Robert Olsen

Time-dependent boundary conditions for multiphase flow

Trondheim, September 2004

Doctoral thesis for the degree of doktor ingeniør

Norwegian University of Science and Technology
Faculty of Engineering Science and Technology
Department of Energy and Process Engineering

NTNU

Abstract

In this thesis a set of boundary conditions for multiphase flow is suggested. Characteristic-based boundary conditions are reviewed for single-phase flow. The problem of open-boundary conditions is investigated, and to avoid drifting values, the use of control functions is proposed.

The use of control functions is also verified with a new test which assesses the quality of the boundary conditions. Particularly, P- and PI-control functions are examined. PI-controllers have the ability to specify a given variable exactly at the outlet as well as at the inlet, without causing spurious reflections which are amplified.

Averaged multiphase flow equations are reviewed, and a simplified model is established. This model is used for the boundary analysis and the computations. Due to the averaging procedure, signal speeds are reduced to the order of the flow speed. This leads to numerical challenges. For a horizontal channel flow, a splitting of the interface pressure model is suggested. This bypasses the numerical problems associated with separation by gravity, and a physical realistic model is used. In this case, the inviscid model is shown to possess complex eigenvalues, and still the characteristic boundary conditions give reasonable results.

The governing equations are solved with a Runge-Kutta scheme for the time integration. For the spatial discretisation, a finite-volume and a finite-difference method are used. Both implementations give equivalent results. In single-phase flow, the results improve significantly when a numerical filter is applied. For two-dimensional two-phase flow, the computations are unstable without a numerical filter.

Preface

The reception of a three year scholarship from the Research Council of Norway and the financial support from SINTEF Energy Research AS which made it possible to conclude this work are gratefully acknowledged.

Above all, it is the continuous interest in this work from my supervisor, professor Inge R. Gran, which made this work worthwhile. It is due to his clear mind and strong will to share his knowledge, that I started on this work in the first place.

I also appreciated the encouraging talks of my other supervisor, professor Bjørn F. Magnussen.

I am grateful for the introduction to characteristic-based boundary conditions that my colleague Kjell Erik Rian gave me at the start of this work, and for his comments to the manuscript.

Thanks are especially given to my colleague Svend T. Munkejord, for his willingness to discuss ideas as well as reading and commenting the manuscript.

Thanks are also given to, Jens A. Melheim, Matteo Chiesa, Skjalg Haaland and my fiancé Anna Ivanova for reading and commenting the manuscript.

This thesis will be submitted for the degree:

Doktor Ingeniør (Dr. ing.)
Doctor of Engineering,

at the Norwegian University of Science and Technology (NTNU).

Trondheim, March 2003

Robert Olsen

Contents

Nomenclature

Latin letters

$\boldsymbol{A}$	System matrix	
A	Area	m^2
$\mathcal{A}$	Control surface	m^2
A_f	Filter coefficient, see Equation (4.24)	–
A_i^j	Cartesian area projections	m^2
J	Jacobian determinant of the coordinate transformation	m^3
b	Body force per unit mass	m/s^2
B_k	Interface pressure coefficient, see Equation (2.54)	–
C	Interface friction coefficient	1/m
c	Speed of sound	m/s
C_s	Interface friction term, see Equation (6.8)	N/m
$\boldsymbol{D}_\mathrm{f}$	Dissipation matrix	
D_h	Hydraulic diameter	m
$f_{m,k}$	Phasic Moody friction parameter	–
$F_{nn,k}$	Mass-flow across the various control volume faces	kg/s
G^{ji}	Geometric diffusion coefficient	

g_x	Gravity component in the x-direction	m/s^2
H_s	Mean curvature	m^{-1}
$\mathbf{I}$	Unitary tensor	–
K_d	Denominator, see Equation (6.15)	Pa
K_D	Derivative coefficient for the controller	
K_I	Integrational coefficient for the controller	
K_P	Proportional coefficient for the controller	
$\boldsymbol{l}_i$	i-th left eigenvector of $\boldsymbol{A}$	
$\boldsymbol{\Lambda}$	Matrix with the eigenvalues of $\boldsymbol{A}$ along the diagonal	
$\mathscr{L}$	Vector containing the wave amplitude variations	
L	Characteristic size of domain	m
$\mathscr{M}$	Maximum Mach number	–
Ma_k	Mach number of phase k	–
$\dot{m}_\mathrm{i}$	Inlet mass-flow rate	kg/s
$\dot{m}_\mathrm{o}$	Outlet mass-flow rate	kg/s
$\boldsymbol{n}$	Unit normal vector	m
$\boldsymbol{P}$	Transformation matrix	
p	Pressure	Pa
Δp	Gauge pressure	Pa
$\dot{Q}_k$	Volume-flow rate	m^3/s
$\boldsymbol{r}_j$	j-th right eigenvector of $\boldsymbol{A}$	
Re	Reynolds number	–
R_k	Right-hand side, see Equation (6.7)	s

$\boldsymbol{S}$	Right eigenvector matrix of $\boldsymbol{A}$	
$\overline{S}_{1P}$	The constant part of the source	
$\overline{S}_{2P}$	The coefficient of the variable part	
t	Time	s
Δt	Time step	s
t‘	Reduced time	–
$\boldsymbol{U}$	Vector of primitive variables	
u	Velocity magnitude	m/s
$\hat{\boldsymbol{U}}$	Vector of composite variables	
$\tilde{U}$	Filtered variable	
$\boldsymbol{u}$	Velocity vector	m/s
V	Volume	m^3
$\mathcal{V}$	Control volume	m^3

Greek letters

α	Volume fraction	–
ζ_D	Filter coefficient	–
β	Angle of inclination	–
δ_{ij}	Kronecker delta	–
Φ	Interfacial momentum transfer	N/m^3
ϕ	Number of phases	–
Γ_k	Mass transfer rate	$kg/(sm^3)$
Γ	Diffusivity in the scalar convection-diffusion equation	
$\varkappa$	Condition number	–

λ_i	Eigenvalue of $\boldsymbol{A}$	m/s
μ	Molecular viscosity	kg/(ms)
ν	Kinematic viscosity	m^2/s
Ω	Interfacial momentum transfer due to mass exchange	N/m^3
π_k	Material parameter of the phase	Pa
ρ	Density	kg/m^3
ρ_m	Mixture density, see Equation (2.40)	kg/m^3
σ	Surface tension	N/m
σ	Coefficient in the proportional parameter, page 43	–
$\boldsymbol{\tau}$	Stress tensor	Pa
χ_k	Factor in definition of volume average, see Equation (2.8)	–
ξ_i	Curvilinear non-orthogonal coordinates	m
ψ	General variable	

Other symbols and labels

$\langle\psi_k\rangle$	Volume average of ψ_k, see Equation (2.6)
${}^{\mathrm{i}}\langle\psi_k\rangle$	Intrinsic average of ψ_k, see Equation (2.7)
2x-8f	Combination of spatial operator and filter function, page 75
PIIO	PI-controller at the inlet and the outlet
PIO2	As PIO, but K_P is half that of PIO
PIO	PI-controller at the outlet, the inlet is set
PO	P-controller the outlet, the inlet is set

Subscripts and superscripts

$\circ$	Reference state

+	Sub- matrix or vector associated with positive eigenvalues
−	Sub- matrix or vector associated with negative eigenvalues
1D	Matrix or vector as in the one-dimensional case
d	$d = 2$ for 2D and $d = 3$ for 3D, see Equation (2.37)
f	Second phase index
in	Initial value
k	Phase index
l	Third phase index
nb	The neighbouring nodes surrounding the central node P
T	Transposed matrix or vector

Abbreviations

3D	Three Dimensional
CBC	Characteristic-based Boundary Conditions
CFD	Computational Fluid Dynamics
DNS	Direct Numerical Simulations
LES	Large-Eddy Simulations
LODI	Locally One-Dimensional Inviscid, page 40
MPCBC	Multiphase Characteristic Boundary Conditions, page 53
NRBC	Non-Reflecting Boundary Conditions
NSCBC	Navier-Stokes Characteristic Boundary Conditions, page 44
ODE	Ordinary Differential Equation
PID	Three-mode controller: Proportional, Integrational, Derivative
POW	Power-law scheme

RKFD	Runge-Kutta Finite Difference
RKFV	Runge-Kutta Finite Volume
SOU	Second-Order Upwind scheme

Chapter 1

Introduction

Computational fluid dynamics (CFD) has evolved during the last decades and become an important tool for the scientist to gain a better understanding of complex flow phenomena.

A realistic mathematical model is required in order to obtain good numerical solutions. For initial-boundary value systems, like the Navier-Stokes equations or the multiphase equations, relevant initial values and boundary conditions must be provided in order to have a complete mathematical description of the problem.

In the mathematical model, the boundary conditions describe how the domain interacts with the surroundings.

1.1 Motivation for the thesis

In numerical simulations of flows, artificial boundaries are needed to obtain a finite computational domain when an unbounded physical domain is given. Artificial boundaries which fluids are free to cross are called open boundaries.

This thesis focuses on steady-state computations of internal flow. When compressible flow methods are applied, setting the spatial derivative of the variable in question to zero by assuming that the outlet is far downstream, or setting the outlet pressure to a known value may lead to reflections. These reflections may grow in amplitude and contaminate the computation. Therefore, a proper treatment of the open boundaries in numerical simulations of multidimensional compressible multiphase flow is required.

1.2 Multiphase flow

Our ability to predict multiphase flow behaviour, is crucial for the design, quantification, and control of equipment.

Two-phase flow is extremely complex and very challenging for the scientist. Even in a simple geometry, like flow in pipes, the situation can be chaotic and frustrating. The flow can exist in several different states called flow patterns. Among the patterns we find annular flow, annular mist, churn flow, stratified, bubbly, and slug flow. Each of the patterns have their own characteristics. For a discussion about flow regimes and flow patterns, see for instance Spedding and Spence (1993).

1.2.1 Multiphase and multifluid flow

It is natural to use different methods for different types of flows. Saurel and Abgrall (1999a) made a distinction between multiphase flow and multifluid flow. A schematic presentation is given in Figure 1.1.

> In multiphase flows, a control volume contains a large number of individual particles (or bubbles, etc.) with many interfaces, while in multifluid flows, nearly all control volumes contain pure phases, except for the computational cells around the interface.

Although such a distinction is not explicitly used in this work, it can be of importance when it comes to interpreting computational results.

An Eulerian description of two-phase flow has been established over the years. The derivation of the balance equations is based on a homogenisation technique, like time-averaging (Ishii, 1975), volume-averaging (Soo, 1990) or ensemble averaging (Drew and Passman, 1999). Multi-field models use α_k (time-fraction, volume-fraction or expectation) to characterise the presence of phase k. Then ϕ velocities may co-exist at the same time and at the same location, where ϕ is the number of phases.

The resulting model is ill-posed and mathematically complex, in the sense that the system is non-hyperbolic, non-linear and non-conservative, and can be said to be an ill-posed approximation of the physical reality. The ill-

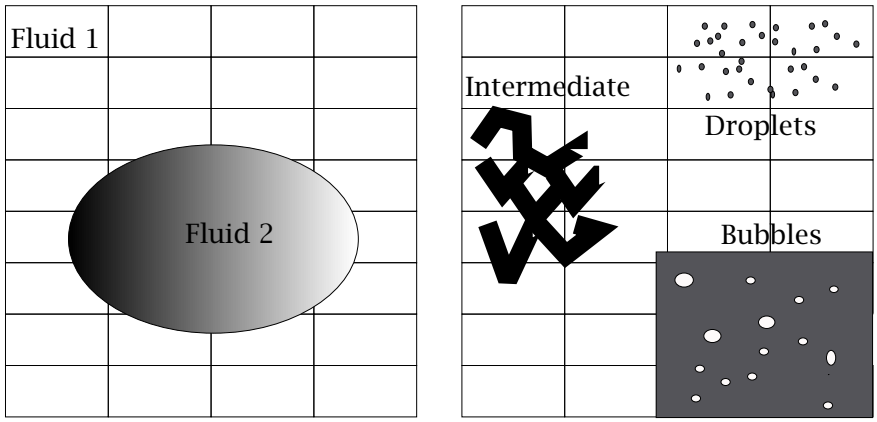

(a) Multifluid (b) Multiphase

Figure 1.1: Schematic representation of a multifluid flow and several multiphase flows, (Saurel and Abgrall, 1999a).

posed two-fluid model requires regularisation[a]. These issues have caused a lot of confusion in the literature, see Ramshaw and Trapp (1978). Dinh *et al.* (2003) collect recent advances from mathematical analyses of ill-posed partial differential equations, and an understanding of the challenging mathematical properties in two-fluid flow is provided.

Mathematical regularisation

Two different types of regularisation techniques are used in the literature. Those using mathematical regularisation attempt to alter the basic set of equations. Saurel and Abgrall (1999a,b) and Saurel and LeMetayer (2001) add an extra equation and solve these equations with a relaxation procedure. Dinh *et al.* (2003) propose to solve the equations in a $t - \tau - x$ space, although the new problem is much more computationally demanding.

Another type of mathematical regularisation which has been successful

[a]Regularisation is here used as a collective term to denote various mathematical or numerical techniques used to amend the system of governing equations in order to facilitate their numerical solution.

is the level set method. Caiden *et al.* (2001) use this method to simulate two-phase flow with regions of compressible and incompressible flow. The method is shown to be able to compute one- and two-dimensional flow.

Numerical regularisation

The other type of regularisation is numerical regularisation. Those using numerical regularisation attempt to alter the numerical procedure to obtain numerical solutions. Hwang (2003) uses an upwind scheme designed for non-hyperbolic problems. By a transformation, which splits the system of equations into a real and a complex part, he derives a canonical form for the non-hyperbolic system in the real space.

Evje and Fjelde (2003) construct a hybrid splitting scheme and achieve good results with the water faucet case. Lee and Lyczkowski (2000) examine five two-phase flow models with three different test problems, and found that none of them could be entirely rejected on the basis of producing physically impossible or unacceptable results. The general performance of the five models was found to be similar.

In the field of direct numerical simulations (DNS) and large-eddy simulations (LES) a clean and modern way of achieving numerical regularisation is to use numerical filters (Mathew *et al.*, 2003).

CFD in multiphase flow

Early numerical models of multiphase flows were most often tailored to a particular geometry, and specific flow regimes. Examples of such models are OLGAS (Bendiksen *et al.*, 1991) and various ones used in the nuclear industry.

The use of two- and three-dimensional CFD for multiphase flows can enable the solution of flows in complex geometries, as well as flow phenomena which otherwise could not be calculated.

Early two-fluid flow codes primarily originate from single-fluid flow codes based on the Implicit, Continuous-fluid, Eulerian (ICE) solution scheme developed by Harlow and Amsden (1971) or the Semi-Implicit Method for Pressure-Linked Equations (SIMPLE) by Patankar and Spalding (1972).

Moura and Rezkallah (1993) used a semi-implicit scheme to study the two-phase flow distribution in a T-junction, and reported good agreement

between calculated results and experimental data for the phase separation.

1.3 Boundary conditions

The neccessity of open boundary conditions can be understood by studying the one-way wave equation (Strikwerda, 1989, Chapter 1):

$$\frac{\partial u}{\partial t} + a\frac{\partial u}{\partial x} = 0, \tag{1.1}$$

where $a > 0$ is a constant, t is time, and x is the spatial variable. Equation (1.1) has the solution

$$u(t,x) = u_0(x - at), \tag{1.2}$$

where $u_0(x) = u(0,x)$. If this problem is to be solved on a finite domain, say $-1 \leq x \leq 1$, then it is obvious that a boundary condition for u at $x = -1$ must be specified, and no boundary condition can be specified for u at $x = 1$.

If this problem is extended to two variables,

$$\frac{\partial \boldsymbol{U}}{\partial t} + \boldsymbol{A}\frac{\partial \boldsymbol{U}}{\partial x} = 0, \tag{1.3}$$

where $\boldsymbol{U} = [u_1, u_2]$ and $\boldsymbol{A}$ is diagonalisable, then the transformation,

$$\boldsymbol{W} = \boldsymbol{S}^{-1}\boldsymbol{U}, \tag{1.4}$$

where $\boldsymbol{S}$ is the eigenvector matrix, gives a decoupled set of one-way wave equations

$$\frac{\partial w_i}{\partial t} + \lambda_i\frac{\partial w_i}{\partial x} = 0, \tag{1.5}$$

with characteristic velocities λ_i. If for instance $\lambda_1 > 0$ and $\lambda_2 < 0$, w_1 must be specified on the left boundary and w_2 on the right boundary. A direct specification of u_1 would not give a solution of the problem, and may in some cases lead to an ill-posed problem. However, u_1 could be specified through w_1 and w_2.

1.3.1 Boundary conditions in single-phase flow

The Navier-Stokes equations are much more complicated than the one-way wave equation. The one-way wave equation is a hyperbolic equation, while the Navier-Stokes equations can be considered as incomplete parabolic, see (Tourrette, 1997).

Many names are used in the literature to refer to artificial or open boundary conditions, depending on the scientific field. In a review article, Givoli (1991) finds radiating, absorbing, silent, transmitting, transparent, open, free-space, and one-way boundary conditions. He uses the term *non-reflecting boundary conditions* (NRBC).

Givoli also gives a list which the designer of NRBC should keep in mind.

1. The problem together with the boundary conditions is well-posed.
2. The problem together with the boundary conditions is a good approximation of the original problem in the infinite domain.
3. The boundary condition is highly compatible with the numerical scheme used in the internal domain.
4. The numerical method employed together with the boundary condition must result in a stable numerical scheme.
5. The amount of spurious reflection generated by the boundary condition is small.
6. The use of the boundary condition does not involve a large computational effort.
7. In time-dependent schemes where only the steady-state solution is sought, the numerical scheme should reach the steady state rapidly.

An extensive review of the numerical solution of problems on unbounded domain is given by Tsynkov (1998). The different boundary strategies are normally divided into local and non-local methods.

Engquist and Majda (1977, 1979) derive theoretical boundary conditions, which are nonlocal in space and time. The non-locality is the price one has to pay in order to eliminate an infinite spatial domain. When the problem

under consideration is time-independent, a NRBC has to be spatially non-local in order to exactly represent the entire exterior domain. If the problem depends on time, then an exact condition has to represent the history of the exterior as well (Givoli, 1991). Recent articles which use non-local methods are (Keller and Givoli, 1989), (Givoli, 1992), (Tsynkov *et al.*, 2000), (Ryaben'kii, 2000), (Ryaben'kii *et al.*, 2001).

The local methods are typically easier to implement, but are usually less accurate than the nonlocal methods. Givoli (1991) points out that many local methods have been constructed such that spurious reflections are kept small for a certain range of frequencies and perform well in some situations and poorly in others. He recommends nonlocal boundary conditions. Givoli and Patlashenko (1998) tries to solve the non-local problem with a local approximation and derive an optimal approximation of the Dirichlet-to-Neumann boundary condition.

A mathematical treatment of an absorbing boundary condition for hyperbolic equations is presented by Engquist and Majda (1977, 1979).

Over the years, there have been attempts to design absorbing layers where dissipative terms are added to damp outgoing waves. The approach is either to slow down the waves, where the reflected waves do not reach the domain during the computation, or to force a decay. Examples are found in Abarnel *et al.* (1999), Yost *et al.* (2000), Colonius and Ran (2002), Hu (2001).

Characteristic-based boundary conditions

Thompson (1987, 1990) presents a characteristic-based way of constructing boundary conditions for the Euler equations. This method is straightforward to implement, and extend to other types of flows. Poinsot and Lele (1992) have developed this method further for direct numerical simulations of compressible flow, and Baum *et al.* (1994) extend this to reactive multi-component flow. Okong'o and Bellan (2002) extend the method further to real gas mixtures. Characteristic-based boundary conditions have evolved to become an attractive way of solving the boundary problem and have been used in a number of studies, see Salvesen and Teigland (1998) and Rian (1999, 2003).

Kim and Lee (2000) present generalised characteristic boundary conditions for computational aeroacoustics, where the conservative formulation with generalised coordinates is used.

Bruneau and Creusé (2001) discuss new artificial boundary conditions based on the hyperbolic part of the equations. They conclude that setting the amplitude of the incoming wave to zero is unsatisfactory when vortices are leaving the domain.

Tourrette (1997, 1998) develops artificial boundary conditions for the linearised compressible Navier-Stokes equations. He uses a previous developed method for deriving artificial boundary conditions for incompletely parabolic perturbations of hyperbolic systems.

Sutherland and Kennedy (2003) study direct numerical simulations of combustion and review the boundary treatment in that sense. They combine theory and boundary treatment from incomplete parabolic problems with the theory of Thompson, and they propose a refinement of the method. They also mention that they want to control the incoming waves by a controller, although no details about the control function are provided in their work.

Navier-Stokes Characteristic Boundary Conditions

The key idea for characteristic-based boundary conditions (CBC) is to identify outgoing and incoming waves and to set the correct boundary conditions in terms of them. To ensure well-posed and well-behaved solutions, waves emerging from the computational domain must be calculated from the domain and not specified by boundary conditions.

The CBC method is only strictly valid for hyperbolic systems, like the Euler equations. However, Poinsot and Lele (1992) use results from well-posedness analyses and extend CBC to the Navier-Stokes equations, as forementioned, and call them NSCBC (Navier-Stokes Characteristic Boundary Conditions). The Navier-Stokes equations are not a hyperbolic system of equations, but transport waves like the Euler equations do. Due to its simplicity the NSCBC method is an appealing approach.

A boundary condition is called a physical boundary condition when it specifies the known physical behaviour of one or more of the dependent variables on the boundary. Boundary conditions are called numerical (soft), when no explicit boundary condition fixes one of the dependent variables and the numerical implementation requires us to specify something about this variable.

In the method of Thompson and in the NSCBC method, the number of

physical boundary conditions equals the number of incoming waves. The numerical conditions are provided by solving the governing equations on the boundary. In the NSCBC method, additional viscous conditions are imposed directly into the system solved at the boundary. By doing so, the NSCBC method relaxes smoothly to the method of Thompson when the viscosity approaches zero.

1.3.2 Boundary conditions in multiphase flow

For multiphase flow there are not that many theoretical works on boundary conditions to be found in the literature.

Cheng *et al.* (1999) study boundary conditions for a two-pressure two-phase flow model deducted from drag and buoyancy laws.

Haley *et al.* (1993) give a characteristic analysis of void waves with the two-fluid model, and found that the void waves involve shock and rarefaction waves.

Chung *et al.* (2002) discuss sonic speeds obtained with characteristic analysis.

In this thesis, characteristic-based boundary conditions are developed for multiphase flow. In a recent published work, Nourgaliev *et al.* (2003a,b) also use a characteristic-based approach to solve the two-fluid model. As opposed to this work, they neglect the non-conservative part in the characteristic analysis. Still they obtain numerical solutions.

1.4 Present contribution

The need for a proper treatment of open boundaries in multiphase flow is recognised.

A local quasi-one-dimensional characteristic approach, which is developed from the principles of Thompson (1987, 1990) and Poinsot and Lele (1992), is proposed for boundary conditions for time-dependent compressible multiphase flow. In this method, boundary conditions are set through the incoming wave amplitudes. This work proposes an approach based on the use of control functions to estimate the incoming wave amplitude.

Two numerical codes are developed for the computations and to verify the implementations: one finite-volume code based on the work of Melaaen

(1990, 1992b,a) and one finite-difference code based on a DNS code made by Gran (2000). Both codes use an explicit low-storage five-stage fourth-order Runge-Kutta scheme for the temporal integration.

Numerical calculations of a single-phase Poiseuille flow are carried out to validate the present boundary treatment against the results of Poinsot and Lele (1992) and to evaluate the control functions. A new test which assesses the quality of the boundary treatment is presented, and the proposed boundary treatment shows excellent quality with this test.

The derivation of volume-averaged equations for multiphase flow is reviewed, and a simplified model describing multiphase flow is established. With this model, the case of separation by gravity is discussed.

Different possibilities of formulating the boundary expressions for multiphase flow are discussed. A new method, which gives good coupling when more than one variable is specified at the boundary, is developed.

Multiphase flow is generally more complicated than single-phase flow. The issues of ill-posedness and complex eigenvalues of the inviscid model are discussed. With the simplified model, computations of one-dimensional multiphase flow are carried out and discussed. The steady-state solution of the transient one-dimensional problem is compared with the solution of a direct steady-state solver. A two-dimensional flow in a horizontal channel is computed and evaluated with respect to the boundary conditions.

1.5 Survey of the thesis

Chapter 2 reviews the derivation of volume-averaged equations for multiphase flow. A simplified model is established for further study.

Chapter 3 reviews characteristic-based boundary conditions. A general derivation is provided. Boundary conditions for single-phase and multiphase flow are discussed.

Chapter 4 presents the choice of numerical methods and discusses issues related to those.

Chapter 5 presents the case study of single-phase Poiseuille flow. Different possibilities for the boundary conditions are discussed and evaluated.

Chapter 6 presents the case study of multiphase flow. Additional difficulties in multiphase flow are reviewed and discussed. The boundary conditions are evaluated by computations of one- and two-dimensional flow.

Chapter 7 draws conclusions from the present work.

Appendix A presents the extension of the boundary treatment to three dimensions.

Appendix B presents a summarised multiphase flow model.

Chapter 2

Basic equations

This chapter reviews the derivation of the basic equations of multiphase flow, and is based on the work presented in the article of Munkejord *et al.* (2003).

The mathematical modelling and numerical simulation of multiphase flow is an area of ongoing research.

In section 2.1, the basic equations for multiphase flow are derived. Time versus volume averaging is briefly discussed. The volume averaged dynamic equations for a phase and its interface are given. In section 2.2, the mathematical model of multiphase flow used throughout this thesis is presented. Further, a link between the basic equations derived using the averaging techniques and the mathematical model suited for implementing in a numerical code is provided. Finally, in section 2.3, the interfacial pressure force is discussed.

2.1 Multiphase flow equations

This chapter reviews the basic equations of multiphase flow. Special attention is paid to volume averaging. It is seen that the averaging procedure gives rise to transfer integrals in the conservation equations. These integrals are unknown and must be modelled.

2.1.1 Basic equations

Equations for a pure phase

The conservation equations for a pure phase are well known, and are therefore stated here without derivation. This section will use the terminology

of Soo (1990, Section 6.1) and Soo (1989, Section 2.1). It is reasonable that within phase k, the continuity equation[a] is

$$\frac{\partial}{\partial t}\rho_k + \boldsymbol{\nabla}\cdot(\rho_k \boldsymbol{u}_k) = 0, \tag{2.1}$$

and the momentum equation is

$$\frac{\partial}{\partial t}(\rho_k \boldsymbol{u}_k) + \boldsymbol{\nabla}\cdot(\rho_k \boldsymbol{u}_k \otimes \boldsymbol{u}_k) = -\boldsymbol{\nabla} p_k + \boldsymbol{\nabla}\cdot\boldsymbol{\tau}_k + \rho_k \boldsymbol{b}, \tag{2.2}$$

where $\boldsymbol{u}_k \otimes \boldsymbol{u}_k$ is the tensor product between the velocities. That is, the velocity vectors are first-order tensors. In a Cartesian coordinate system, this can be written as

$$\boldsymbol{u}_k \otimes \boldsymbol{u}_k = u_{i,k} u_{j,k} \boldsymbol{e}_i \otimes \boldsymbol{e}_j = \begin{bmatrix} u_1u_1 & u_1u_2 & u_1u_3 \\ u_2u_1 & u_2u_2 & u_2u_3 \\ u_3u_1 & u_3u_2 & u_3u_3 \end{bmatrix}_k . \tag{2.3}$$

From here on the tensor multiplication sign is dropped, that is, the tensor product will be denoted $\boldsymbol{u}_k\boldsymbol{u}_k$. The energy equation has not been considered in this work.

Interface relations

In order to derive interface relations for multiphase flow, it is necessary to consider a control volume containing more than one phase. Such a control volume and the interacting phases are shown in Figure 2.1. V_k is the volume of phase k inside the control volume $\mathcal{V}$, and V is the total volume of $\mathcal{V}$. The control surface $\mathcal{A}_k$ has an area A_k and is the interface between phases k and f inside $\mathcal{V}$. Generally, other phases l might also be present, but they are not considered when discussing the interaction between the phases k and f.

The mass and momentum balances *at the interface* between phases k and f reads, (Soo, 1990, page 306):

$$\rho_k(\boldsymbol{u}_k - \boldsymbol{u}_s)\cdot\boldsymbol{n}_k + \rho_f(\boldsymbol{u}_f - \boldsymbol{u}_s)\cdot\boldsymbol{n}_f = 0, \tag{2.4}$$

[a] In the following, Einstein's summation rule is not to be applied on the indices k and f, which are being used to denote phases.

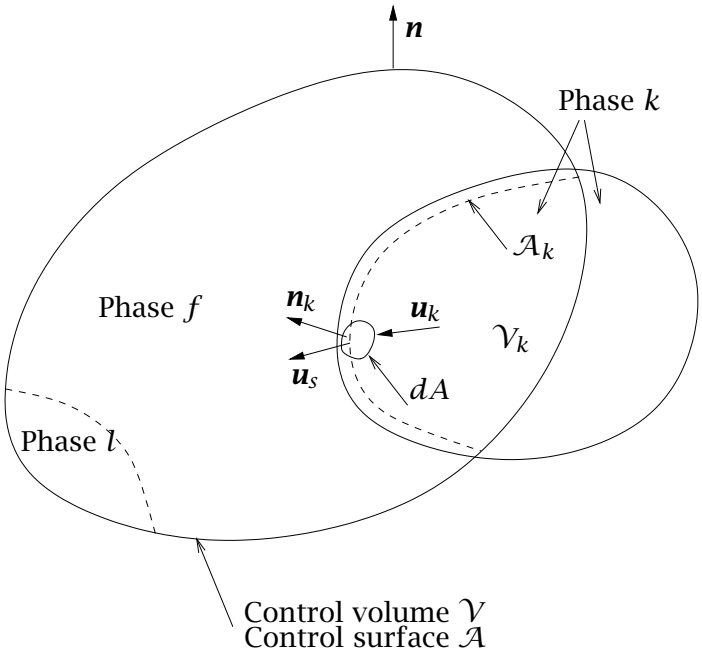

Figure 2.1: Control volume and interacting phases.

and

$$\underbrace{-\nabla_s\sigma}_{\text{(i)}} + \underbrace{2\sigma H_s \boldsymbol{n}}_{\text{(ii)}} - \underbrace{\rho_k \boldsymbol{u}_k(\boldsymbol{u}_k - \boldsymbol{u}_s)\cdot\boldsymbol{n}_k}_{\text{(iii)}} - \underbrace{\rho_f \boldsymbol{u}_f(\boldsymbol{u}_f - \boldsymbol{u}_s)\cdot\boldsymbol{n}_f}_{\text{(iv)}} + \underbrace{(-\mathbf{I}p_k + \boldsymbol{\tau}_k)\cdot\boldsymbol{n}_k}_{\text{(v)}} + \underbrace{(-\mathbf{I}p_f + \boldsymbol{\tau}_f)\cdot\boldsymbol{n}_f}_{\text{(vi)}} = 0, \quad (2.5)$$

where $\boldsymbol{n}_k$ is the outward unit normal vector from phase k, H_s^{-1} is the mean radius of curvature along $\boldsymbol{n}_k$, σ is the interfacial tension, ∇_s is the surface gradient operator, and $\mathbf{I}$ is the unitary tensor. The interfacial velocity is given by $\boldsymbol{u}_s$, and H_s is positive when the associated radius of curvature is pointing outward. The effect of change in mean curvature is ignored.

Equation (2.4) plainly states that the mass transfer from phase k to phase f must be equal in size and opposite to the mass transfer from phase f to phase k. If $\boldsymbol{u}_k = \boldsymbol{u}_s = \boldsymbol{u}_f$ at the interface, then no mass transfer takes place.

The momentum balance (2.5) is written in force per length (N/m) units, where

term (i) is due to changes in the surface tension along the interface, for example due to temperature or composition gradients[b],

term (ii) is because the radius of curvature will cause the surface tension to yield a resultant force normal to the interface,

term (iii) is due to mass transfer from phase k to phase f,

term (iv) is due to mass transfer from phase f to phase k,

term (v) is due to pressure and stresses in phase k, and

term (vi) is due to pressure and stresses in phase f.

When no mass transfer takes place, the terms (iii) and (iv) will disappear from the interface momentum Equation (2.5), because $\boldsymbol{u}_k = \boldsymbol{u}_s = \boldsymbol{u}_f$ at the interface. That is, for a flow without mass transfer, the surface tension forces are balanced by pressure and stress forces. If the surface tension is negligible, then the pressure and stress of each phase are equal at the interface.

The computational domain has been divided into small control volumes $\mathcal{V}$ according to Figure 2.1. The finest level of detail of the computation is the control-volume level. The basic equations, however, are written on a microscopical level. Therefore it is necessary to introduce a proper averaging technique.

2.1.2 Averaging

The motion of fluid flow in engineering applications varies over so many orders of magnitude in both length and time scales, that it is computationally intractable to directly solve the full conservation Equations (2.1)–(2.2), except in highly simplified cases.

Averaging may be seen as a sort of low-pass filtering which is employed to reduce the amount of computational effort required to solve the equations. It is necessary to introduce models to account for the scales which

[b] That is, $\sigma = \sigma(p, T, n_i)$, where n_i indicates the material components involved.

are 'filtered away'. A model is a more or less simplified view of a physical phenomenon together with mathematical equations describing this view.

Time versus volume averaging

There are many ways to compute an average, for instance with respect to time, space, volume, area or statistical mean (ensemble average). In his two-fluid model, Ishii (1975, Page 61) applied time averaging to the basic conservation equations. He argued that since time averaging has proven useful in single-phase turbulent flow analysis, it is natural and logical also to apply time averaging to two-phase flow. Ishii identified two main consequences of time averaging, namely

1. to smooth out turbulent fluctuations in the same sense as in single-phase flow, and

2. to bring two phases, which are alternately occupying a volume element, into two continua simultaneously existing at the same point with a properly defined expectation for each phase.

Soo (1989, Page 49), on the other hand, maintained that volume averaging is convenient in expressing dynamic phases in terms of volume fractions, while an a priori time averaging yields fraction residence times of phases. He further stated that dynamic and thermodynamic properties of a mixture are not cumulative with fractional residence time, but with volume fractions, and that fractional residence time is equal to volume fraction only in the instance of one-dimensional uniform motion in a mixture. Therefore, time and volume averaging operations are not commutative. Soo recommended to carry out time averaging after volume averaging to account for the high frequency fluctuations retained by instantaneous volume averaging.

Drew and Passman (1999) used ensemble averaging and gave a more detailed discussion of different averaging methods for multiphase flow.

However, in this work, attention has been payed to the arguments of Soo (1989). Therefore we continue by discussing volume averaging.

Volume averaging of a phase in a mixture

The volume averaging, when applied to any scalar, vector or tensor ψ_k associated with phase k is defined by:

$$\langle \psi_k \rangle = \frac{1}{V} \int_{\mathcal{V}_k} \psi_k \, dV, \tag{2.6}$$

when averaged over volume V, and when averaged over V_k, the intrinsic average is:

$$^{\mathrm{i}}\langle \psi_k \rangle = \frac{1}{V_k} \int_{\mathcal{V}_k} \psi_k \, dV. \tag{2.7}$$

That is, $\langle \psi_k \rangle$ is averaged over the whole control volume $\mathcal{V}$, whereas $^{\mathrm{i}}\langle \psi_k \rangle$ is averaged only over the part of the control volume where phase k is present, $\mathcal{V}_k$.

To achieve a mathematically rigorous fundament, the definition of volume averaging in Equation (2.6) may instead be written as

$$\langle \psi_k \rangle = \frac{1}{V} \int_{\mathcal{V}} \psi_k \chi_k \, dV. \tag{2.8}$$

Now the integration is performed over the whole control volume $\mathcal{V}$. The factor χ_k is defined as 1 inside $\mathcal{V}_k$ and as 0 outside $\mathcal{V}_k$. Analogously we get for the intrinsic average in Equation (2.7):

$$^{\mathrm{i}}\langle \psi_k \rangle = \frac{1}{V_k} \int_{\mathcal{V}} \psi_k \chi_k \, dV. \tag{2.9}$$

When the averaging relations (2.6) and (2.7) are applied to a specific quantity such as density, we have:

$$\langle \rho_k \rangle = \frac{1}{V} \int_{\mathcal{V}_k} \rho_k \, dV = \alpha_k \overline{\rho}_k, \tag{2.10}$$

and

$$^{\mathrm{i}}\langle \rho_k \rangle = \frac{1}{V_k} \int_{\mathcal{V}_k} \rho_k \, dV = \overline{\rho}_k. \tag{2.11}$$

Herein the volume fraction of phase k is defined as $\alpha_k = V_k/V$. The latter equalities are for uniform material density $\overline{\rho}_k$ of phase k.

Some points are worth noting (Soo, 1989, page 51):

1. Intrinsic averaging gives rise to quantities inside $\mathcal{V}_k$.

2. Volume averaging will spread phase k over the whole volume $\mathcal{V}$, superposing on phase f, which is correspondingly averaged in the same manner. So, for instance, the density $\langle \rho_k \rangle$ is averaged over $\mathcal{V}$ and is equal to ${\alpha_k}^{\mathrm{i}}\langle \rho_k \rangle$.

3. Volume averaging can only be applied to quantities per volume or area. These include density, momentum per unit volume, energy per unit volume, and gradients of stresses and fluxes for ψ_k in equations (2.6) and (2.7). Therefore, for instance, the intrinsic average of the phase velocity is given by:

$$ {}^{\mathrm{i}}\langle \boldsymbol{u}_k \rangle = \frac{1}{{}^{\mathrm{i}}\langle \rho_k \rangle \, V_k} \int_{\mathcal{V}_k} \rho_k \boldsymbol{u}_k \, dV = \frac{1}{\langle \rho_k \rangle \, V} \int_{\mathcal{V}_k} \rho_k \boldsymbol{u}_k \, dV \tag{2.12} $$

4. Stresses and fluxes in a formulation can be expressed as $\langle \psi_k \rangle = {\alpha_k}^{\mathrm{i}}\langle \psi_k \rangle$; the physical meaning is represented in the 'volume average' where all interactions are represented.

As we shall see, $\langle \boldsymbol{\tau}_k \rangle$, the viscous stress, is not necessarily contributed by the viscous stress inside phase k. It may represent the resistance to transfer of momentum by bodily displacement of one phase through another. That is, $\langle \boldsymbol{\tau}_k \rangle$ has two contributions; one from within the phase and one from its surface. The same applies to $\langle p_k \rangle$.

The following relations can be derived from the general transport theorem for volume averages of derivatives, according to the averaging theorems of Whitaker (1969) and Slattery (1967):

$$ \langle \boldsymbol{\nabla} \psi_k \rangle \equiv \frac{1}{V} \int_{\mathcal{V}_k} \boldsymbol{\nabla} \psi_k \, dV = \boldsymbol{\nabla} \langle \psi_k \rangle + \frac{1}{V} \int_{\mathcal{A}_k} \psi_k \boldsymbol{n}_k \, dA, \tag{2.13} $$

and from Reynolds transport theorem

$$ \left\langle \frac{\partial}{\partial t} \psi_k \right\rangle = \frac{\partial}{\partial t} \langle \psi_k \rangle - \frac{1}{V} \int_{\mathcal{A}_k} \psi_k \boldsymbol{u}_s \cdot \boldsymbol{n}_k \, dA, \tag{2.14} $$

where $\boldsymbol{u}_s \cdot \boldsymbol{n}_k$ is the speed of displacement of the interface. These averaging

relations are subject to the restriction[c] that

$$\{\text{characteristic lengths of phases or pores}\} \ll \{\text{characteristic length of averaging volume } \mathcal{V}\} \ll \{\text{characteristic length of the physical system}\}. \quad (2.15)$$

Therefore, the control volume $\mathcal{V}$ under consideration cannot be arbitrarily small or become infinitesimal. Furthermore, the control volume $\mathcal{V}$ needs to be much larger than the size of the phases or pores, so that a small translation of the control volume will not influence the magnitude of the averaged variables $\langle \psi_k \rangle$. Yet in order for the average to be representative of the local variations, the control volume must be small, such that its characteristic dimension is smaller than that of the physical system under consideration.

Inserting $\psi_k = 1$ in Equation (2.6) yields

$$\langle 1 \rangle = \frac{1}{V} V_k = \alpha_k. \quad (2.16)$$

Using Equation (2.16) in Equation (2.14) then gives

$$\frac{\partial}{\partial t} \alpha_k = \frac{1}{V} \int_{\mathcal{A}_k} \boldsymbol{u}_s \cdot \boldsymbol{n}_k \, dA, \quad (2.17)$$

and analogously for Equation (2.13):

$$\boldsymbol{\nabla} \alpha_k = -\frac{1}{V} \int_{\mathcal{A}_k} \boldsymbol{n}_k \, dA. \quad (2.18)$$

2.1.3 Volume-averaged dynamic equations for a phase and its interface

Continuity

As the average of a sum equals the sum of averages, the averaging relations (2.13)–(2.14) can be applied term-wise to the continuity Equation (2.1):

$$\frac{\partial}{\partial t} \langle \rho_k \rangle + \boldsymbol{\nabla} \cdot \langle \rho_k \boldsymbol{u}_k \rangle = -\frac{1}{V} \int_{\mathcal{A}_k} \rho_k (\boldsymbol{u}_k - \boldsymbol{u}_s) \cdot \boldsymbol{n}_k \, dA = \Gamma_k, \quad (2.19)$$

where Γ_k is the rate of generation of phase k per unit volume of $\mathcal{V}$ as the interface displaces outward relative to phase k.

[c] That is, the mathematical theorems are general, but the physical meaning of the averaged quantities $\langle \psi \rangle$ is subject to this restriction.

Momentum

Similarly, applying the averaging relations to the momentum Equation (2.2) yields:

$$\frac{\partial}{\partial t}\langle \rho_k \boldsymbol{u}_k \rangle + \boldsymbol{\nabla}\cdot\langle \rho_k \boldsymbol{u}_k \boldsymbol{u}_k \rangle = -\boldsymbol{\nabla}\langle p_k \rangle + \boldsymbol{\nabla}\cdot\langle \boldsymbol{\tau}_k \rangle + \langle \rho_k \rangle \boldsymbol{b} + \frac{1}{V}\int_{\mathcal{A}_k} (-p_k \boldsymbol{n}_k + \boldsymbol{\tau}_k \cdot \boldsymbol{n}_k)\, dA - \frac{1}{V}\int_{\mathcal{A}_k} \rho_k \boldsymbol{u}_k (\boldsymbol{u}_k - \boldsymbol{u}_s)\cdot \boldsymbol{n}_k\, dA, \quad (2.20)$$

where the force field per unit mass, $\boldsymbol{b}$, is assumed to be constant in $\mathcal{V}$. The last two terms are transfer integrals, and it is necessary to give them a careful physical interpretation. They account for the transfer of pressure, viscous stresses and inertia across the interface per unit volume.

Interface balances

The volume-averaged interface balance equations are obtained by integrating equations (2.4) and (2.5) over the interface $\mathcal{A}_k$ and dividing by the control volume. The mass balance is given by:

$$\Gamma_k = -\frac{1}{V}\int_{\mathcal{A}_k} \rho_k (\boldsymbol{u}_k - \boldsymbol{u}_s)\cdot \boldsymbol{n}_k\, dA = \frac{1}{V}\int_{\mathcal{A}_k} \rho_f (\boldsymbol{u}_f - \boldsymbol{u}_s)\cdot \boldsymbol{n}_f\, dA = -\Gamma_f. \quad (2.21)$$

The momentum balance is given by:

$$\frac{1}{V}\int_{\mathcal{A}_k} (-\boldsymbol{\nabla}_s \sigma + 2\sigma H_s \boldsymbol{n})\, dA - \frac{1}{V}\int_{\mathcal{A}_k} \rho_k \boldsymbol{u}_k (\boldsymbol{u}_k - \boldsymbol{u}_s)\cdot \boldsymbol{n}_k\, dA - \frac{1}{V}\int_{\mathcal{A}_k} \rho_f \boldsymbol{u}_f (\boldsymbol{u}_f - \boldsymbol{u}_s)\cdot \boldsymbol{n}_f\, dA + \frac{1}{V}\int_{\mathcal{A}_k} (-\mathbf{I} p_k + \boldsymbol{\tau}_k)\cdot \boldsymbol{n}_k\, dA + \frac{1}{V}\int_{\mathcal{A}_k} (-\mathbf{I} p_f + \boldsymbol{\tau}_f)\cdot \boldsymbol{n}_f\, dA = 0. \quad (2.22)$$

For bubbles and droplets, the first integral gives the capillary pressure (denoted by subscript c) difference:

$$\frac{1}{V}\int_{\mathcal{A}_k} (-\boldsymbol{\nabla}_s \sigma + 2\sigma H_s \boldsymbol{n})\, dA = \frac{1}{V}\int_{\mathcal{A}_k} (p_{c,k} - p_{c,f})\, dA. \quad (2.23)$$

The equations in the present section include averages and averages of products as well as local values in the interface transfer integrals. The configurations of the interface and its motion are given by $\boldsymbol{u}_s$, $\boldsymbol{n}_k$, and $\mathcal{A}_k$. Solution of equations (2.19) and (2.20) calls for expressing averages of products in terms of products of averages and to express the integrals in terms of averaged dependent variables by introducing proper constitutive relations.

Recall the expression for the intrinsic average of the phase velocity from Equation (2.12). Analogously, we may now write for the volume-averaged rate of change of momentum flux of phase k per unit area:

$$\begin{aligned}\langle \rho_k \boldsymbol{u}_k \boldsymbol{u}_k \rangle \equiv \frac{1}{V} \int_{\mathcal{V}_k} \rho_k \boldsymbol{u}_k \boldsymbol{u}_k \, dV &= \langle \rho_k \rangle \frac{1}{{}^{\mathrm{i}}\langle \rho_k \rangle \, V_k} \int_{\mathcal{V}_k} \rho_k \boldsymbol{u}_k \boldsymbol{u}_k \, dV \\ &= \langle \rho_k \rangle \, {}^{\mathrm{i}}\langle \boldsymbol{u}_k \boldsymbol{u}_k \rangle = \alpha_k \, {}^{\mathrm{i}}\langle \rho_k \rangle \, {}^{\mathrm{i}}\langle \boldsymbol{u}_k \boldsymbol{u}_k \rangle \,. \end{aligned} \tag{2.24}$$

In the second and in the last equality, we have used that

$$\alpha_k = \frac{V_k}{V} = \frac{\langle \rho_k \rangle}{{}^{\mathrm{i}}\langle \rho_k \rangle}. \tag{2.25}$$

2.1.4 Summary

Until now we have defined the volume average, averaged the governing equations and the interface. This has lead to averaged equations, which hopefully are easier to solve than the equations we started with. The next step is to specify models to close the system, and thereafter solve the averaged equations. This could be done using the framework and notation of this section. However, a different path is chosen. When the averaged equations are to be solved, it is easier to incorporate the equations in an existing Navier-Stokes solver when they are written in a cartesian form, and this is done in the next section.

2.2 Mathematical model

In this section, a mathematical model suited for implementation in a numerical code is presented, and the connection between this model and the volume-averaged equations is shown.

2.2.1 Governing equations

Continuity equation

The continuity equation for phase k is

$$\frac{\partial}{\partial t}\left(\alpha_k \rho_k\right) + \frac{\partial}{\partial x_i}\left(\alpha_k \rho_k u_{k,i}\right) = \Gamma_k, \tag{2.26}$$

where ρ_k is the density of phase k, α_k is the volume fraction of phase k, $u_{k,i}$ is the Cartesian velocity component for phase k in the x_i-direction, and Γ_k is the mass transfer rate for phase k.

The corresponding constitutive equations are

$$\sum_{k=1}^{\phi} \alpha_k = 1, \tag{2.27}$$

and

$$\sum_{k=1}^{\phi} \Gamma_k = 0, \tag{2.28}$$

where ϕ is the number of phases involved.

Momentum equation

The momentum equation for phase k in the x_j-direction is

$$\begin{aligned}\frac{\partial}{\partial t}\left(\alpha_k \rho_k u_{k,j}\right) + \frac{\partial}{\partial x_i}\left(\alpha_k \rho_k u_{k,j} u_{k,i}\right) \\ = -\frac{\partial}{\partial x_j}\left(\alpha_k p_k\right) + \frac{\partial}{\partial x_i}\left(\alpha_k \tau_{k,ji}\right) + \alpha_k \rho_k b_{k,j} + \Phi^{\text{if}}_{k,j} + \Omega_{\Gamma_k}.\end{aligned} \tag{2.29}$$

Here, p_k is the pressure of phase k, $\tau_{k,ji}$ is the mean stress tensor including viscous shear stresses and apparent turbulence stresses, and b is the body force per unit mass including gravity. Φ^{if} is the interfacial momentum transfer rate and Ω_{Γ_k} represents interfacial momentum transfer rate due to mass exchange.

2.2.2 Comparison of the formulations

In this section, a term-wise comparison will be made between the momentum Equation (2.20) and the momentum equation as written in Equation (2.29).

Transient term

In Equation (2.20), the transient term of the momentum equation is stated as

$$\frac{\partial}{\partial t}\langle \rho_k \boldsymbol{u}_k \rangle = \frac{\partial}{\partial t}\left(\alpha_k{}^{\mathrm{i}}\langle \rho_k \boldsymbol{u}_k \rangle \right), \tag{2.30}$$

and in Equation (2.29) as

$$\frac{\partial}{\partial t}\left(\alpha_k \rho_k u_{k,j} \right),$$

which implicitly equals

$$\frac{\partial}{\partial t}\left(\alpha_k{}^{\mathrm{i}}\langle \rho_k \rangle {}^{\mathrm{i}}\langle u_{k,j} \rangle \right).$$

Using the first equality of Equation (2.12), we obtain

$${}^{\mathrm{i}}\langle \rho_k \rangle {}^{\mathrm{i}}\langle \boldsymbol{u}_k \rangle = \frac{1}{V_k}\int_{V_k} \rho_k \boldsymbol{u}_k \, dV = {}^{\mathrm{i}}\langle \rho_k \boldsymbol{u}_k \rangle, \tag{2.31}$$

which shows that the two ways of writing the transient term are equivalent.

Body force term

The body force term in Equation (2.20) is written like this:

$$\langle \rho_k \rangle \, \boldsymbol{b},$$

where $\boldsymbol{b}$ is assumed constant in the control volume. In Equation (2.29) it is written like

$$\alpha_k \rho_k b_{k,j},$$

which means

$$\alpha_k{}^{\mathrm{i}}\langle \rho_k \rangle \, b_{k,j}.$$

This shows that there is no difference between the two ways of writing the terms, because $b_{s,j}$ equals the jth component of $\boldsymbol{b}$.

Pressure term

The pressure term of Equation (2.20) is

$$-\nabla \langle p_k \rangle ,$$

and that of Equation (2.29) is

$$-\frac{\partial}{\partial x_j} (\alpha_k p_k) .$$

The two terms are equivalent given that one may write

$$\langle p_k \rangle = \alpha_k{}^{\mathrm{i}} \langle p_k \rangle .$$

Stress term

The stress term is presented like

$$\nabla \cdot \langle \boldsymbol{\tau}_k \rangle ,$$

in Equation (2.20), while in Equation (2.29) the stress term is formulated as

$$\frac{\partial}{\partial x_i} \left(\alpha_k \tau_{k,ji} \right) .$$

Observe that it is permitted to perform volume averaging of $\boldsymbol{\tau}_k$, because its unit is given in force per area. Thus $\langle \boldsymbol{\tau}_k \rangle = \alpha_k{}^{\mathrm{i}} \langle \boldsymbol{\tau}_k \rangle$, and the two formulations agree.

Inertia term

The inertia term is

$$\nabla \cdot \langle \rho_k \boldsymbol{u}_k \boldsymbol{u}_k \rangle .$$

and the momentum Equation (2.29) uses

$$\frac{\partial}{\partial x_i} \left(\alpha_k \rho_k u_{k,j} u_{k,i} \right) ,$$

which equals

$$\frac{\partial}{\partial x_i} \left(\alpha_k{}^{\mathrm{i}} \langle \rho_k \rangle{}^{\mathrm{i}} \left\langle u_{k,j} \right\rangle{}^{\mathrm{i}} \langle u_{k,i} \rangle \right) .$$

If the inertia term is written as:

$$\langle \rho_k \boldsymbol{u}_k \boldsymbol{u}_k \rangle = \alpha_k{}^{\mathrm{i}}\langle \rho_k \rangle^{\mathrm{i}}\langle \boldsymbol{u}_k \rangle^{\mathrm{i}}\langle \boldsymbol{u}_k \rangle + \alpha_k \Delta, \tag{2.32}$$

where Δ is a spatially fluctuating term, which must be modelled, then the formulations agree. A similar term arrives when ensemble averaging is used, (Drew and Passman, 1999, Page 125). In Nigmatulin (1991, Page 37) the fluctuating momentum transfer is referred to as the fluctuating stress tensor and is similar to the Reynolds stresses in turbulent regimes of flow.

Momentum transfer integral due to mass exchange

In Equation (2.29) the interfacial momentum transfer rate term may be regarded as a model for the momentum transfer integral due to mass exchange, or

$$\boldsymbol{\Omega}_{\Gamma_k} = -\frac{1}{V}\int_{\mathcal{A}_k} \rho_k \boldsymbol{u}_k (\boldsymbol{u}_k - \boldsymbol{u}_s) \cdot \boldsymbol{n}_k \, dA, \tag{2.33}$$

where $\boldsymbol{\Omega}_{\Gamma_k}$ is a vector.

Momentum transfer integral due to pressure and stress

The interfacial momentum transfer rate term of Equation (2.29),

$$\Phi^{\mathrm{if}}_{k,j},$$

might be considered to represent a model for the jth component of the momentum transfer integral due to pressure and stress,

$$\frac{1}{V}\int_{\mathcal{A}_k} (-p_k \boldsymbol{n}_k + \boldsymbol{\tau}_k \cdot \boldsymbol{n}_k) \, dA.$$

2.2.3 Closure laws

Models to close the system are presented in this section.

Turbulence

The presence of an interface affects the turbulence structure for the individual phases, (Kataoka and Serizawa, 1989; Kataoka *et al.*, 1992).

Nevertheless, the mean stress tensor and the spatially fluctuating term are often expressed as for single-phase flow, (Moe and Bendiksen, 1993),

$$\tau_{k,ji} + \Delta = \mu_{k,\text{eff}} \left(\frac{\partial u_{k,j}}{\partial x_i} + \frac{\partial u_{k,i}}{\partial x_j} - \frac{2}{3} \frac{\partial u_{k,l}}{\partial x_l} \delta_{ji} \right), \tag{2.34}$$

where the effective viscosity for phase k, $\mu_{k,\text{eff}}$, is given by

$$\mu_{k,\text{eff}} = \mu_k + \mu_k^{\text{T}}. \tag{2.35}$$

Here, μ_k^{T} is the turbulence eddy viscosity, which usually is estimated from characteristic length and time scales of the large-scale turbulence. This can be done by using modified versions of the k-ε model or a mixing-length model. In this thesis, the focus is not on turbulence models, but on boundary conditions and hence a simple model is used,

$$\mu_{k,\text{eff}} = a\mu_k, \tag{2.36}$$

where $a = 100$.

Interfacial drag force

One method to model the interfacial drag force is to impose no-slip conditions at the interface, involving the use of boundary layer functions. This approach is analogous to law-of-the-wall treatment in the modelling of wall boundary layers in turbulent single-phase flows. The other alternative, which is used here, is to allow slip between the phases.

It is customary to assume that the interfacial drag force is proportional to the difference between the two phases squared. This gives the following relation, (Moura and Rezkallah, 1993):

$$\Phi_{k,j} = \sum_{\forall f \neq k} F_j^{kf} \left| \boldsymbol{u}_f - \boldsymbol{u}_k \right| \left(u_{f,j} - u_{k,j} \right) \tag{2.37}$$

where $\left|\boldsymbol{u}_f - \boldsymbol{u}_k\right| = \sqrt{\sum_{j=1}^{d}(u_{f,j} - u_{k,j})^2}$, $d = 2$ for 2D and $d = 3$ for 3D, and F_j^{kf} is modelled by

$$F_j^{kf} = \frac{1}{2}\pi\rho_f\lambda_j^{kf}\frac{A^{kf}}{V}, \tag{2.38}$$

where $\lambda_j^{kf} = \lambda_j^{fk}$ is the interfacial friction factor between the phases f and k. A^{kf}/V is the interfacial area per volume, and is called the interfacial area density. This quantity has to be known in order to make reliable predictions of the interfacial momentum transfers.

The interfacial area should vanish when the fraction of one phase vanishes. Hence, a model expression for F^{kf} can be written as

$$F^{kf} = C\rho_{\mathrm{m}}\alpha_k\alpha_f, \qquad k \neq f. \tag{2.39}$$

C is a coefficient with dimension $1/L$. The appropriate length scale depends on the flow regime. The characteristic length scale for C can be motivated by comparing Equations (2.38) and (2.39), i.e. $L \sim V/A^{kf}$. For bubbly or droplet flows, the relevant length scale is the bubble or droplet radius.

The mixture density, ρ_{m}, is given by

$$\rho_{\mathrm{m}} = \sum_{k=1}^{\phi}(\alpha\rho)_k. \tag{2.40}$$

Mass transfer

In this thesis, no mass transfer phenomena are considered, and hence

$$\Gamma_k = \Omega_{\Gamma_k} = 0. \tag{2.41}$$

Thermodynamical equilibrium

In a closed thermodynamical system where thermodynamical equilibrium is assumed. It is reasonable to take equal pressures in the phases,

$$p_k = p, \tag{2.42}$$

when pressure differences due to surface tension are neglected. During a dynamical process this assumption is not as obvious. However, if the time it takes for the process to reach thermodynamical equilibrium is less than the resolved time, then Equation (2.42) holds. An alternative is to use a relaxation process towards equilibrium, (Saurel and Abgrall, 1999a).

Equation of state

An equation of state has to be provided to close the model. A linear relation between the pressure and density of each phase can be expressed as:

$$p_k = \rho_k c_k^2, \tag{2.43}$$

where c_k is the speed of sound of phase k. This equation of state is based on a polytropic process and perfect gas and is quite accurate for gases. For liquids, however, Equation (2.43) gives the wrong density. Water, for instance, has a sound speed around 1400 m/s and air around 340 m/s, then from Equation (2.43) the density of water will be less than air, which is obviously wrong.

An alternative consists in using the stiffened gas equation of state, which Saurel and Abgrall (1999b) used,

$$p_k = (\gamma_k - 1)\rho_k e_k - \gamma_k \pi_k, \tag{2.44}$$

where γ_s and π_s are material parameters of the phase. e_s is the internal energy. In this thesis the internal energy of the phase is considered constant, and if

$$c_k^2 = (\gamma_k - 1)e_k \tag{2.45}$$

and

$$p_k^\circ = \rho_k^\circ c_k^2 = \gamma_k \pi_k, \tag{2.46}$$

then the following equation of state may be used:

$$p_k = (\rho_k - \rho_k^\circ)c_k^2, \tag{2.47}$$

where ρ_k° is a reference density. For water, a value of $\rho_\mathrm{w}^\circ = 1000\,\mathrm{kg/m^3}$ may be used and for air $\rho_\mathrm{a}^\circ = 0$. By defining $p_k^\circ = \rho_k^\circ c_k^2$, the equation of state may also be written as

$$\rho_k = (p_k - p_k^\circ)c_k^{-2}. \tag{2.48}$$

It should be noted that if the pressures are equal in the two phases, then ρ_1 and ρ_2 are linearly dependent,

$$\rho_1 = \rho_1^\circ + (\rho_2 - \rho_2^\circ)\, c_2^2/c_1^2. \tag{2.49}$$

2.3 Study of the interfacial pressure force

2.3.1 Modelling

In the previous sections it was seen that it is necessary to find a model and an approximation for the integral terms in the continuity and momentum equations. If no mass transfer between the phases takes place, the mass-transfer integral in the momentum Equation (2.20) on page 21 vanishes. Disregarding the interfacial stresses, we are left with the transfer integral due to interface pressure:

$$\frac{1}{V}\int_{\mathcal{A}_k} (-p_k \boldsymbol{n}_k)\, dA. \tag{2.50}$$

Interfacial pressure

Recall Equation (2.18) on page 20. The gradient of the volume fraction is:

$$\boldsymbol{\nabla}\alpha_k = -\frac{1}{V}\int_{\mathcal{A}_k} \boldsymbol{n}_k\, dA. \tag{2.51}$$

From this equation it makes sense to model the integral of Equation (2.50) through the gradient of the volume fraction, and since the integral is evaluated at the interface, the interfacial pressure p_k^i is defined by:

$$\frac{1}{V}\int_{\mathcal{A}_k} (-p_k \boldsymbol{n}_k)\, dA = p_k^i \boldsymbol{\nabla}\alpha_k. \tag{2.52}$$

Models for the interfacial pressure

If constant pressure is assumed in Equation (2.50), then we get:

$$p_k^i = p_k. \tag{2.53}$$

A simple model for the interfacial pressure may then be (Soo, 1990, Chapter 6):

$$p_k^i = B_k p_k, \tag{2.54}$$

where B_k is a coefficient close to 1. When the momentum equations are added, this term should vanish, hence B_k should be equal for both phases.

Other models for the interfacial pressure

Cortes *et al.* (1998) lists different models for the interfacial pressure,

$$p - p_k^i = 0, \tag{2.55}$$

$$p - p_g^i = 0, p - p_l^i = C_p(\alpha_g)\rho_l \left(u_g - u_l\right)^2, \tag{2.56}$$

$$p - p_g^i = p - p_l^i = \alpha_g \delta\rho_l \left(u_g - u_l\right)^2, \tag{2.57}$$

$$p - p_g^i = p - p_l^i = \frac{\alpha_g \alpha_l \rho_l}{\alpha_g \rho_l + \alpha_l \rho_g} \left(u_g - u_l\right)^2. \tag{2.58}$$

For details about these models, see Cortes *et al.* (1998).

2.3.2 Separation by gravity

In this thesis, the simple model, Equation (2.54), is used. In order to determine the value of B_k separation by gravity is studied.

Consider the case where the two phases are at rest, then the momentum equations reduce to:

$$p\,(1 - B_k)\,\frac{\partial \alpha_1}{\partial y} + \alpha_1 \frac{\partial p}{\partial y} = \alpha_1 \rho_1 g \tag{2.59}$$

and

$$p\,(1 - B_k)\,\frac{\partial \alpha_2}{\partial y} + \alpha_2 \frac{\partial p}{\partial y} = \alpha_2 \rho_2 g. \tag{2.60}$$

By adding Equation (2.59) and Equation (2.60):

$$\frac{\partial p}{\partial y} = \rho_{\mathrm{m}} g, \tag{2.61}$$

where $\rho_m = \alpha_1\rho_1 + \alpha_2\rho_2$. Now multiply Equation (2.59) by $\alpha_2\rho_2$ and subtract Equation (2.60) multiplied by $\alpha_1\rho_1$ and arrive at:

$$\frac{\partial\alpha_1}{\partial y} = -\alpha_1\alpha_2\left(\frac{g}{1-B_k}\right)\left(\frac{\rho_2-\rho_1}{p}\right). \tag{2.62}$$

In Equation (2.62), it is assumed that $B_k \neq 1$, and that two phases are present, $0 < \alpha_1 < 1$. With the Equation of state (2.48) the gradient of the volume-fraction becomes:

$$\frac{\partial\alpha_1}{\partial y} = -\alpha_1\alpha_2\left(\frac{g}{1-B_k}\right)\left(\frac{1-p_2^\circ/p}{c_2^2} - \frac{1-p_1^\circ/p}{c_1^2}\right). \tag{2.63}$$

Equation (2.61) and Equation (2.63) are ordinary differential equations.

If the pressure p and the volume fraction α_1 are known at a given y, solutions can be found by integration, either numerically or analytically. Although the purpose at the moment is to study the separation effect of B_k, it should be noted that the solution found may also be used as initial value for a transient computation.

Numerical solution

The ordinary differential equation (ODE) system (2.61) and (2.63) may be solved with any ODE solver, like for instance the Runge-Kutta solver described in Chapter 4 on page 55.

The separation effect of B_k

The separation system, Equation 2.61 and Equation 2.63, is solved numerically for water and air. In Figure 2.2 the volume fraction of air, α_1, and the gauge pressure, $\Delta p = p - p(y=0)$, $p(y=0) = 1\,\text{bar}$, is plotted for different values of B_k. It is observed that the system becomes more and more separated the closer B_k reaches 1.

2.3.3 More arguments for choosing B_k close to unity

If one splits the pressure into

$$p_k = {}^{\text{i}}\langle p_k\rangle + \delta p_k, \tag{2.64}$$

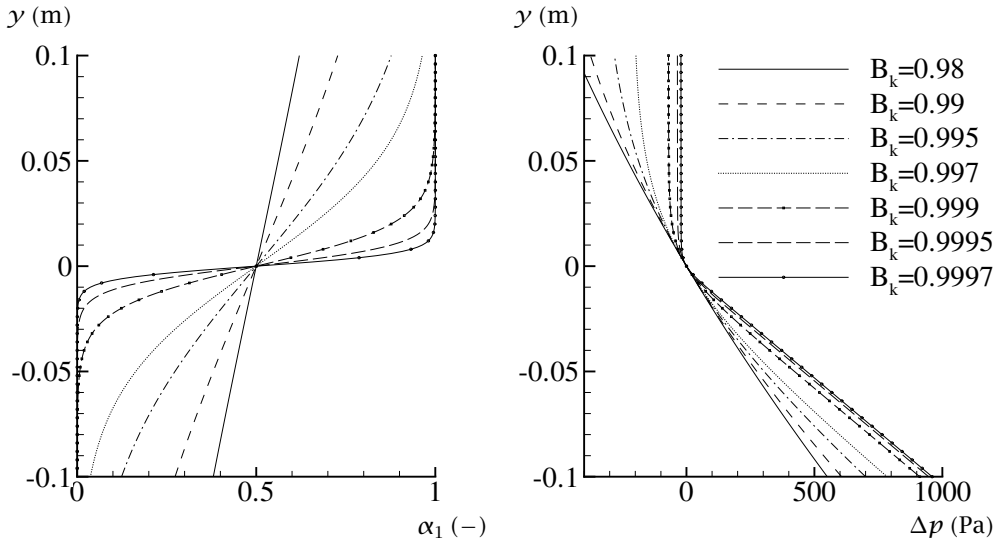

(a) Volume fraction (b) Gauge pressure

Figure 2.2: Separation by gravity for different B_k.

and use this in Equation (2.54), then after some algebra one can write B_k as:

$$B_k = 1 - \frac{\frac{1}{V}\int_{\mathcal{A}_k} \delta p_k \boldsymbol{I} \cdot \boldsymbol{n}_k \, dA}{{}^{\mathrm{i}}\langle p_k \rangle \, \boldsymbol{\nabla} \alpha_k}, \tag{2.65}$$

and argue that δp_k is small in comparison to ${}^{\mathrm{i}}\langle p_k \rangle$. Now it may be concluded that B_k should be chosen close to unity, (Prosperetti and Jones, 1984), (Munkejord *et al.*, 2003) .

2.4 Summary

In this chapter some of the complex modelling work involved in the field of multiphase flow has been reviewed. This work results in model equations, and a summarised version is presented in Appendix B.

As Drew and Passman (1999, Page 237) write:

> It should be recognized that any system of equations that is expected to describe the behaviour of a physical system is a model, and will, at best, describe the subset of phenomena that falls under the limitaions of the model. These limitations are often unwritten and, unfortunately, are often unrecognized.

Therefore, when the equations derived in this chapter are applied to problems of any sort, it is important to review the simplifications to determine whether they are valid in the specific case.

The modelling questions are not further discussed here and the rest of this thesis focuses on finding numerical solutions of the modelled equations.

Chapter 3

Characteristic-based boundary conditions

This chapter presents the characteristic-based boundary conditions (CBC), and is based on Thompson (1987, 1990), Poinsot and Lele (1992), and the review report of Rian (1999).

The method is first presented for single-phase flow and then extended to multiphase flow.

In Section 3.1, the method is shown on a general form, and each step of the process of finding the boundary matrices are outlined. Examples of boundary conditions for the general system are shown in Section 3.2. Boundary conditions for a simplified Euler system are discussed in Section 3.3, and the boundary matrices for the Navier-Stokes equations are presented in Section 3.4, and finally for the multiphase equations in Section 3.5.

3.1 A general derivation

A general system in three dimensions is treated as locally one-dimensional, where the normal direction to the boundary is denoted by x_1. Terms from the other directions are passive in the analysis, meaning that the main effects of the flow are along the normal direction. Often the system of governing equations is written in composite form,

$$\frac{\partial \hat{\boldsymbol{U}}}{\partial t} + \frac{\partial \boldsymbol{F}}{\partial x_1} + \boldsymbol{D} = \boldsymbol{0}, \tag{3.1}$$

where $\hat{\boldsymbol{U}}$ is the vector of the composite variables, $\partial \boldsymbol{F}/\partial x_1$ contains all terms with a derivative with respect to the x_1-direction and $\boldsymbol{D}$ contains all other

terms. To perform the analysis the primitive form of the equation system is needed,

$$\frac{\partial \boldsymbol{U}}{\partial t} + \boldsymbol{A}\frac{\partial \boldsymbol{U}}{\partial x_1} + \boldsymbol{C} = \boldsymbol{0}, \tag{3.2}$$

which can be found by multiplying Equation (3.1) by the inverse of the transformation matrix $\boldsymbol{P}$. $\boldsymbol{P}$ is a Jacobian matrix defined by:

$$\frac{\partial \hat{\boldsymbol{U}}}{\partial t} = \boldsymbol{P}\frac{\partial \boldsymbol{U}}{\partial t}, \tag{3.3}$$

with elements

$$P_{ij} \equiv \frac{\partial \hat{U}_i}{\partial U_j}, \tag{3.4}$$

where $\det(\boldsymbol{P}) \neq 0$. Similarly, the flux-vector term in Equation (3.1) can be written as:

$$\frac{\partial \boldsymbol{F}}{\partial x_1} = \boldsymbol{Q}\frac{\partial \boldsymbol{U}}{\partial x_1}, \tag{3.5}$$

where $\boldsymbol{Q}$ has elements

$$Q_{ij} \equiv \frac{\partial F_i}{\partial U_j}. \tag{3.6}$$

Finally introduce the matrix $\boldsymbol{A}$ and vector $\boldsymbol{C}$:

$$\boldsymbol{A} \equiv \boldsymbol{P}^{-1}\boldsymbol{Q} \quad \text{and} \quad \boldsymbol{C} \equiv \boldsymbol{P}^{-1}\boldsymbol{D}, \tag{3.7}$$

and assume $\boldsymbol{A}$ is diagonalisable, then a diagonal matrix, $\boldsymbol{\Lambda}$, with the eigenvalues λ_i of $\boldsymbol{A}$ along the diagonal, can be obtained by the similarity transformation,

$$\boldsymbol{S}^{-1}\boldsymbol{A}\boldsymbol{S} = \boldsymbol{\Lambda}, \tag{3.8}$$

where $\Lambda_{ij} = 0$ for $i \neq j$ and $\Lambda_{ij} = \lambda_i$ for $i = j$. The columns of the matrix $\boldsymbol{S}$ are the right eigenvectors, $\boldsymbol{r}_j$, and the rows of the inverse matrix, $\boldsymbol{S}^{-1}$, are the left eigenvectors, $\boldsymbol{l}_i^{\mathrm{T}}$ of $\boldsymbol{A}$. Multiply Equation (3.2) with $\boldsymbol{S}^{-1}$,

$$\boldsymbol{S}^{-1}\frac{\partial \boldsymbol{U}}{\partial t} + \boldsymbol{S}^{-1}\boldsymbol{A}\frac{\partial \boldsymbol{U}}{\partial x_1} + \boldsymbol{S}^{-1}\boldsymbol{C} = \boldsymbol{0}, \tag{3.9}$$

and define $\mathscr{L}$ as,

$$\mathscr{L} \equiv \boldsymbol{\Lambda} \boldsymbol{S}^{-1} \frac{\partial \boldsymbol{U}}{\partial x_1} \equiv \boldsymbol{S}^{-1} \boldsymbol{A} \frac{\partial \boldsymbol{U}}{\partial x_1}, \tag{3.10}$$

or in component form,

$$\mathscr{L}_i \equiv \lambda_i \boldsymbol{l}_i^{\mathrm{T}} \frac{\partial \boldsymbol{U}}{\partial x_1}. \tag{3.11}$$

This gives the primitive form of the *time-dependent boundary conditions*,

$$\frac{\partial \boldsymbol{U}}{\partial t} + \boldsymbol{S} \mathscr{L} + \boldsymbol{C} = \boldsymbol{0}, \tag{3.12}$$

and the composite form,

$$\frac{\partial \hat{\boldsymbol{U}}}{\partial t} + \boldsymbol{P} \boldsymbol{S} \mathscr{L} + \boldsymbol{D} = \boldsymbol{0}. \tag{3.13}$$

If the system was linearly hyperbolic with $\boldsymbol{C} = \boldsymbol{0}$ and $\boldsymbol{A}$ independent of $\boldsymbol{U}$, then the change of variables to $\boldsymbol{W} = \boldsymbol{S}^{-1} \boldsymbol{U}$, would give a set of wave equations,

$$\frac{\partial w_i}{\partial t} + \lambda_i \frac{\partial w_i}{\partial x} = 0, \tag{3.14}$$

with characteristic velocities λ_i. When $\lambda_i > 0$, the waves will propagate in the positive x-direction. It is then obvious that w_i cannot be specified at the right boundary, and that w_i must be specified at the left boundary. For a quasi-linear system like the Euler equations, the case is not so simple anymore. However, it turns out that λ_i is the velocity and $\mathscr{L}_i$ is the amplitude of the different waves and $\mathscr{L}_i$ is the proper variable to specify at the boundary (Thompson, 1987).

Specifying boundary conditions in terms of $\mathscr{L}_i$

For outgoing[a] waves the $\mathscr{L}_i$ are calculated from its definition, Equation (3.11). Therefore write the outgoing $\mathscr{L}_i$ as $\mathscr{L}_i^+$ and incoming as $\mathscr{L}_i^-$. The

[a] outgoing means that $\lambda_i > 0$ at $x = x_{\max}$ and $\lambda_i < 0$ at $x = x_{\min}$.

eigenvector matrix $\boldsymbol{S}$ is also split into $\boldsymbol{S}^+$ and $\boldsymbol{S}^-$, where $\boldsymbol{S}^+$ contains eigenvectors with positive eigenvalues. A similar splitting was also done by Bjørhus (1995). Equation (3.12) now reads:

$$\frac{\partial \boldsymbol{U}}{\partial t} + \boldsymbol{S}^+ \mathscr{L}^+ + \boldsymbol{S}^- \mathscr{L}^- + \boldsymbol{C} = \boldsymbol{0}. \tag{3.15}$$

Since $\mathscr{L}^-$ represents incoming waves, this is the only variable left to link the surroundings with the domain. Hence, all boundary conditions must be set through $\mathscr{L}^-$. The task is then to find equations for the unknown $\mathscr{L}^-$ which represents different boundary conditions.

3.2 Typical boundary conditions for the generalised system

A given time-derivative at the boundary

If the time-derivative of a given quantity, like for instance the velocity, is to be specified, an equation for $\mathscr{L}_i^-$ may be found from Equation (3.15),

$$\boldsymbol{S}_i^- \mathscr{L}^- = -\left(\frac{\partial U_i}{\partial t} + \boldsymbol{S}_i^+ \mathscr{L}^+ + C_i \right). \tag{3.16}$$

For a wall at rest the proper boundary condition would be to set the velocity equal to zero at the wall and find the $\mathscr{L}_i^-$ which gives $\partial u / \partial t = 0$.

Given spatial derivative

If $\partial U_i / \partial x_1$ is prescribed, an equation for the unknown $\mathscr{L}^-$ can be found by inverting Equation (3.10),

$$(\boldsymbol{A}^{-1}\boldsymbol{S})_i \mathscr{L} = \frac{\partial U_i}{\partial x_1} \tag{3.17}$$

or

$$(\boldsymbol{A}^{-1}\boldsymbol{S}^-)_i \mathscr{L}^- = \frac{\partial U_i}{\partial x_1} - (\boldsymbol{A}^{-1}\boldsymbol{S}^+)_i \mathscr{L}^+ \tag{3.18}$$

Non-reflecting boundary conditions

Non-reflecting boundary conditions may be achieved by setting the amplitude of the incoming wave to zero, i.e. $\mathscr{L}_i^- = 0$. This may, however, in some cases lead to drifting values of the variable at the boundary and hence in the whole field.

Partially reflecting boundary conditions

A way to overcome drifting values is to specify $\partial U_i/\partial t$ using a PID controller (three-mode controller):

$$\boldsymbol{S}_i^- \mathscr{L}^- = \left(\boldsymbol{S}_i^- \mathscr{L}^-\right)^\circ + \frac{K_P}{T}\Delta U_i + \frac{K_I}{T^2}\int_0^t \Delta U_i \, d\tau + K_D \frac{\partial U_i}{\partial t}, \tag{3.19}$$

where $\Delta U_i = (U_i - U_i^\infty)$, T is the integral time, K_P is the proportional gain, K_I is the integral gain, K_D is the derivative gain and a start term for the controller $\left(\boldsymbol{S}_i^- \mathscr{L}^-\right)^\circ$. The start term can be based on an analytical solution, a previous simulation or simply set to zero. Inserting $\partial U_i/\partial t$ from Equation (3.15) gives:

$$\begin{aligned}\boldsymbol{S}_i^- \mathscr{L}^- = \mathrm{PID}(U_i) \equiv \frac{1}{(1+K_D)} \\ \cdot \left(\left(\boldsymbol{S}_i^- \mathscr{L}^-\right)^\circ + \frac{K_P}{T}\Delta U_i + \frac{K_I}{T^2}\int_0^t \Delta U_i \, d\tau - K_D\left(\boldsymbol{S}_i^+ \mathscr{L}^+ + C_i\right)\right).\end{aligned} \tag{3.20}$$

The reasoning behind this method is presented in Section 3.3.2. The discussion continues with the Euler and the Navier-Stokes equations in the next section.

3.3 Single-phase Euler equations

The Euler equations in one-dimension reads:

$$\frac{\partial}{\partial t}(\rho) + \frac{\partial}{\partial x}(\rho u) = 0, \tag{3.21}$$

$$\frac{\partial}{\partial t}(\rho u) + \frac{\partial}{\partial x}\left(\rho u^2 + p\right) = 0, \tag{3.22}$$

and the equation of state

$$p + p^\circ = \rho c^2, \tag{3.23}$$

where $p^\circ = \rho^\circ c^2$ is the reference pressure, ρ° is the reference density, and c is the speed of sound.

3.3.1 Boundary matrices for the Euler equations

In this section, the boundary matrices for the Euler equations in one dimension, also referred to as the LODI (locally one-dimensional inviscid) relations are presented.

The composite, primitive and the flux-vector from Section 3.1 become:

$$\hat{\boldsymbol{U}} = \begin{bmatrix} \rho \\ \rho u \end{bmatrix}, \quad \boldsymbol{U} = \begin{bmatrix} p \\ u \end{bmatrix}, \quad \text{and} \quad \boldsymbol{F} = \begin{bmatrix} \rho u \\ \rho u^2 + p \end{bmatrix}. \tag{3.24}$$

The transformation matrix and the inverse are

$$\boldsymbol{P} = \begin{bmatrix} c^{-2} & 0 \\ u c^{-2} & \rho \end{bmatrix}, \quad \text{and} \quad \boldsymbol{P}^{-1} = \begin{bmatrix} c^2 & 0 \\ -u/\rho & 1/\rho \end{bmatrix}. \tag{3.25}$$

The system matrix and the eigenvalue matrix are

$$\boldsymbol{A} = \begin{bmatrix} u & \rho c^2 \\ 1/\rho & u \end{bmatrix}, \quad \text{and} \quad \boldsymbol{\Lambda} = \begin{bmatrix} u - c & 0 \\ 0 & u + c \end{bmatrix}. \tag{3.26}$$

The eigenvector matrix and the inverse

$$\boldsymbol{S} = 1/2 \begin{bmatrix} 1 & 1 \\ -1/(\rho c) & 1/(\rho c) \end{bmatrix}, \quad \text{and} \quad \boldsymbol{S}^{-1} = \begin{bmatrix} 1 & -\rho c \\ 1 & \rho c \end{bmatrix}. \tag{3.27}$$

When subsonic flow ($|u| < c$) is assumed, the eigenvector matrix at the upper boundary, ($x = x_{\max}$), is split into:

$$\boldsymbol{S}^{+} = 1/2 \begin{bmatrix} 1 \\ 1/(\rho c) \end{bmatrix}, \quad \text{and} \quad \boldsymbol{S}^{-} = 1/2 \begin{bmatrix} 1 \\ -1/(\rho c) \end{bmatrix}. \tag{3.28}$$

We can also find $\mathscr{L}^{+}$,

$$\mathscr{L}^{+} = \mathscr{L}_2 = (u + c) \left(\frac{\partial p}{\partial x} + \rho c \frac{\partial u}{\partial x} \right). \tag{3.29}$$

For the lower boundary, ($x = x_{\min}$), the eigenvectors and $\mathscr{L}^{+}$ are

$$\boldsymbol{S}^{+} = 1/2 \begin{bmatrix} 1 \\ -1/(\rho c) \end{bmatrix}, \quad \boldsymbol{S}^{-} = 1/2 \begin{bmatrix} 1 \\ 1/(\rho c) \end{bmatrix}, \tag{3.30}$$

and

$$\mathscr{L}^{+} = \mathscr{L}_1 = (u - c) \left(\frac{\partial p}{\partial x} - \rho c \frac{\partial u}{\partial x} \right). \tag{3.31}$$

3.3.2 Non-reflecting boundary conditions

In this section, the Euler equations are discussed with respect to non-reflecting and partially reflecting boundary conditions. Equation (3.12) now becomes:

$$\begin{bmatrix} \dfrac{\partial p}{\partial t} \\ \dfrac{\partial u}{\partial t} \end{bmatrix} + 1/2 \begin{bmatrix} 1 & 1 \\ -1/(\rho c) & 1/(\rho c) \end{bmatrix} \begin{bmatrix} \mathscr{L}_1 \\ \mathscr{L}_2 \end{bmatrix} = \begin{bmatrix} 0 \\ 0 \end{bmatrix}, \tag{3.32}$$

or,

$$\frac{\partial p}{\partial t} + \frac{1}{2}(\mathscr{L}_2 + \mathscr{L}_1) = 0, \tag{3.33}$$

and

$$\frac{\partial u}{\partial t} + \frac{1}{2\rho c}(\mathscr{L}_2 - \mathscr{L}_1) = 0. \tag{3.34}$$

$\mathscr{L}_2$ may be eliminated from the equations if we rewrite Equation (3.34)

$$\mathscr{L}_2 = \mathscr{L}_1 - 2\rho c \frac{\partial u}{\partial t}, \tag{3.35}$$

and insert this in the pressure Equation (3.33),

$$\frac{\partial p}{\partial t} - \rho c \frac{\partial u}{\partial t} + \mathscr{L}_1 = 0. \tag{3.36}$$

By setting $\mathscr{L}_1 = 0$, the non-reflecting boundary condition used by Rudy and Strikwerda (1980) is found, see also the footnote on page 111 of Poinsot and Lele (1992).

Drifting pressure

It is known that specifying $\mathscr{L}_1 = 0$ may lead to a drifting pressure, and by studying Equation (3.33) and Equation (3.34) it is easy to realize why it happens. First note that a steady solution is only possible when $\mathscr{L}_2 = 0$, or $\partial p/\partial x = -\rho c \partial u/\partial x$. When using the Euler equations in 1D it is often the case that $\partial p/\partial x = \partial u/\partial x = 0$ in the steady solution and hence no drifting pressure will occur. A way to represent 2D viscous effects in a 1D-simulation is to use friction factors. By adding a wall friction term $f|u|u$ to Equation (3.34), Equation (3.36) now becomes:

$$\frac{\partial p}{\partial t} - \rho c \frac{\partial u}{\partial t} + \mathscr{L}_1 = \rho c f |u| u. \tag{3.37}$$

When $\mathscr{L}_1 = 0$ and $\partial u/\partial t = 0$ is specified at the other boundary, $\partial u/\partial t \to 0$ at this boundary as well. Equation (3.37) is reduced to:

$$\frac{\partial p}{\partial t} = \rho c f |u| u. \tag{3.38}$$

It is now clear that the pressure will drift unless the velocity equals zero.

Partially reflecting boundary conditions

A way to overcome the problem of drifting pressure was proposed by Rudy and Strikwerda (1980):

$$\frac{\partial p}{\partial t} - \rho c \frac{\partial u}{\partial t} + k(p - p_\infty) = 0, \tag{3.39}$$

where p_∞ is the pressure at some reference state located at infinity. Rudy and Strikwerda (1981) studied the behaviour of a linearised Navier-Stokes system and claimed that the coefficient k should be of the form

$k = \sigma(1 - \mathscr{M}^2)c/L$. $\mathscr{M}$ is the maximum Mach number in the flow, L is a characteristic size of the domain, and σ is a constant. They derived an optimal value for σ around 0.27, but their tests showed that a value of 0.58 provides better results. Poinsot and Lele (1992) compared Equation (3.39) and several other methods, they arrived at setting $\mathscr{L}_1 = k(p - p_\infty)$ with σ=0.25 and using this in all equations at the boundary. They also suggested that the method might perform better if an analytical expression for $\mathscr{L}_1$ were available, then the expression for $\mathscr{L}_1$ becomes:

$$\mathscr{L}_1 = \mathscr{L}_1^{\text{exact}} + k(p - p_\infty). \tag{3.40}$$

Chaturvedi (1999) claimed that this is not the optimum choice and investigated the following formulations:

$$\frac{\partial p}{\partial t} - \rho c \frac{\partial u}{\partial t} + k|p - p_\infty|^z = 0, \tag{3.41}$$

$$\frac{\partial p}{\partial t} - \rho c \frac{\partial u}{\partial t} + k|e^{(p-p_\infty)} - 1|^z = 0, \tag{3.42}$$

and

$$\frac{\partial p}{\partial t} - \rho c \frac{\partial u}{\partial t} + k\left(\left|\frac{1}{\ln(p - p_\infty)}\right|\right)^z = 0, \tag{3.43}$$

where k and z are coefficients, for faster convergence. The optimum values of k and z are problem dependent.

PID controller

If we consider the procedure of modifying Equation (3.39) in terms of control engineering, the methods of the previous section are recognised as controllers. Specifically, the methods used by Rudy and Strikwerda (1980) and Poinsot and Lele (1992) are recognised as P-controllers for $\partial p/\partial t$. Sutherland and Kennedy (2003) mentions, in a recent paper, that they want to control $\mathscr{L}_i^-$.

It is known from control engineering that a PID-controller performs better than a P-controller, see a standard textbook on control engineering like Haugen (1994). With $\Delta p = (p - p_\infty)$, a PID-controller for $\partial p/\partial t$ may be written as:

$$\mathscr{L}_1 = \mathscr{L}_1^\circ + \frac{K_P}{T}\Delta p + \frac{K_I}{T^2}\int_0^t \Delta p \, d\tau + K_D \frac{\partial}{\partial t}(\Delta p), \tag{3.44}$$

and with $\partial p/\partial t$ from Equation (3.33), $\mathscr{L}_1$ becomes:

$$\mathscr{L}_1 = \frac{1}{1+K_D}\left(\mathscr{L}_1^\circ + \frac{K_P}{T}\Delta p + \frac{K_I}{T^2}\int_0^t \Delta p\, d\tau - \frac{K_D}{2}\mathscr{L}_2\right). \tag{3.45}$$

The P-controller of Poinsot and Lele (1992), Equation (3.40), is found if we set $\mathscr{L}_1^\circ = \mathscr{L}_1^{\text{exact}}$, $K_P = kT$ and $K_I = K_D = 0$.

Controlling other variables than pressure

Kim and Lee (2000) used the same approach as Poinsot and Lele (1992), at the inlet in addition to the outlet, i.e. by specifying $\mathscr{L}_i^-$ on the form,

$$\mathscr{L}_i^- = K_{\text{in}}(u - u^\infty) + K_{\text{in}}(v - v^\infty). \tag{3.46}$$

Thus it makes sense to use a PID-controller at the inlet as well. In this case use Equation (3.20) to find an equation for the unknown $\mathscr{L}_i^-$.

It is also possible to use a controller at walls, but this may lead to mass flowing through the wall during the computations, hence either Equation (3.16) or an extrapolation procedure should be used instead.

3.4 CBC applied to the Navier-Stokes equations

Poinsot and Lele (1992) extends the CBC method to the Navier-Stokes equations based on well-posedness analyses. It is called Navier-Stokes characteristic boundary conditions (NSCBC). According to well-posedness analyses, the Navier-Stokes equations needs more boundary conditions than the Euler equations. Therefore the boundary conditions are divided into inviscid and viscous boundary conditions. The inviscid conditions are set as for the Euler equations, i.e. in terms of $\mathscr{L}_i$. The viscous conditions are set directly in the momentum equation at the boundary.

3.4.1 Navier-Stokes equations in two dimensions

This section presents the NSCBC method using the notation of the present thesis. It is carried out similarly to what was done in Section 3.3.

The Navier-Stokes equations in two dimensions reads:

Continuity equation

$$\frac{\partial \rho}{\partial t} + \frac{\partial}{\partial x}(\rho u) + \frac{\partial}{\partial y}(\rho v) = 0$$

Momentum equation

$$\frac{\partial}{\partial t}(\rho u) + \frac{\partial}{\partial x}(\rho u u) + \frac{\partial}{\partial y}(\rho u v) = -\frac{\partial p}{\partial x} + \frac{\partial \tau_{xx}}{\partial x} + \frac{\partial \tau_{xy}}{\partial y} + \rho g_x$$

$$\frac{\partial}{\partial t}(\rho v) + \frac{\partial}{\partial x}(\rho v u) + \frac{\partial}{\partial y}(\rho v v) = -\frac{\partial p}{\partial y} + \frac{\partial \tau_{yx}}{\partial x} + \frac{\partial \tau_{yy}}{\partial y} + \rho g_y$$

Viscous stress tensor

$$\tau_{jk} = \mu\left(\frac{\partial u_j}{\partial x_k} + \frac{\partial u_k}{\partial x_j} - \frac{2}{3}\frac{\partial u_i}{\partial x_i}\delta_{jk}\right)$$

$$\tau_{xx} = \mu\left(\frac{4}{3}\frac{\partial u}{\partial x} - \frac{2}{3}\frac{\partial v}{\partial y}\right)$$

$$\tau_{xy} = \tau_{yx} = \mu\left(\frac{\partial u}{\partial y} + \frac{\partial u}{\partial x}\right)$$

Equation of state

$$p + p^\circ = \rho c^2, \tag{3.47}$$

where $p^\circ = \rho^\circ c^2$ is the reference pressure, ρ° is the reference density and c is the speed of sound.

Boundary matrices

The suffix 1D refers to the matrices for the Euler equations in Section 3.3.

$$\hat{\boldsymbol{U}} = \begin{bmatrix} \rho \\ \rho u \\ \rho v \end{bmatrix} = \begin{bmatrix} \hat{\boldsymbol{U}}_{1\mathrm{D}} \\ \rho v \end{bmatrix}, \quad \boldsymbol{U} = \begin{bmatrix} p \\ u \\ v \end{bmatrix} = \begin{bmatrix} \boldsymbol{U}_{1\mathrm{D}} \\ v \end{bmatrix}, \tag{3.48}$$

$$\boldsymbol{P} = \begin{bmatrix} c^{-2} & 0 & 0 \\ uc^{-2} & \rho & 0 \\ vc^{-2} & 0 & \rho \end{bmatrix}, \quad \boldsymbol{P}^{-1} = \begin{bmatrix} c^2 & 0 & 0 \\ -u/\rho & 1/\rho & 0 \\ -v/\rho & 0 & 1/\rho \end{bmatrix}, \tag{3.49}$$

$$\boldsymbol{P} = \begin{bmatrix} \boldsymbol{P}_{1D} & & 0 \\ vc^{-2} & 0 & \rho \end{bmatrix}, \quad \boldsymbol{P}^{-1} = \begin{bmatrix} \boldsymbol{P}_{1D}^{-1} & & 0 \\ -v/\rho & 0 & 1/\rho \end{bmatrix}, \tag{3.50}$$

$$\boldsymbol{A} = \begin{bmatrix} u & \rho c^2 & 0 \\ 1/\rho & u & 0 \\ 0 & 0 & u \end{bmatrix}, \quad \boldsymbol{\Lambda} = \begin{bmatrix} u-c & 0 & 0 \\ 0 & u+c & 0 \\ 0 & 0 & u \end{bmatrix}, \tag{3.51}$$

$$\boldsymbol{A} = \begin{bmatrix} \boldsymbol{A}_{1D} & & 0 \\ 0 & 0 & u \end{bmatrix}, \quad \boldsymbol{\Lambda} = \begin{bmatrix} \boldsymbol{\Lambda}_{1D} & & 0 \\ 0 & 0 & u \end{bmatrix}, \tag{3.52}$$

$$\boldsymbol{S} = 1/2 \begin{bmatrix} 1 & 1 & 0 \\ -1/(\rho c) & 1/(\rho c) & 0 \\ 0 & 0 & 2 \end{bmatrix}, \quad \boldsymbol{S}^{-1} = \begin{bmatrix} 1 & -\rho c & 0 \\ 1 & \rho c & 0 \\ 0 & 0 & 1 \end{bmatrix}, \tag{3.53}$$

$$\boldsymbol{S} = \begin{bmatrix} \boldsymbol{S}_{1D} & & 0 \\ 0 & 0 & 1 \end{bmatrix}, \quad \boldsymbol{S}^{-1} = \begin{bmatrix} \boldsymbol{S}_{1D}^{-1} & & 0 \\ 0 & 0 & 1 \end{bmatrix}, \tag{3.54}$$

$$\boldsymbol{D} = \begin{bmatrix} \frac{\partial}{\partial y}(\rho v) \\ \frac{\partial}{\partial y}(\rho uv) - (\frac{\partial \tau_{xx}}{\partial x} + \frac{\partial \tau_{xy}}{\partial y} + \rho g_x) \\ \frac{\partial}{\partial y}(\rho vv) + \frac{\partial p}{\partial y} - (\frac{\partial \tau_{yx}}{\partial x} + \frac{\partial \tau_{yy}}{\partial y} + \rho g_y) \end{bmatrix} \tag{3.55}$$

3.4.2 Boundary conditions for two-dimensional Poiseuille flow

Poinsot and Lele (1992) used poiseuille flow in one of their examples, this will also be done in the present work, and therefore the specific boundary conditions for this case are described.

The inlet is located at $x = 0$, the outlet at $x = L$, and at $y = \pm h$ there are no-slip walls. In addition to the inviscid boundary conditions, the NSCBC method needs viscous conditions. The additional viscous conditions are shown for a subsonic outlet, inlet and no-slip walls.

Subsonic outlet

One viscous condition is needed at the outlet, $\partial \tau_{xy}/\partial x = 0$.

Subsonic inlet

For a non-reflecting inlet the viscous condition, $\partial \tau_{xx}/\partial x = 0$, is used.

Subsonic wall

According to the NSCBC method, a subsonic wall does not need viscous conditions. It is sufficient to set the velocities to zero and solve the continuity equation. When it comes to multiphase flow, the CBC approach is computationally expensive, and therefore one should avoid using it whenever possible. An alternative is to extrapolate the pressure to the wall. In order to find out how extrapolation works in conjunction with the NSCBC method, extrapolation of the pressure to the wall is used instead.

Corners

A corner is a special point which is a member of two boundaries at the same time. In the NSCBC method, a second LODI-system is used to compute the corner. Bjørhus (1995) suggests that the corner point may be transformed to a direction pointing out of the corner. However, in this thesis, a corner is considered as a part of one of the boundaries only. For the channel-flow computations in this thesis, the corner is part of the no-slip wall.

3.5 CBC applied to the multiphase equations

In this section, the multiphase equations in one dimension, with no gravity, no viscous terms, no interface friction, no phase transfer, with an interface pressure model and arbitrary equation of state are written on the form of Equation (3.13) on page 37. The multiphase equations reduce to

$$\frac{\partial}{\partial t}\left(\alpha_1\rho_1\right) + \frac{\partial}{\partial x}\left(\alpha_1\rho_1 u_1\right) = 0, \tag{3.56}$$

$$\frac{\partial}{\partial t}\left(\alpha_2\rho_2\right) + \frac{\partial}{\partial x}\left(\alpha_2\rho_2 u_2\right) = 0, \tag{3.57}$$

$$\frac{\partial}{\partial t}\left(\alpha_1\rho_1 u_1\right) + \frac{\partial}{\partial x}\left(\alpha_1\rho_1 u_1^2 + \alpha_1 p\right) = \Phi_{1,1}^{\text{if}}, \tag{3.58}$$

and

$$\frac{\partial}{\partial t}\left(\alpha_2\rho_2 u_2\right) + \frac{\partial}{\partial x}\left(\alpha_2\rho_2 u_2^2 + \alpha_2 p\right) = \Phi_{2,1}^{\text{if}}. \tag{3.59}$$

The interface pressure model from Chapter 2 is:

$$\Phi_{k,i}^{\text{if}} = B_k p \frac{\partial \alpha_k}{\partial x_i}. \tag{3.60}$$

3.5.1 Expressions for an arbitrary equation of state

With the composite and primitive vector as

$$\hat{\boldsymbol{U}} = \begin{bmatrix} \alpha_1\rho_1 \\ \alpha_2\rho_2 \\ \alpha_1\rho_1 u_1 \\ \alpha_2\rho_2 u_2 \end{bmatrix} \text{ and } \boldsymbol{U} = \begin{bmatrix} \alpha_1 \\ p \\ u_1 \\ u_2 \end{bmatrix}, \tag{3.61}$$

the transformation matrix $\boldsymbol{P}$ will be:

$$\begin{bmatrix} \frac{\partial}{\partial \alpha_1}\left(\alpha_1\rho_1\right) & \frac{\partial}{\partial p}\left(\alpha_1\rho_1\right) & \frac{\partial}{\partial u_1}\left(\alpha_1\rho_1\right) & \frac{\partial}{\partial u_2}\left(\alpha_1\rho_1\right) \\ \frac{\partial}{\partial \alpha_1}\left(\alpha_2\rho_2\right) & \frac{\partial}{\partial p}\left(\alpha_2\rho_2\right) & \frac{\partial}{\partial u_1}\left(\alpha_2\rho_2\right) & \frac{\partial}{\partial u_2}\left(\alpha_2\rho_2\right) \\ \frac{\partial}{\partial \alpha_1}\left(\alpha_1\rho_1 u_1\right) & \frac{\partial}{\partial p}\left(\alpha_1\rho_1 u_1\right) & \frac{\partial}{\partial u_1}\left(\alpha_1\rho_1 u_1\right) & \frac{\partial}{\partial u_2}\left(\alpha_1\rho_1 u_1\right) \\ \frac{\partial}{\partial \alpha_1}\left(\alpha_2\rho_2 u_2\right) & \frac{\partial}{\partial p}\left(\alpha_2\rho_2 u_2\right) & \frac{\partial}{\partial u_1}\left(\alpha_2\rho_2 u_2\right) & \frac{\partial}{\partial u_2}\left(\alpha_2\rho_2 u_2\right) \end{bmatrix}, \tag{3.62}$$

or simplified without saying anything about the equation of state:

$$\boldsymbol{P} = \begin{bmatrix} \rho_1 & \alpha_1 \frac{\partial \rho_1}{\partial p} & 0 & 0 \\ -\rho_2 & \alpha_2 \frac{\partial \rho_2}{\partial p} & 0 & 0 \\ \rho_1 u_1 & \alpha_1 u_1 \frac{\partial \rho_1}{\partial p} & \alpha_1 \rho_1 & 0 \\ -\rho_2 u_2 & \alpha_2 u_2 \frac{\partial \rho_2}{\partial p} & 0 & \alpha_2 \rho_2 \end{bmatrix} \tag{3.63}$$

and its inverse, with $\varsigma = \alpha_1 \rho_2 \frac{\partial \rho_1}{\partial p} + \alpha_2 \rho_1 \frac{\partial \rho_2}{\partial p}$,

$$\boldsymbol{P}^{-1} = \varsigma^{-1} \begin{bmatrix} \alpha_2 \frac{\partial \rho_2}{\partial p} & -\alpha_1 \frac{\partial \rho_1}{\partial p} & 0 & 0 \\ \rho_2 & \rho_1 & 0 & 0 \\ -u_1 \varsigma / (\alpha_1 \rho_1) & 0 & \varsigma / (\alpha_1 \rho_1) & 0 \\ 0 & -u_2 \varsigma / (\alpha_2 \rho_2) & 0 & \varsigma / (\alpha_2 \rho_2) \end{bmatrix}. \tag{3.64}$$

The flux vector is

$$\boldsymbol{F} = \begin{bmatrix} \alpha_1 \rho_1 u_1 \\ \alpha_2 \rho_2 u_2 \\ \alpha_1 \rho_1 u_1^2 + \alpha_1 p \\ \alpha_2 \rho_2 u_2^2 + \alpha_2 p \end{bmatrix}, \tag{3.65}$$

and this gives us $\boldsymbol{Q}$ from Equation (3.5), $\boldsymbol{Q}$ is split over two lines for better readability,

$$\begin{aligned} \boldsymbol{Q} = \begin{bmatrix} \frac{\partial}{\partial \alpha_1}(\alpha_1 \rho_1 u_1) & \frac{\partial}{\partial p}(\alpha_1 \rho_1 u_1) \\ \frac{\partial}{\partial \alpha_1}(\alpha_2 \rho_2 u_2) & \frac{\partial}{\partial p}(\alpha_2 \rho_2 u_2) \\ \frac{\partial}{\partial \alpha_1}\left(\alpha_1 \rho_1 u_1^2 + \alpha_1 p\right) & \frac{\partial}{\partial p}\left(\alpha_1 \rho_1 u_1^2 + \alpha_1 p\right) \\ \frac{\partial}{\partial \alpha_1}\left(\alpha_2 \rho_2 u_2^2 + \alpha_2 p\right) & \frac{\partial}{\partial p}\left(\alpha_2 \rho_2 u_2^2 + \alpha_2 p\right) \end{bmatrix} \\ \begin{bmatrix} \frac{\partial}{\partial u_1}(\alpha_1 \rho_1 u_1) & \frac{\partial}{\partial u_2}(\alpha_1 \rho_1 u_1) \\ \frac{\partial}{\partial u_1}(\alpha_2 \rho_2 u_2) & \frac{\partial}{\partial u_2}(\alpha_2 \rho_2 u_2) \\ \frac{\partial}{\partial u_1}\left(\alpha_1 \rho_1 u_1^2 + \alpha_1 p\right) & \frac{\partial}{\partial u_2}\left(\alpha_1 \rho_1 u_1^2 + \alpha_1 p\right) \\ \frac{\partial}{\partial u_1}\left(\alpha_2 \rho_2 u_2^2 + \alpha_2 p\right) & \frac{\partial}{\partial u_2}\left(\alpha_2 \rho_2 u_2^2 + \alpha_2 p\right) \end{bmatrix}. \end{aligned} \tag{3.66}$$

By evaluating the derivatives, $\boldsymbol{Q}$ is simplified to

$$\boldsymbol{Q} = \begin{bmatrix} \rho_1 u_1 & \alpha_1 u_1 \frac{\partial \rho_1}{\partial p} & \alpha_1 \rho_1 & 0 \\ -\rho_2 u_2 & \alpha_2 u_2 \frac{\partial \rho_2}{\partial p} & 0 & \alpha_2 \rho_2 \\ \rho_1 u_1^2 + p & \alpha_1 (u_1^2 \frac{\partial \rho_1}{\partial p} + 1) & 2\alpha_1 \rho_1 u_1 & 0 \\ -\rho_2 u_2^2 - p & \alpha_2 (u_2^2 \frac{\partial \rho_2}{\partial p} + 1) & 0 & 2\alpha_2 \rho_2 u_2 \end{bmatrix}. \tag{3.67}$$

Taking into consideration the interfacial pressure model, Equation (3.60), we get:

$$\boldsymbol{Q} = \begin{bmatrix} \rho_1 u_1 & \alpha_1 u_1 \frac{\partial \rho_1}{\partial p} & \alpha_1 \rho_1 & 0 \\ -\rho_2 u_2 & \alpha_2 u_2 \frac{\partial \rho_2}{\partial p} & 0 & \alpha_2 \rho_2 \\ \rho_1 u_1^2 + p(1-B) & \alpha_1 (u_1^2 \frac{\partial \rho_1}{\partial p} + 1) & 2\alpha_1 \rho_1 u_1 & 0 \\ -\rho_2 u_2^2 - p(1-B) & \alpha_2 (u_2^2 \frac{\partial \rho_2}{\partial p} + 1) & 0 & 2\alpha_2 \rho_2 u_2 \end{bmatrix}. \quad (3.68)$$

This gives us $\boldsymbol{A} = \boldsymbol{P}^{-1}\boldsymbol{Q}$ with $\varsigma = \alpha_1 \rho_2 \frac{\partial \rho_1}{\partial p} + \alpha_2 \rho_1 \frac{\partial \rho_2}{\partial p}$,

$$\boldsymbol{A} = \varsigma^{-1} \begin{bmatrix} \alpha_2 \rho_1 u_1 \frac{\partial \rho_2}{\partial p} + \alpha_1 \rho_2 u_2 \frac{\partial \rho_1}{\partial p} & \alpha_1 \alpha_2 (u_1 - u_2) \frac{\partial \rho_1}{\partial p} \frac{\partial \rho_2}{\partial p} & \alpha_1 \alpha_2 \rho_1 \frac{\partial \rho_2}{\partial p} & -\alpha_1 \alpha_2 \rho_2 \frac{\partial \rho_1}{\partial p} \\ \rho_1 \rho_2 (u_1 - u_2) & \alpha_1 \rho_2 u_1 \frac{\partial \rho_1}{\partial p} + \alpha_2 \rho_1 u_2 \frac{\partial \rho_2}{\partial p} & \alpha_1 \rho_1 \rho_2 & \alpha_2 \rho_1 \rho_2 \\ p(1-B)\varsigma/(\alpha_1 \rho_1) & \varsigma/\rho_1 & \varsigma u_1 & 0 \\ -p(1-B)\varsigma/(\alpha_2 \rho_2) & \varsigma/\rho_2 & 0 & \varsigma u_2 \end{bmatrix}. \quad (3.69)$$

The extension to three-dimensions is shown in Appendix A. To continue the discussion, the equation of state will be specified in order to find the eigenvalues and the eigenvectors.

3.5.2 Specified equation of state

Recall the equation of state from Chapter 2, Equation (2.47) on page 29,

$$\rho_k = (p + p_k^\circ)/c_k^2, \quad (3.70)$$

where $p_k^\circ = \rho_k^\circ c_k^2$ is the reference pressure, ρ_k° is the reference density and c_k is the speed of sound for phase k. The derivative of the densities with respect to p is:

$$\frac{\partial \rho_k}{\partial p} = c_k^{-2}. \quad (3.71)$$

The transformation matrix $\boldsymbol{P}$ and the primitive system matrix $\boldsymbol{A}$ now becomes,

$$\boldsymbol{P} = \begin{bmatrix} \rho_1 & \alpha_1 c_1^{-2} & 0 & 0 \\ -\rho_2 & \alpha_2 c_2^{-2} & 0 & 0 \\ \rho_1 u_1 & \alpha_1 u_1 c_1^{-2} & \alpha_1 \rho_1 & 0 \\ -\rho_2 u_2 & \alpha_2 u_2 c_2^{-2} & 0 & \alpha_2 \rho_2 \end{bmatrix}, \tag{3.72}$$

$$\boldsymbol{A} = \tilde{\varsigma}^{-1} \cdot \begin{bmatrix} (\alpha_1 \tilde{p}_2 u_2 + \alpha_2 \tilde{p}_1 u_1) & \alpha_1 \alpha_2 (u_1 - u_2) & \alpha_1 \alpha_2 \tilde{p}_1 & -\alpha_1 \alpha_2 \tilde{p}_2 \\ \tilde{p}_2 \tilde{p}_1 (u_1 - u_2) & (\alpha_1 u_1 \tilde{p}_2 + \alpha_2 u_2 \tilde{p}_1) & \alpha_1 \tilde{p}_1 \tilde{p}_2 & \alpha_2 \tilde{p}_1 \tilde{p}_2 \\ p(1 - B_x)\tilde{\varsigma}/(\alpha_1 \rho_1) & \tilde{\varsigma}/\rho_1 & u_1 \tilde{\varsigma} & 0 \\ -p(1 - B_x)\tilde{\varsigma}/(\alpha_2 \rho_2) & \tilde{\varsigma}/\rho_2 & 0 & u_2 \tilde{\varsigma} \end{bmatrix}, \tag{3.73}$$

where $\tilde{p}_1 = p + p_1^\circ$, $\tilde{p}_2 = p + p_2^\circ$ and $\tilde{\varsigma} = \alpha_1 \tilde{p}_2 + \alpha_2 \tilde{p}_1$. To find the eigenvalues of $\boldsymbol{A}$, a fourth-order equation for the characteristic polynomial has to be solved. This can be done numerically for instance by a program package like LAPACK[b]. Since a linear combination of any eigenvectors may be used as a eigenvector basis, there are infinitely many possible choices of eigenvectors. Here, the eigenvectors are chosen such that the condition number of the eigenvector matrix is as low as possible.

Example with analytical eigenvalues

Analytical solutions can be found if we let $B_k = 0$, $p_1^\circ = 0$ and p_2° is chosen arbitrarily, then the eigenvalues are:

$$\boldsymbol{\lambda}^{\mathrm{T}} = \left[u_1 - c_1, u_1 + c_1, u_2 - c_2 \sqrt{\frac{p}{p + \alpha_1 p_2^\circ}}, u_2 + c_2 \sqrt{\frac{p}{p + \alpha_1 p_2^\circ}} \right]. \tag{3.74}$$

The eigenvectors can also be found analytically, but the output will be pages long. It is therefore recommended to find the eigenvectors numerically even in this case. If we let $p_2^\circ = 0$ in addition, then the eigenvalues will be:

$$\boldsymbol{\lambda}^{\mathrm{T}} = [u_1 - c_1, u_1 + c_1, u_2 - c_2, u_2 + c_2], \tag{3.75}$$

[b] LAPACK is a Linear Algebra package available at http://www.netlib.no/

and the eigenvectors are now much simpler:

$$\boldsymbol{S} = \begin{bmatrix} -\alpha_2\alpha_1/c_1 & \alpha_2\alpha_1/c_1 & -\alpha_2\alpha_1/c_2 & \alpha_2\alpha_1/c_2 \\ -\alpha_1 p/c_1 & \alpha_1 p/c_1 & -\alpha_2 p/c_2 & \alpha_2 p/c_2 \\ 1 & 1 & 0 & 0 \\ 0 & 0 & 1 & 1 \end{bmatrix}, \tag{3.76}$$

$$\boldsymbol{S}^{-1} = 1/2 \begin{bmatrix} -c_1/\alpha_1 & -c_1/p & 1 & 0 \\ c_1/\alpha_1 & c_1/p & 1 & 0 \\ c_2/\alpha_2 & -c_2/p & 0 & 1 \\ -c_2/\alpha_2 & c_2/p & 0 & 1 \end{bmatrix}. \tag{3.77}$$

3.5.3 Multiphase partially-reflecting boundary conditions

When building partially reflecting boundary conditions for multiphase flow there are several possibilities.

Following the approach of Rudy and Strikwerda (1980)

One possibility is to follow the approach of Rudy and Strikwerda (1980), then boundary conditions can be constructed by setting $\mathscr{L}_i^- = 0$. To avoid drifting values a controller is inserted for each variable there is to specify.

As an example, consider the outflow boundary when both phases are subsonic, i.e. with two incoming characteristics, and we wish to specify the pressure and the volume fraction. Then add a controller for $\partial p/\partial t$ to the $\partial p/\partial t$-equation and add a controller for $\partial \alpha_1/\partial t$ to the $\partial \alpha_1/\partial t$-equation.

Following the approach of Poinsot and Lele (1992)

By using the controller to estimate the unknown $\mathscr{L}_i^-$ as Poinsot and Lele (1992) did, and use $\mathscr{L}_i^-$ in all the equations, a better coupling of the imposed information is probably achieved.

For instance, at an outlet where both phases are subsonic and α_1 and p is to be specified, set $\mathscr{L}_1^- = \mathrm{PID}(p)$ and $\mathscr{L}_2^- = \mathrm{PID}(\alpha_1)$.

The MPCBC method

A possible problem when using the approach of Poinsot and Lele (1992), is that it may lead to a situation where a variable which is at the specified level, is driven away from this level, since the other variables imposed by a controller are not[c].

This possible problem can be overcome by using Equation (3.20), but at the cost of solving an equation for $\mathscr{L}_i^-$. This is the chosen approach in this thesis, and it is here called Multiphase Characteristic Boundary Conditions (MPCBC).

The MPCBC method in the case of analytical eigenvectors

To clarify the MPCBC metod, it is shown for the case when the eigenvectors are available analytical, and with a PID-controller. The analytical eigenvectors from Equation (3.76),

$$\boldsymbol{S} = \begin{bmatrix} -s_a & s_a & -s_b & s_b \\ -s_c & s_c & -s_d & s_d \\ 1 & 1 & 0 & 0 \\ 0 & 0 & 1 & 1 \end{bmatrix} = \begin{bmatrix} -\alpha_2\alpha_1/c_1 & \alpha_2\alpha_1/c_1 & -\alpha_2\alpha_1/c_2 & \alpha_2\alpha_1/c_2 \\ -\alpha_1 p/c_1 & \alpha_1 p/c_1 & -\alpha_2 p/c_2 & \alpha_2 p/c_2 \\ 1 & 1 & 0 & 0 \\ 0 & 0 & 1 & 1 \end{bmatrix},$$

where $s_{a,b,c,d}$ is introduced to ease the notation. Assuming subsonic flow in both phases i.e. $|u_i| < c_i$ and the outlet ($u_i > 0$) is located at $x = x_{\max}$. Then $\mathscr{L}^- = \left[\mathscr{L}_1^-, \mathscr{L}_3^-\right]$ and $\mathscr{L}^+ = [\mathscr{L}_2^+, \mathscr{L}_4^+]$, further $\boldsymbol{S}$ is split into,

$$\boldsymbol{S}^+ = \begin{bmatrix} s_a & s_b \\ s_c & s_d \\ 1 & 0 \\ 0 & 1 \end{bmatrix}, \boldsymbol{S}^- = \begin{bmatrix} -s_a & -s_b \\ -s_c & -s_d \\ 1 & 0 \\ 0 & 1 \end{bmatrix}. \tag{3.78}$$

Recall that our goal is to find equations for the unknown $\mathscr{L}^-$ in Equation (3.15), and since the chosen approach is to control $\partial\alpha_1/\partial t$ and $\partial p/\partial t$ with PID-controllers, Equation (3.20), the following system for $\mathscr{L}^-$ appears,

$$\begin{bmatrix} -s_a & -s_b \\ -s_c & -s_d \end{bmatrix} \begin{bmatrix} \mathscr{L}_1^- \\ \mathscr{L}_3^- \end{bmatrix} = \begin{bmatrix} \mathrm{PID}(\alpha_1) \\ \mathrm{PID}(p) \end{bmatrix}, \tag{3.79}$$

[c]This behaviour has not been verified by numerical tests.

where,

$$\mathrm{PID}(\alpha_1) = \boldsymbol{S}_1^- \mathscr{L}^- = -(s_a \mathscr{L}_1^- + s_b \mathscr{L}_3^-) = \frac{1}{(1+K_D)} \cdot \left((\boldsymbol{S}_1^- \mathscr{L}^-)^\circ + K_P \Delta\alpha_1 + \frac{K_I}{T} \int_0^t \Delta\alpha_1 \, d\tau - K_D \, (\boldsymbol{S}_1^+ \mathscr{L}^+) \right) \quad (3.80)$$

and equivalent for $\mathrm{PID}(p)$.

3.6 Summary

In this chapter, characteristic-based boundary conditions have been reviewed. Further, they have been written on a form which is suitable for a system where the eigenvalues and eigenvectors must be found numerically.

The method used today to avoid a drifting pressure was recognised as the use of control functions to estimate the unknown $\mathscr{L}^-$. The use of the PID-controller was proposed.

With the present formulation, the NSCBC method has been reviewed for single-phase flow. Finally, for multiphase flow, the MPCBC method has been proposed.

Chapter 4

Numerical methods

The mathematical model presented in Chapter 2 together with the boundary conditions presented in Chapter 3 must be solved numerically. The numerical methods are presented in this chapter. As will be seen in Chapter 6, the model in some cases can be very near or even have complex eigenvalues. A solution found in such a case can have a strong impact from the numerical algorithm and not necessarily be the correct solution of the governing equations (Drew and Passman, 1999). Drew and Passman (1999, Chapter 20) write that the solutions should satisfy the following three prerequisites:

- the solutions must exist;
- the solutions must be uniquely determined; and
- the solutions must depend in a continuous fashion on the initial and boundary data.

In order to verify that the numerical solution found is indeed the solution of the modelled equations, the modelled equations with the proposed boundary treatment have been implemented in two different codes. The first is in this thesis called Runge-Kutta finite volume (RKFV), and is described in Section 4.2, the second is called Runge-Kutta finite difference (RKFD), and is described in Section 4.3.

4.1 Common for finite volume and finite difference

In both methods, the individual phases are considered compressible, i.e. an equation of state is used to link the pressure and the density variations. If explicit time integration is chosen as well, the system can be treated as

a coupled system of ordinary differential equations, one for each variable and every grid point after spatial discretisation.

4.1.1 Time integration

For the time integration, the five-stage, fourth order, explicit Runge-Kutta scheme of Carpenter and Kennedy (1994) is chosen, mainly because it is nearly as effective as the standard RK-schemes while only needing two storage registers for each equation.

We have the initial value problem

$$\frac{\partial U}{\partial t} = F(t, U(t)); \qquad U(t_0) = U_0. \tag{4.1}$$

The discrete approximation is made with a M-stage explicit RK scheme. Standard implementation over a time step h is accomplished by

$$k_1 = F(t_n, U^n) \tag{4.2}$$
$$k_i = F\left(t_n + c_i h, U^n + h\sum_{j=1}^{i-1} a_{i,j} k_j\right) \quad i = 2, \ldots, M \tag{4.3}$$
$$U^{n+1} = U^n + h\sum_{j=1}^{M} b_j k_j, \tag{4.4}$$

in the low-storage notation used by Carpenter and Kennedy (1994) this can be written as

$$dU_j = A_j dU_{j-1} + hF(U_j) \tag{4.5}$$
$$U_j = U_{j-1} + B_j dU_j, \qquad j = 1, \ldots, M \tag{4.6}$$

with $A_1 = 0$, so that it is self starting.

4.2 Finite volume

In this section, the general-purpose CFD code SPIDER originally developed by Melaaen (1990, 1992b,a) for calculating fluid flow in complex geometries, is extended to compressible multiphase flow.

4.2.1 Discretisation of the interior points

The material presented here is based on Melaaen (1990). The modelled transport equations can be cast into the prototype scalar convection-diffusion equation. For a particular scalar variable $\psi = U_i$ this equation reads

$$\frac{\partial}{\partial t}(\rho\psi) + \frac{\partial}{\partial x_j}\left(\rho\psi v_j\right) = \frac{\partial}{\partial x_j}\left(\Gamma\frac{\partial\psi}{\partial x_j}\right) + \rho S, \tag{4.7}$$

where Γ is the diffusivity and S is the source term.

Since the finite-volume concept is chosen, the equation is integrated over a general control volume, δV, in physical space. Then the Gauss divergence theorem is used. Based on earlier experience, a non-staggered (collocated) grid arrangement is preferred Melaaen (1992b,a). The equation is transformed from Cartesian coordinates, x_i, to curvilinear non-orthogonal coordinates, ξ_i, by using the chain rule

$$\frac{\partial\psi}{\partial x_i} = \frac{\partial\xi_j}{\partial x_i}\frac{\partial\psi}{\partial\xi_j} \tag{4.8}$$

In order to compute this expression, the relation

$$\frac{\partial\xi_j}{\partial x_i} = \frac{A_i^j}{J}, \tag{4.9}$$

where A_i^j are the Cartesian area projections and J is the Jacobian determinant of the coordinate transformation, is used. A_i^j and J are linked to the covariant basis vectors $\boldsymbol{e}_{(i)}$ by

$$J = \boldsymbol{e}_{(1)} \cdot \left(\boldsymbol{e}_{(2)} \times \boldsymbol{e}_{(3)}\right), \tag{4.10}$$

and

$$A_n^j \boldsymbol{i}^n = \boldsymbol{e}_{(l)} \times \boldsymbol{e}_{(m)}, \tag{4.11}$$

where j, l and m are cyclic.

The final algebraic equations are stored in the right hand side of Equation (4.1).

$$F = \sum_{\text{nb}} a_{\text{nb}}\psi_{\text{nb}} - a_P\psi_P + b, \tag{4.12}$$

where

$$a_P = \sum_{\text{nb}} a_{\text{nb}} + a_{\text{f}} - \overline{S}_{2P}, \tag{4.13}$$

$$b = b_{\text{NO}} + \overline{S}_{1P}, \tag{4.14}$$

$$a_{\text{f}} = F_e - F_w + F_n - F_s + F_t - F_b, \tag{4.15}$$

and

$$\begin{aligned} b_{\text{NO}} &= \left[\Gamma G^{12}\frac{\partial\psi}{\partial\xi^2} + \Gamma G^{13}\frac{\partial\psi}{\partial\xi^3}\right]_w^e + \left[\Gamma G^{21}\frac{\partial\psi}{\partial\xi^1} + \Gamma G^{23}\frac{\partial\psi}{\partial\xi^3}\right]_s^n \\ &+ \left[\Gamma G^{31}\frac{\partial\psi}{\partial\xi^1} + \Gamma G^{32}\frac{\partial\psi}{\partial\xi^2}\right]_b^t. \end{aligned} \tag{4.16}$$

In these equations, subscript nb refer to the neighbouring nodes surrounding the central node P. The subscripts e, w, n, s, t, and b refer to the control volume faces, east, west, north, south, top and bottom. Superscript $^\circ$ means values from previous time-step.

The terms F_{nn} in Equation (4.15) represent the mass-flow across the various control volume faces

$$F_{nn,k} = (\alpha_k \rho_k u_{k,j} A_j^m)_{nn}. \tag{4.17}$$

Subscript nn is a general indicator. Index m refers to the direction of the area vector. If nn is equal to e or w, then $m = 1$. Analogously, nn equal to n or s gives $m = 2$ and nn equal to t or b gives $m = 3$.

The geometric diffusion coefficient in Equation (4.16) is defined as

$$G^{ji} = \frac{A_l^j A_l^i}{J}, \tag{4.18}$$

and the source term S has been linearised according to the equation

$$\overline{S}_P = \int_{\delta V} S dV = \overline{S}_{1P} + \overline{S}_{2P}\,\psi_P, \tag{4.19}$$

where $\overline{S}_{1P}$ gives the constant part of the source and $\overline{S}_{2P}$ is the coefficient of the variable part.

The a_{nb} coefficients and the mass-flow terms in Equation (4.15) contain fluxes with both a diffusive and a convective part. In this work, for the convective term two different discretisation schemes have been used:

Power law: The power-law scheme is a curve fit to the exact solution for the one-dimensional, steady-state, diffusion-convection flow with zero source and constant diffusivity (Patankar, 1980). At low Peclet numbers, the power-law scheme is reduced to central differencing, and at high Peclet numbers to the first-order upwind scheme. Hence, the power-law scheme is second-order accurate at low Peclet numbers and first-order accurate at high Peclet numbers. The power law scheme is very robust, but at high Peclet numbers, false diffusion reduces the quality of the result.

Second order upwind: Since the power-law scheme can produce inaccurate solutions at high Peclet numbers, a better approach for discretising the convective terms is needed. In the second-order upwind method, linear extrapolation from the two upstream neighbouring nodes is used when estimating the cell face value. From Taylor series analysis, the second-order upwind scheme is second-order accurate. As with all higher-order discretisation schemes, the second-order upwind scheme can produce over- and undershoots in regions with steep gradients (Peric, 1985).

4.2.2 Grid

SPIDER uses curvilinear non-orthogonal coordinates which enable a detailed description of many complex two- and three-dimensional geometries. In this thesis the boundary conditions are studied. Therefore, errors due to the gridding should be minimised, hence Cartesian orthogonal equidistant grids are chosen. Then errors due to grid stretching and non-orthogonality are absent (Melaaen, 1990, Chapter 4).

4.2.3 Explicit solution scheme

In the RKFV method the composite equations are solved.

At time t, the dependent variables p_k, ρ_k, α_k, $u_{k,j}$, are known at each grid point. The mass and momentum equations are then advanced one (sub)time step using the Runge-Kutta scheme. This provides values for $(\alpha\rho)_k$, $(\alpha\rho u_j)_k$ for each grid point at time $t + \Delta t$.

Computing the state

Having computed $(\alpha\rho)_k$, $(\alpha\rho u_j)_k$ we need to separate the individual variables. $u_{k,j}$ is easily found by dividing by $(\alpha\rho)_k$. In order to determine the 3ϕ variables p_k, ρ_k, and α_k, where ϕ is the number of phases, ϕ equations of state are required. In general, the equations of state can be coupled, non-linear, and implicit. The equation of state for phase k is expressed as $\mathcal{F}_k(\alpha_t, \rho_t) = 0$, where $t = 1, \ldots, \phi$. The 3ϕ unknowns α_k, ρ_k, and p_k are found by solving the following set of 3ϕ non-linear algebraic equations:

$$\begin{aligned} \alpha_k\rho_k - (\alpha\rho)_k &= 0,\ k = 1, \ldots, \phi \\ \mathcal{F}_k(\alpha_t, \rho_t, p_t) &= 0,\ k = 1, \ldots, \phi \\ p_1 - p_k &= 0,\ k = 2, \ldots, \phi \\ \sum_{k=1}^{\phi} \alpha_k - 1 &= 0. \end{aligned} \tag{4.20}$$

Analytical solution

Under certain simplifying assumptions, it is possible to solve the non-linear set of 3ϕ equations in Equation (4.20) analytically. With the equation of state from Chapter 2,

$$p_k = (\rho_k - \rho_k^\circ)c_k^2, \tag{4.21}$$

where c_k is the speed of sound for phase k. Inserted into Equation (4.20), the system of equations reads

$$\begin{aligned} \alpha_k\rho_k - (\alpha\rho)_k &= 0,\ k = 1, \ldots, \phi \\ p_k - c_k^2(\rho_k - \rho_k^\circ) &= 0,\ k = 1, \ldots, \phi \\ p_1 - p_k &= 0,\ k = 2, \ldots, \phi \\ \sum_{k=1}^{\phi} \alpha_k - 1 &= 0. \end{aligned} \tag{4.22}$$

In the special case when only two phases are involved ($\phi = 2$), a quadratic

equation for p appears. The solution of this equation is

$$\begin{aligned} p &= \frac{1}{2}\left(-c_1^2\rho_1^\circ - c_2^2\rho_2^\circ + c_1^2(\alpha\rho)_1 + c_2^2(\alpha\rho)_2\right) \\ &+ \frac{1}{2}\Big((c_1^2\rho_1^\circ)^2 - 2c_1^2c_2^2\rho_1^\circ\rho_2^\circ - 2(c_1^2)^2\rho_1^\circ(\alpha\rho)_1 \\ &+ 2c_2^2\rho_1^\circ c_1^2(\alpha\rho)_2 + (c_2^2)^2(\rho_2^\circ)^2 + 2c_1^2c_2^2\rho_2^\circ(\alpha\rho)_1 - 2(c_2^2)^2\rho_2^\circ(\alpha\rho)_2 \\ &+ (c_1^2)^2(\alpha\rho)_1^2 + 2c_1^2c_2^2(\alpha\rho)_1(\alpha\rho)_2 + (c_2^2)^2(\alpha\rho)_2^2\Big)^{0.5} \end{aligned} \tag{4.23}$$

In the time-marching scheme, p can be found from $(\alpha\rho)_1$ and $(\alpha\rho)_2$ after each time (sub)step. It is now straightforward to find the phase densities ρ_k from Equation (4.21). Finally, the phase volume fractions α_k are found by dividing $\alpha_k\rho_k$ with the newly found ρ_k.

Numerical solution

For a three-phase system ($\phi = 3$), a cubic equation for p arises. Although the roots can be found analytically, it is more practical to solve the equations numerically, for instance with the Netlib package DNSQ.

4.2.4 Filtering

For incompressible flow spurious oscillation in the solution can be prevented by using momentum interpolation (Rhie and Chow, 1983).

In compressible flow the Rhie and Chow interpolation does not filter sufficiently, therefore Munkejord *et al.* (2003) extended this method to filter all variables. They used a hyper-viscosity filter, which in short adds a filter function to the right-hand side to each integrated equation:

$$F(\psi) = A_f \frac{(\Delta x)^4}{\tau}\frac{\partial^4\psi}{\partial x^4}, \tag{4.24}$$

where τ is the time-step length and A_f a coefficient. The filter is only applied to inner points. However, numerical tests indicate that the boundary points should be included in the discretisation of the filter or else it may be unstable. Filtering must be applied with care since it adds a term to the equations. The filter coefficient A should therefore be as small as possible, but still large enough so that a solution is found.

4.2.5 Discretisation of the boundary formulation

At the boundary the finite-volume approach is not appealing, since the volume is zero. Instead the right-hand side for the Runge-Kutta integrator is computed using the boundary formulation directly. In SPIDER, the composite form (3.13) is used. To find $\mathscr{L}_i^+$, the derivative of the primitive variables are obtained by finite-difference schemes of second order:

$$\frac{\partial f}{\partial x} = \frac{\partial f}{\partial \xi}\frac{\partial \xi}{\partial x} + \frac{\partial f}{\partial \eta}\frac{\partial \eta}{\partial x}, \tag{4.25}$$

where the scheme for $\partial f / \partial \xi$ is

$$\begin{aligned} f_1' &= 3\,(f_2 - f_1) + \frac{1}{3}\,(f_1 - f_3)\,, \\ f_2' &= (f_2 - f_1) + \frac{1}{3}\,(f_3 - f_1)\,, \\ f_3' &= \frac{1}{2}\,(f_4 - f_2)\,, \end{aligned}$$

where the third point corresponds to the interior scheme. SPIDER utilises a special equidistant numerical grid, where $\Delta\xi = 1$ everywhere except between the boundary point and the first interior point where $\Delta\xi = 1/2$.

4.3 Finite differences

Gran (2000) developed a Navier-Stokes solver based on finite differences. This code utilises a clean numerical approach with high-order numerical schemes and high-order numerical filters. It is limited to equidistant grids and does not automatically conserve mass[a], however this code can serve as a validation if these limitations are overcome.

4.3.1 Spatial discretisation

The primitive formulation, Equation (3.2),

$$\frac{\partial \boldsymbol{U}}{\partial t} + \boldsymbol{A}\frac{\partial \boldsymbol{U}}{\partial x_1} + \boldsymbol{C} = \boldsymbol{0},$$

[a] Special care must be taken in order to achieve a conservative scheme, this is not done here.

is discretised in all points by replacing $\partial/\partial x$ by finite difference operators. Here, the eighth-order explicit stencil with a (3,3,4,6-8-6,4,3,3) boundary treatment is shown:

$$
\begin{aligned}
f_1' &= \frac{1}{6\Delta x}\left(-11f_1 + 18f_2 - 9f_3 + 2f_4\right), \\
f_2' &= \frac{1}{6\Delta x}\left(-2f_1 - 3f_2 + 6f_3 - f_4\right), \\
f_3' &= \frac{1}{12\Delta x}\left[8\left(f_4 - f_2\right) - \left(f_5 - f_1\right)\right], \\
f_4' &= \frac{1}{60\Delta x}\left[45\left(f_5 - f_3\right) - 9\left(f_6 - f_2\right) + \left(f_7 - f_1\right)\right], \\
f_5' &= \frac{1}{840\Delta x}\left[672\left(f_6 - f_4\right) - 168\left(f_7 - f_3\right) + 32\left(f_8 - f_2\right) - 3\left(f_9 - f_1\right)\right],
\end{aligned}
$$

where the fifth grid point above corresponds to the interior scheme.

4.3.2 Filtering

After each time step, the solution vector $\boldsymbol{U}$ is filtered by a filter function,

$$\tilde{\boldsymbol{U}} = \left(1 + \zeta_D \boldsymbol{D}_\mathrm{f}\right)\boldsymbol{U}, \tag{4.26}$$

where the filter coefficient ζ_D is given by $(-1)^{n+1}2^{-2n}$ for a $(2n)$th-order filter, and $\boldsymbol{D}_\mathrm{f}$ is the dissipation matrix. Normally, a filter with the same or higher order than the spatial operator is used. Here, the dissipation matrix for the second-order filter with first-order boundary points appear as

$$\boldsymbol{D}_\mathrm{f} = \begin{bmatrix} +1 & -1 & 0 & 0 & 0 \\ -1 & +2 & -1 & 0 & 0 \\ 0 & -1 & +2 & -1 & 0 \\ 0 & 0 & -1 & +2 & -1 \\ 0 & 0 & 0 & -1 & +1 \end{bmatrix}. \tag{4.27}$$

Filtering and boundary conditions

Special care must be taken when $\partial U_i/\partial t$ is given on the boundary or estimated by a P-controller. The easiest solution is to not filter the boundary point for U_i. When a PID-controller is used at the boundary, there is no need

for special care since the controller makes sure that the solution slowly converges to the specified value.

A more thorough discussion of explicit filters and high-order finite difference operators can be found in Kennedy and Carpenter (1994, 1997).

4.4 Summary

In this chapter, the numerical methods have been explained. A Runge-Kutta scheme was chosen for the time-integration. Both finite-volume and finite-differences are chosen for the spatial discretisation. In the finite-volume code, which is here called RKFV, the general-multi purpose CFD code SPIDER has been altered to solve the multiphase equations. In the finite-difference code, which is here called RKFD, central differences of various order is used to solve the governing equations.

Chapter 5

Case study I: Single-phase poiseuille flow

The development of boundary conditions is an area of ongoing research, where most of the work has been done for single-phase flow. In Chapter 3, the matrix notation was introduced. Furthermore, it was realized that the method used by other authors to avoid a drifting pressure simply is to apply controllers for the unknown $\mathscr{L}_i$. Therefore, in order to check the implementation and to compare the different controlling methods, the plane channel of Poinsot and Lele (1992) is chosen. In Section 5.1, this enables us to validate our results against theirs. A new test to evaluate the boundary conditions, which until now has been cumbersome to perform, is developed in Section 5.2.

5.1 Validation of the method

This section concerns a numerical study of a 2D channel. The channel is the same as the one Poinsot and Lele (1992) used.

5.1.1 Problem description

A viscous fluid, with kinematic viscosity $\nu = 2\,\mathrm{m}^2/\mathrm{s}$ and speed of sound $c = 300\,\mathrm{m/s}$, flowing in a 2D plane channel, with length $L = 10\,\mathrm{m}$ and half-height $h = 1\,\mathrm{m}$, is studied here.

The inflow conditions are:

$$\begin{aligned} u(0,y,t) &= u_0 \left[\cos\left(\frac{\pi}{2}\frac{y}{h}\right)\right]^2, \\ v(0,y,t) &= 0, \end{aligned} \tag{5.1}$$

where $u_0 = 30\,\mathrm{m/s}$ is the maximum inlet velocity. The Reynolds number is $Re = u_0 h/\nu = 15$ and the Mach number is $\mathscr{M} = u_0/c = 0.1$.

Analytical solution

An analytical solution may be found if this case is considered to be incompressible. A criterion for this is:

$$\frac{L}{h}\frac{\mathscr{M}^2}{Re} \ll 1. \tag{5.2}$$

For this computation, $L/h\,Re^{-1}\mathscr{M}^2 = 0.007$ and the incompressible solution may be considered to be close to the exact one. The exact solution is:

$$\frac{\partial p}{\partial x}^{\mathrm{e}} = -\frac{3}{2} Re^{-1} \rho u_0^2, \tag{5.3}$$

where

$$u(x,y,t) = u_{\mathrm{m}}(1 - (y/h)^2), \tag{5.4}$$

and u_{m} is the maximum velocity: $u_{\mathrm{m}} = -\frac{1}{2\mu}\frac{\partial p}{\partial x}^{\mathrm{e}} h^2$.

Initial values

Initial values for the calculations are:

$$\begin{aligned} u(x,y,0) &= u_0 \left[\cos\left(\frac{\pi}{2}\frac{y}{h}\right)\right]^2, \\ v(x,y,0) &= 0, \\ \rho(x,y,0) &= \rho_{\mathrm{in}} = 1\,\mathrm{kg/m^3}. \end{aligned} \tag{5.5}$$

Lateral boundary conditions

The lateral boundary conditions (y=$\pm h$) correspond to no-slip walls. For the walls, the unknown $\mathscr{L}_i$ could be found by specifying the velocity, however this is computationally expensive, and hence should be avoided whenever possible. In this case, the pressure is found by weighted linear extrapolation in the physical space (Melaaen, 1990, Chapter 2).

Inlet

At the inlet, the velocity is specified and the unknown $\mathscr{L}_i$ are found from the LODI relations, (Section 3.3).

Outlet

At the outlet, the pressure is specified with a controller for $\partial p/\partial t$. For simplicity, the discussion is restricted to P- ($K_I = K_D = 0$) and PI-controllers ($K_D = 0$ in Equation (3.44)):

$$\mathscr{L}_1 = \mathscr{L}_1^\circ + K_P \Delta p + \frac{K_I}{T} \int_0^t \Delta p \, d\tau, \tag{5.6}$$

$$\mathscr{L}_1^\circ = (u - c)\left(\frac{\partial p}{\partial x}^{\mathrm{e}} - \rho c \frac{\partial u}{\partial x}^{\mathrm{e}}\right), \tag{5.7}$$

where $\partial u/\partial x^{\mathrm{e}}$ is found from continuity of the exact solution. For the proportional term we take $K_P = \sigma(1 - \mathscr{M}^2)c/L$ and for the integral term $K_I = K_P$.

5.1.2 About the computations

The Navier-Stokes equations given in Section 3.4 are solved with the RKFV and RKFD approach from Chapter 4.

RKFV

The computational domain is discretised with a 41×41 equidistant grid. For the convective discretisation in the inner domain, the SOU-scheme is

used. Initial tests showed that the computations were stable without a filter, thence no filtering is applied. In the boundary discretisation, a second-order first-derivative operator was used, and for the viscous terms the first-derivative operator is used twice.

RKFD

For the finite-difference code, the Navier-Stokes equations were discretised in the same manner at the boundary as in the inner domain. The domain is discretised with an equidistant 41×41 grid and the spatial discretisations are obtained with an eight-order first-derivative operator. For the viscous terms, the first-derivative operator is applied twice. The solution is filtered after each time step with an eight-order explicit filter.

5.1.3 The steady solution

The steady solution can be found by applying either a P- or a PI -controller for $\partial p/\partial t$ at the outlet. The steady solution does not depend much on the choice of the controlling parameters, save the absolute pressure level, thence the steady solution is studied for one of the P-controllers.

At the outlet, it is desired to be able to compute the case as if the channel were infinitely long, or in other words no acceleration process is present near the outlet boundary. This is observed in the pressure contour plot, Figure 5.2, since the pressure lines are vertical (gravity is neglected) so the pressure in the developed section is a function of x only. This can also be seen in the velocity contour plot, Figure 5.1, where the velocity lines at the outlet are horizontal. This agrees with Poinsot and Lele (1992).

The transverse velocity profile in Figure 5.3, is plotted at the inlet, $x = L/3$, $x = 2L/3$ and at $x = L$. The exact velocity profile, Equation (5.4), is shown as well. The difference between the profiles cannot be observed in this plot, save the inlet profile, since they are almost equal to the exact velocity profile. This is also in accordance with the solution found by Poinsot and Lele (1992).

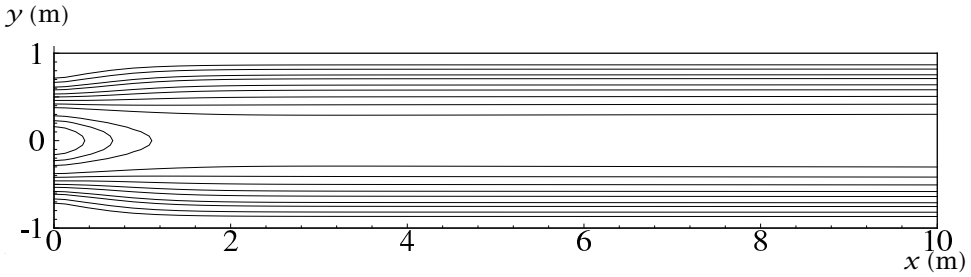

Figure 5.1: Contour plot of the velocity.

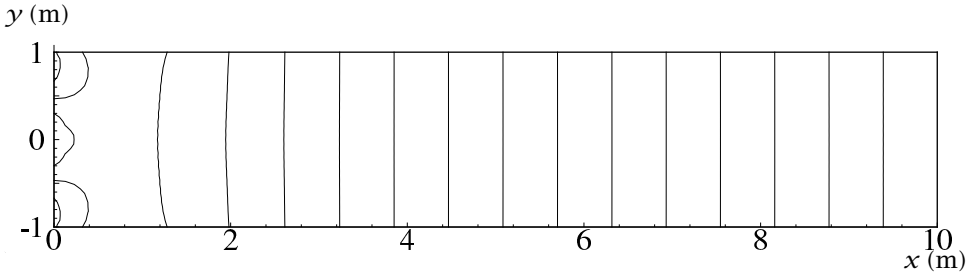

Figure 5.2: Contour plot of the pressure.

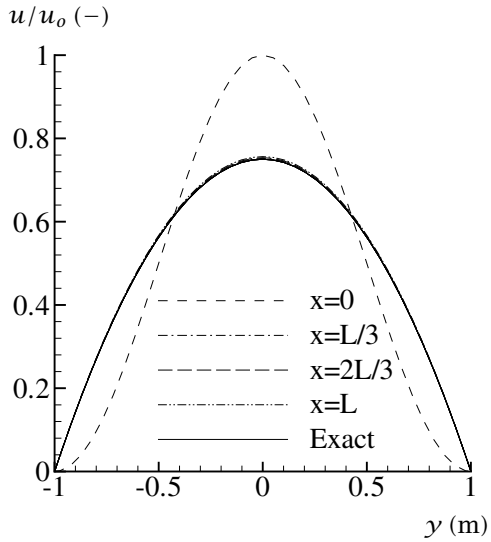

Figure 5.3: The transverse velocity profile, for x=0, $L/3$, $2L/3$, L and the exact solution.

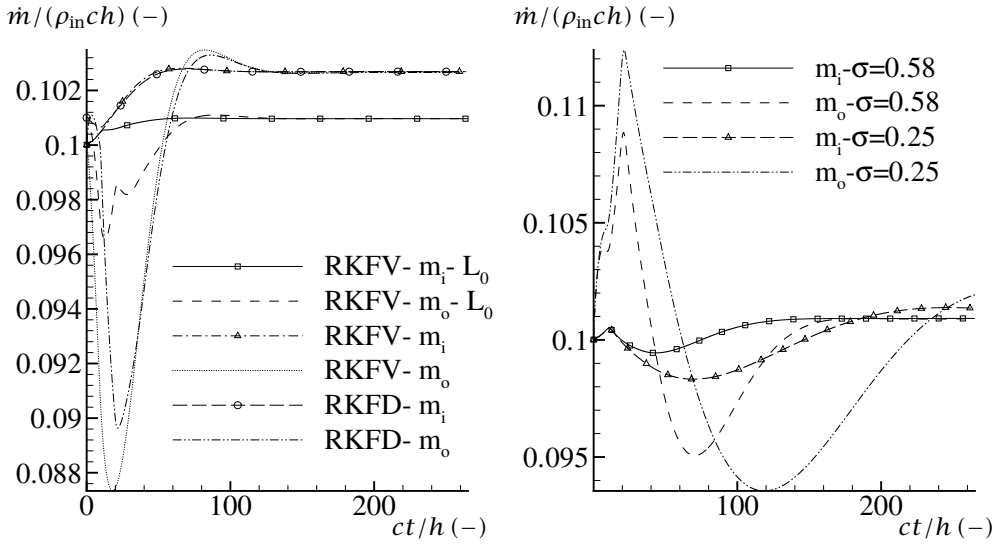

(a) P-controllers at the outlet

(b) PI-controllers at the outlet

Figure 5.4: Inlet and outlet mass-flow rates.

5.1.4 The transient solution

More insight into the performance of the boundary conditions can be gained by studying the transient behaviour of the solution. In Figure 5.4, the reduced inlet and outlet mass-flow rates are presented versus reduced time $t' = ct/h$. In this figure, the label RKFV-m_i-L_0 denominates Runge-Kutta Finite Volume, reduced inlet flow rate, with $\mathscr{L}^\circ$ from Equation (5.7). m_o tells us that it is the outlet flow rate and when L_0 is not present in the label, then $\mathscr{L}^\circ$ is zero. Figure 5.4(a) presents different P-controllers ($K_I = 0$, $\sigma = 0.58$), while Figure 5.4(b) shows two different PI-controllers[a].

Comparison of RKFD and RKFV

By comparing the results obtained with RKFD and RKFV in Figure 5.4(a), it can be observed that there is little difference between the finite-difference and the finite-volume results. Therefore, it is reasonable to assume that the numerical solution found is the correct solution of the modelled equations.

A detail which is not observed in Figure 5.4(a) is that the inlet flow-rate was not exactly equal to the outlet flow rate for the RKFD case. This is due to the straightforward finite-difference implementation used here not conserving mass.

The effect of $\mathscr{L}^\circ$

The outlet pressure does not reach the specified reference pressure ($p_\infty = 0.9$ bar for these simulations) when using the P-controllers. In Figure 5.4(a) it is observed that two different values of $\mathscr{L}^\circ$ gives different dynamical behaviour as well as convergence to different mass-flow rates. Different mass-flow rates tells us that the absolute pressure is different, so the level of $\mathscr{L}^\circ$ affects the converged pressure at the outlet for the P-controllers. This behaviour makes sense if the converged value of $\mathscr{L}_1 = \mathscr{L}_1^c$ is constant. Recall from Equation (5.6) that then the converged value of $\mathscr{L}_1$ must be,

$$\mathscr{L}_1^c = \mathscr{L}^\circ + K_p \Delta p,$$

or,

$$p_{x=L} = p_\infty + \left(\mathscr{L}_1^c - \mathscr{L}^\circ\right)/K_p.$$

[a]Note that the axes are different for Figure 5.4(a) and Figure 5.4(b).

From this it is clear that the pressure can only be specified to a given value if $\mathscr{L}_1^c$ is known a priori.

This is not the case for the PI-controllers, since the integral term assures that the pressure at the outlet will be equal to the specified pressure. However, different $\mathscr{L}^\circ$ affect convergence rates and the behaviour of the PI-controllers.

The effect of different σ

σ is an important controlling parameter. When very low values of σ were used, the pressure began to drift, and when very high σ were employed, the solution became unstable. This behaviour is also observed by Poinsot and Lele (1992). For the PI-controllers, simulations with two different values of σ are presented in Figure 5.4(b). From the figure one can see that the convergence is better and the amplitude of the mass-flow rate variations is smaller for $\sigma = 0.58$ than for $\sigma = 0.25$.

A more methodical way of determining the optimal controlling parameters should be developed. However, it is beyond the scope of the present work.

5.1.5 Summary

Single-phase poiseuille flow has been computed and we have verified that the solution corresponds to a case computed by Poinsot and Lele (1992) and we experienced the same behaviour as they did.

5.2 Evaluation of the boundary conditions

In order to find out how good the boundary conditions are, they should be tested where something can be stated about their performance. Therefore a new test for the boundary conditions is presented.

In Figure 5.5 three Channels A, B and C are shown, for clarity the figure is not drawn dimensionally correct. The channels are computed with the same properties as the channel earlier in this chapter. The length of Channel C in Figure 5.5 is twice that of Channel A and Channel B. With this configuration, the obtained solution in Channel A can be compared with the solution in

the first part of Channel C, and logically the solution obtained in Channel B can be compared with the solution in the second part of Channel C.

This test can be done since the PI-controllers have the ability to specify the pressure to any degree of accuracy. Note that to perform this test with a P-controller would be cumbersome, since it would require an iteration procedure to specify the pressure to a high degree of accuracy. It may be due to that reason that this test, as far as the author know, has not been published before.

This approach will give an idea of the performance of the boundary conditions, furthermore it is even possible to extract approximate values of $\mathscr{L}_i$ at $x = L$ from Channel C and compare them with the values for Channel A and B. Here, however, the discussion is restricted to comparing the converged solution for the three cases.

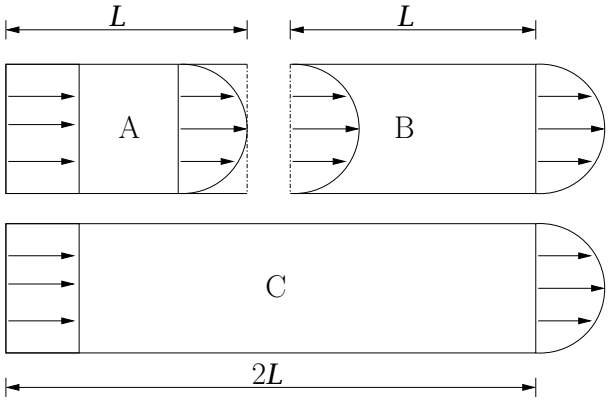

Figure 5.5: Test case for evaluating the boundary conditions.

5.2.1 Boundary conditions for computing the channels

Boundary conditions for Channel C

The same channel as earlier in this chapter is calculated, but now with length $2L$. The boundary conditions are the same as before, specifying the outlet pressure p_∞ with a PI-controller and setting the inlet velocity.

Boundary conditions for Channel A

To compute the first part of the channel, the same boundary conditions as for Channel C were used, except that the pressure $p_L = p_{x=L}$ obtained at $x = L$ from Channel C was specified instead of p_∞.

Boundary conditions for Channel B

A natural choice would be to specify boundary conditions for Channel B as for Channel A and Channel C. That is by reading the velocity profile at $x = L$ in Channel C, and specify this at the inlet. However, this way of specifying boundary conditions is already tested for Channel A. Since the flow in Channel B is fully developed, boundary conditions for fully developed flow can be tested instead.

For the second part of the channel, a PI-controller was applied for the pressure at both the inlet and outlet, i.e. specifying p_L at the inlet and p_∞ at the outlet. According to theory, one more boundary condition must be specified at the inlet, so a P-controller for the v-velocity was used. Indeed, a PI-controller may be used as well, however, initial tests showed that a PI-controller for the v-velocity was unstable unless the whole domain was filtered. In the RKFV code, such a filter was not available and hence a P-controller for the v-equation was chosen.

5.2.2 Results

This problem was computed with the RKFD and RKFV approach and both gave excellent results. In order to compare and quantify the error, the relative difference between the simulations has been calculated. The relative error is defined by:

$$e(f) = \left| \frac{f_{2L} - f_L}{f_{2L}} \right|, \tag{5.8}$$

where f_{2L} is evaluated in Channel C. f_L is evaluated in Channel A when $0 \le x \le L$ and in Channel B when $L \le x \le 2L$. The error is computed in all points, except where f_{2L} is zero. To simplify the comparisons, it makes sense to use the maximum of $e(f)$ as a measure of quality.

RKFD

Filtering must be applied with care when specifying a given variable like the velocity at the inlet. The filter function must not alter this variable at this boundary. When applying PI-controllers for the variable to specify at the boundary, all variables may be filtered at this boundary, since the controller adjusts the variable to the specified value smoothly with time.

In Table 5.1, Channel A and C are compared for three computations with 20×20 control volumes. The first column tells which variable is compared, and the second column at which point the comparison is done. For instance, (mx,2) is at the maximum in x-direction and point 2 in the y-direction. In the next column, the label 2x-8f means that the spatial derivative operator is second-order, and the filter is eight-order.

The first to be read from the table is that the error goes significantly down when filtering is applied, and slightly down when the order of the spatial operator is increased. Second, when the error in the u-velocity is as low as $1 \cdot 10^{-5}$ it is for most practical purposes zero. It is then reasonable to conclude that a filter should be applied when available. This is confirmed when the grid resolution is increased, since the computations are unstable when filtering is not applied.

When comparing Channel B and C, similar results as when comparing Channel A and C are obtained.

Table 5.1: Comparison of Channel A and C for the RKFD computations

$e(f)$	(i,j)	2x-NO	2x-8f	8x-8f
u	(mx,2)	0.0031	$9.6 \cdot 10^{-5}$	$6.45 \cdot 10^{-5}$
u	(2,2)	0.0013	$1.8 \cdot 10^{-5}$	$1 \cdot 10^{-5}$
p	any	$12 \cdot 10^{-7}$	$4.3 \cdot 10^{-7}$	$9 \cdot 10^{-8}$

RKFV

Filtering was not applied since the computations were stable for the actual grid resolution and the present filter is not effective close to the boundary. In fact, the error increased with filtering, however, in general a proper filtering procedure is required, since the computations were unstable for grid resolutions higher than 80×80 control volumes.

Table 5.2: Comparison Channel A and C for the RKFV computations

$e(f)$	(i,j)	20	40	80
u	(mx,2)	0.0078	0.0061	0.0041
u	(2,2)	0.0023	0.0015	$1.66 \cdot 10^{-5}$
p	any	$247 \cdot 10^{-7}$	$66.3 \cdot 10^{-7}$	$2.55 \cdot 10^{-7}$

In Table 5.2, Channel A and C are compared at different grid resolutions. As seen in the table, the error in the pressure goes down with at least second-order convergence, however the error in the u-velocity goes only slightly down.

The largest error in the u-velocity was 0.007 at $x = L$. In Figure 5.6, this error is visualised by plotting the u-velocity, in the point closest to the wall, for Channel A, B and C. A peculiar observation in this plot is that the u-velocity seems to be symmetric around $x = L$ for Channel A and B, this is probably only by chance, since this is not the case in the middle of the channel.

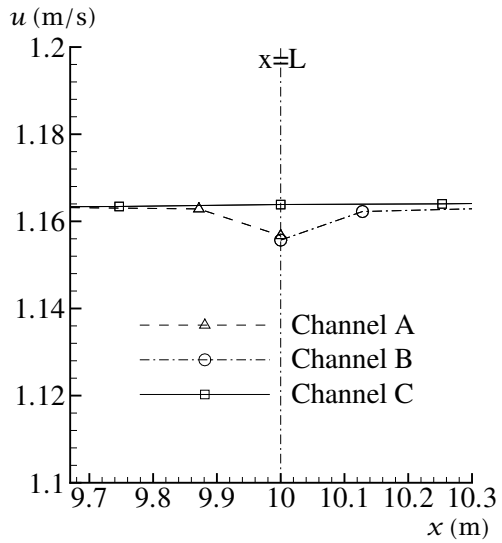

Figure 5.6: The u-velocity at $x = L$ in the point closest to the wall.

The error in the u-velocity is probably due to the lack of filtering, since the RKFD code with no filtering and second-order discretisation gives error

at the same position of equal order, as can be seen from Table 5.1.

5.3 Summary

In this chapter, the boundary formulations were applied to single-phase Poiseuille flow. The computations agreed with those of Poinsot and Lele (1992), and the boundary conditions showed excellent performance.

Different controllers have been tested, and since the PI-controllers allowed us to specify the outlet pressure exactly, a new test could be performed. Due to this ability, it is fair to conclude that the PI-controllers are better than the P-controllers. On the other hand, the PI-controllers are more complex to tune for optimal use.

It has also been demonstrated that by specifying the pressure at the inlet as well as the outlet with a PI-controller, can be used as a method for simulating fully developed flow. Care had to be taken when applying the PI-controller to the inlet v-velocity.

A direct specification of the inlet u-velocity has been tested and it showed excellent results. An alternative, which may be attractive when it is important to filter the whole domain, could be to use a PI-controller to specify the inlet velocity as well. This is not necessarily a preferred method, since the more variables which are specified with a controller, the more difficult it will be to find optimal controlling parameters for the given case.

Chapter 6

Case study II: Two-phase flow

The purpose of this chapter is to find solutions of the *modelled* multiphase equations, which are summarised in Appendix B, to study mathematical aspects of the model, and to study the behaviour of the boundary conditions. Recall the assumptions made in Chapter 2 when developing the model. Although the modelled equations are simplified, they possess many mathematically challenging properties needing to be understood.

In Section 6.1, the eigenvalues and eigenvectors are computed and discussed for some example configurations. A one-dimensional shock-tube with perfectly non-reflecting boundary conditions on both sides is computed in Section 6.2.1. Inlet and outlet boundary conditions are studied for a one-dimensional tube in Section 6.2.2. In Section 6.3, unphysical behaviour of the model is investigated. Finally, two-phase flow in a two-dimensional channel with walls, inlet, and outlet is studied in Section 6.4.

Table 6.1: Three configurations and corresponding eigenvalues.

Property	Unit	Case 1	Case 2	Air-Water
B_k	–	0.99992	0.99992	0.99992
$B_{k-\lim}$	–	0.9999872	0.9999980	0.99999982
p	bar	9.00	9.00	10.00
ρ_1	kg/m^3	104.20	101.84	8.65
ρ_2	kg/m^3	672.90	672.99	1000.51
c_1	m/s	127.92	127.92	340
c_2	m/s	451.48	451.48	1400
α_1	–	0.89	0.79	0.79
u_1	m/s	12.00	0.69	0.69
u_2	m/s	11.50	0.99	0.99
λ_1	m/s	−117.08	−129.53	−339.67
λ_2	m/s	11.17	0.62	0.67
λ_3	m/s	11.84	1.33	1.31
λ_4	m/s	141.07	130.92	341.05

6.1 Example configurations

Since the eigenvalues and eigenvectors are not available in an explicit form, it makes sense to study them numerically, and thereby gaining some insight into the mathematical model.

The eigenvalues of $\boldsymbol{A}$, Equation (3.73) from Section 3.5.2, have been computed numerically for three example configurations, and the results are listed in Table 6.1. Case 1 and Case 2 are examples of real-life multiphase flows in pipes. Multiphase flow of air and water is considered to be an extreme case in the sense that the densities are different by three orders of magnitude. Water and air are also well known fluids, and they will be used as example fluids throughout this chapter.

Speed of sound

From single-phase flow, we are used to express the eigenvalues in terms of the speed of sound, i.e. on the form $\lambda = u \pm c$. Here "New speeds of sound" for Case 2 can be found by setting $u_1 = u_2 = 0$, and then the eigenvalues become $\pm\mu_1 = 130\,\mathrm{m/s}$ and $\pm\mu_2 = 0.36\,\mathrm{m/s}$. As an approximation, this gives us the eigenvalues $\lambda = u_k \pm \mu_k, (k = 1, 2)$. These speeds must not be confused with the mixture speed of sound, see for instance Taitel (2003).

Observe in Table 6.1 that all eigenvalues, except λ_4, are lower than the speed of sound for the individual phases. This indicates that the signal-speeds are reduced significantly for all three cases compared to single-phase flow.

Low speed of sound

The fact that the speed of sound is low in two-phase systems is explained in Nguyen *et al.* (1981). A simple illustration appears if it is assumed that the speed of sound is also the critical velocity for choked two-component flow. This low speed explains why champagne spurting from the top of a newly opened bottle is flowing at the speed of sound of the mixture (so-called "choked flow"), but not at the speed of sound of the liquid (Drew and Passman, 1999, Page 279).

Hybrid-sonic flow

In single-phase flow, when one continuity and one momentum equation are considered, the flow is called supersonic if both eigenvalues are positive (or negative), and subsonic when one of the eigenvalues is negative (positive). In two-phase flow, a special case, which here is called *hybrid-sonic* flow, can occur if three of the eigenvalues are positive and one is negative. In Table 6.1, this is the situation for all three cases. This is in contrast to the *subsonic* situation where two of the eigenvalues are positive and two are negative. In Chapter 3 we learned that the sign of the eigenvalue tells us whether the characteristic wave is leaving or entering the domain, and thus the number of physical boundary conditions to specify. When the flow is hybrid-sonic, one boundary condition is specified at the outlet, and when the flow is subsonic, two boundary conditions must be provided. In two-

dimensional flows, the situation can be rather complex, since hybrid-sonic and subsonic zones can occur along the same boundary. In addition, the system matrix $\boldsymbol{A}$ is singular at the transition point between hybrid-sonic and subsonic flow. This can easily be verified from the definition of the eigenvalues: $\det(\boldsymbol{A} - \lambda \boldsymbol{I}) = 0$, and hence if one of the eigenvalues are zero, then $\boldsymbol{A}$ is singular, ($\det(\boldsymbol{A}) = 0$).

Complex eigenvalues

Another issue in multiphase flow is the fact that the mathematical model may exhibit complex eigenvalues. This is the case for the equal-pressure model, where $p_k = p_k^i = p$, (Drew and Passman, 1999, Chapter 20). In our formulation, the equal-pressure model appears when the interface pressure coefficient $B_k = 1$. When the model possesses complex eigenvalues, it is ill-posed as an initial value problem. This may lead to several undesirable effects, like exponential growth and grid-dependency. Complex characteristics and ways to render real characteristics have been treated in the literature, e.g. by Ramshaw and Trapp (1978), Lee *et al.* (1998), Chung *et al.* (2000, 2002).

Even if the inviscid problem is ill-posed, the inclusion of diffusion may lead to a stable problem. Bedjaoui and Sainsaulieu (1997) analysed this case with a gas and a liquid phase and found two complex eigenvalues. They proved global existence of the solutions of a system of PDEs with complex characteristics when the diffusion and interface friction are large enough.

In their book, Drew and Passman (1999, Chapter 20.6) write:

> The problem of complex characteristics seems to arise from the coupling between the two momentum equations, since it does not appear in models, which have only one momentum equation. The argument has been advanced that viscosity will change the type of partial differential equations, and the problem of complex characteristics will be irrelevant. While it is true that a viscous system has real characteristics, in the limit of vanishing viscosity, the complex characteristics of the inviscid system give rise to small-scale instabilities which are artifacts of the model, and not physical real.
>
> Thus, effort should be devoted to understanding the inviscid,

> incompressible, two-fluid momentum equations. The alternative of including differential terms to force real characteristics, either in the name of engineering or by invoking continuum mechanics principles, is unsatisfactory. We believe that the systematic inclusion of all terms arising in the averaged momentum equations, each soundly based on physics, will yield an appropriate model.

As we see, the issue of complex eigenvalues is important. Extra attention is paid when the inviscid model has complex eigenvalues, especially since the inviscid model is used in the boundary treatment.

Complex characteristics and boundary conditions

The boundary treatment in Chapter 3 is based on a LODI approach, and the LODI system is assumed to be hyperbolic for the treatment to be correct. A system of the form

$$\frac{\partial \boldsymbol{U}}{\partial t} + \boldsymbol{A}\frac{\partial \boldsymbol{U}}{\partial x} = \boldsymbol{C} \tag{6.1}$$

is called weakly hyperbolic if the $m \times m$ matrix $\boldsymbol{A}$ is diagonalisable, with real eigenvalues, (Leveque, 2002, Chapter 2). A more strict condition, namely strong hyperbolicity, requires that all eigenvalues of the characteristic matrix are real and distinct. For initial-value problems, appearance of complex eigenvalues indicates existence of multiple solutions state (Dinh *et al.*, 2003).

Hirsch (1988, Page 140) says the system is hyperbolic if all characteristic normals are real and if the solutions of the associated systems of equations are linearly independent. If all the characteristics are complex, the system is said to be elliptic, and if some are real and others complex, the system is considered as hybrid. If the matrix $\boldsymbol{A}$ does not possess a full rank, then the system is said to be parabolic.

In the numerical implementation, only the real part of the complex numbers is used. A question is whether the boundary treatment will work when $\boldsymbol{A}$ has complex eigenvalues. This is examined later in this chapter. Now the discussion continues by exploring when the inviscid model has complex eigenvalues.

By varying the interface pressure coefficient, B_k, complex eigenvalues may occur. In Table 6.1, the limit for real eigenvalues is given by $B_{k-\text{lim}}$. If B_k is larger than $B_{k-\text{lim}}$, then the eigenvalues are complex. The eigenvalues are dependent of the B_k. To study this for Case 2, two of the eigenvalues, λ_2 and λ_3, are plotted against different values of B_k as B_k approaches 1 in Figure 6.1. To the right of the dashed vertical line, at $B_k \geq B_{k-\text{lim}} = 0.9999980$, in Figure 6.1, λ_2 and λ_3 are complex. In this region, the real component of λ_2 and λ_3 are equal. Complex eigenvalues may also occur depending on the local flow situation. In Case 2, for instance, the eigenvalues are complex if $u_1 \geq 2.88\,\text{m/s}$.

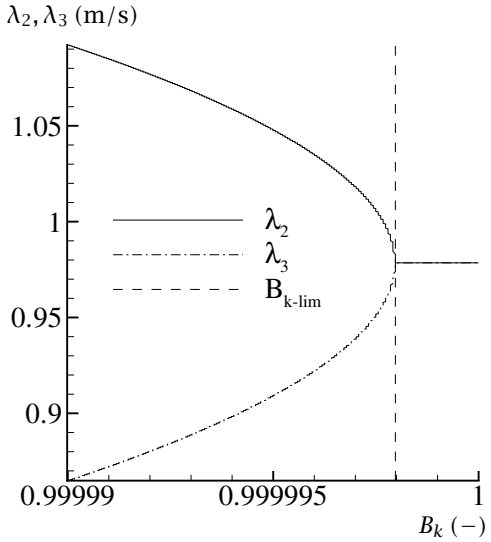

Figure 6.1: Two of the eigenvalues of $\boldsymbol{A}$ in Case 2 as B_k approaches 1.

Summary

We have seen that the signal-speeds are reduced in a two-phase mixture. We have also seen that the inviscid model may possess complex eigenvalues depending on the local flow situation or the value of the interface pressure coefficient. The issue of complex eigenvalues has been briefly discussed and the importance is realized. Although a more detailed mapping of when complex eigenvalues occur should be carried out. This question is left for

now since the map will vary from case to case. Therefore, we continue by studying the boundary conditions in one-dimensional flow.

6.2 One-dimensional computations

After having explored some of the mathematical challenges in two-phase flow, we are now ready for flow computations, and ready to explore the behaviour of the newly developed boundary treatment.

The first case to explore is a case where perfectly non-reflecting boundary conditions may be used.

6.2.1 Non-reflecting boundary conditions — the shock-tube

The shock-tube case is known from single-phase flow to work well and has also been used in multiphase flow (Saurel and LeMetayer, 2001). The shock-tube case displays strong wavy behaviour and is therefore a good test for the boundary conditions. Note that in the present work, the focus has been on the boundary treatment, and not on the resolution of shocks.

Problem description

A shock-tube filled with air and water with initial shocks in pressure and volume fraction is studied under two different configurations:

1. Symmetric initial-pressure and volume-fraction shock.
2. Symmetric initial-pressure and volume-fraction shock with three positive and one negative eigenvalues of $\boldsymbol{A}$.

Both cases are studied with perfectly non-reflecting boundary conditions on both sides, i.e. the incoming wave amplitudes, $\mathscr{L}_i^-$, are set to zero. When the interface friction term is set to zero, this case is not expected to give drifting values, since $\partial/\partial x = 0$ and then $\mathscr{L}_i = 0$ in the steady solution.

All the cases were run with the RKFV method (Chapter 4). The phase-properties and parameters for the numerical method are given in Table 6.2, and Table 6.3 respectively. In Table 6.2, phase 1 refers to the air-phase, and phase 2 refers to the water phase.

Table 6.2: Phase properties.

Property	Symbol	Unit	Phase 1	Phase 2
Speed of sound	c_k	m/s	340	1400
Reference density	ρ_k°	kg/m^3	0	1000
Viscosity	μ_k	Ns/m^2	0.0018	0.08

Table 6.3: Parameters for the RKFV method.

Property	Symbol	Unit	Values
Length of domain	L	m	10
Number of grid-points	-	–	101
Convective discretisation	-	–	Power-Law
Time-step	δt	s	$2.97 \cdot 10^{-4}$

Subsonic flow

Since the initial values are symmetric, the solution will be symmetric. The converged solution is always subsonic since both u_1 and u_2 are zero, $\alpha_1 = 0.5$ and $p = 1.2$ bar. Therefore only the positive eigenvalues, ($\lambda_3 = -\lambda_2$ and $\lambda_4 = -\lambda_1$), are presented in Table 6.4 for the different cases.

Table 6.4: Eigenvalues as a function of B_k

B_k	λ_1	λ_2	$\varkappa = \lambda_1/\lambda_2$
0	340.00	15.49	21.95
0.9	340.15	4.89	69.46
0.95	340.16	3.46	98.25
0.97	340.16	2.68	126.80
0.98	340.16	2.19	155.30
0.99	340.16	1.55	219.69
0.995	340.16	1.09	310.69
0.999	340.16	0.49	694.74
0.9999	340.16	0.16	2196.96
1.0	340.16	0.0	∞

In this table, the condition number $\varkappa = \lambda_1/\lambda_2$ of $\boldsymbol{A}$ will give an indication of how fast the system will converge. A reduced timescale is chosen as $t' = ct/L$, where $c = c_1$ is the sound speed of air. A t' value of 1 corresponds approximately to the time waves associated with λ_1 will need to propagate

through the domain and a t' value of $\varkappa$ corresponds to those of λ_2.

The time step is restricted by a CFL criterion. Leveque (2002, Chapter 4.4, Equation 4.17) writes the CFL-number as:

$$\mathrm{CFL} = (\lambda_{\max})\delta t/\delta x, \tag{6.2}$$

here $\lambda_{\max} \approx c_1$. A CFL number of 1 is used for the simulations in this case.

In Figure 6.2, the time-history $ct/L = 0, 40, 80, 120, 235$ for $B_k = 0.99$ with an initial shock in the volume fraction is shown. The initial shock is computed using the tanh function, which is smooth and infinitely differentiable. The steady solution is reached at $ct/L \approx 235$ and this agrees well with Table 6.4, where $\varkappa = 220$.

This case was also tested with $B_k = 0, 0.9, 0.95, 0.97, 0.99, 0.999$ and 0.9999, as well as with initial shock in the pressure, and with initial shock in the pressure and volume-fraction. In the cases with values of B_k close to 1, the problem exhibited complex eigenvalues in the beginning. Still the problem converged to the steady solution.

The initial shocks created in the u_1-velocity are different for different values of B_k. For example, the initial shocks in the u_1-velocity when $B_k = 0.9$ are approximately five times as large as the initial shocks in the u_1-velocity when $B_k = 0.99$.

All cases converged to steady state and the boundary behaviour was perfectly non-reflecting. As can be seen by observing the graphs at $x = 0$ and $x = 10$ in Figure 6.2.

Hybrid-sonic flow

If the symmetric case is calculated with an initial water-phase velocity of $u_2 = 30\,\mathrm{m/s}$, three of the eigenvalues will be positive and we have a hybrid-sonic situation. In this case, the initial shocks will be convected out of the domain and converge faster to steady state. For B_k close to 1, the eigenvalues will be complex all the time, and still the computations converge to the steady solution. Again the boundary conditions showed perfect non-reflecting behaviour. Some of the cases were also run with the RKFD method and gave equivalent results.

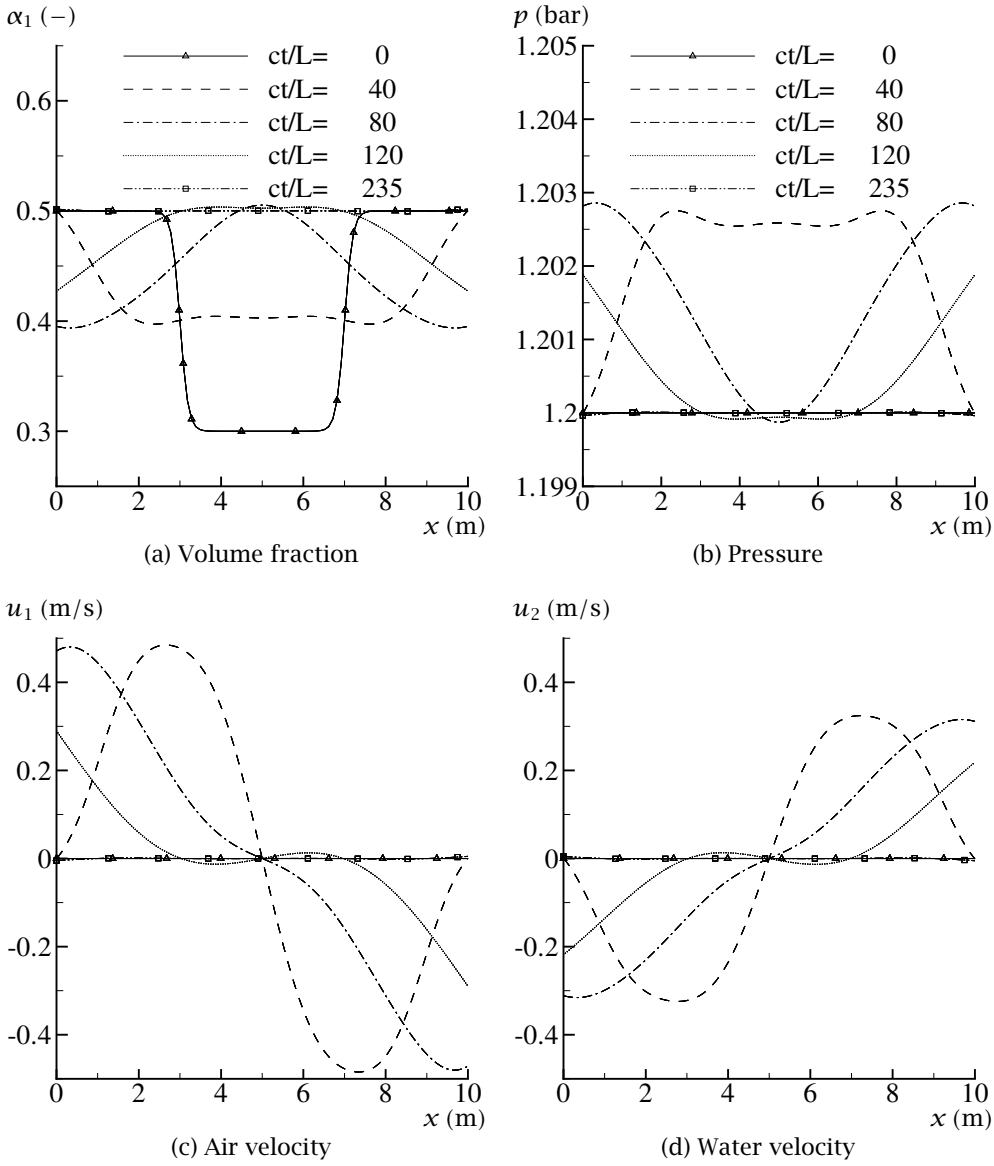

Figure 6.2: The time-history for $B_k = 0.99$.

Summary

We have seen that the perfectly non-reflecting boundary conditions works as expected, for subsonic and hybrid-sonic flow, and even when the eigenvalues were complex. As discussed in Chapter 3, perfectly non-reflecting boundary conditions may in some cases lead to drifting values. Therefore, perfectly non-reflecting boundary conditions are not discussed further in this thesis. Now, the next step is to study reflecting boundary conditions.

6.2.2 Reflecting boundary conditions

In a two-dimensional situation there may be regions at the boundary with hybrid-sonic flow and regions with subsonic flow. In the region with subsonic flow, we have two positive and two negative eigenvalues in contrast to the region with hybrid-sonic flow, where three eigenvalues are positive and one is negative. This, combined with the different possibilities for the boundary conditions, requires an one-dimensional investigation.

Problem description

A 1 m long tube with inlet and outlet is computed. The phase properties are the same as those in the last section, i.e. air and water, with the properties as given in Table 6.2. In Table 6.5, the specification of the case and the numerical method are given. In two-dimensional flow, friction from the wall is accounted for by default, here this effect is represented by adding a friction term in the momentum equations:

$$\frac{1}{2}\frac{f_{m,k}}{D_h}u|u| = f_k u|u|, \tag{6.3}$$

where $f_{m,k} = 0.003$ is a Moody friction-parameter and $D_h = 0.2\,\mathrm{m}$ is the diameter of the pipe.

Hybrid-sonic flow

With $B_k = 0.9999$, three of the eigenvalues are positive, and hence three inlet conditions must be specified. α_1, u_1 and u_2 are imposed by specifying the time-derivative at the boundary, i.e., calculating $\mathscr{L}^-$ from Equation (3.16). At the outlet, the pressure p is imposed by using a PI-controller,

Table 6.5: Specification of the case and the numerical method.

Parameter	Symbol	Unit	Values
Length of domain	L	m	1
Number of grid-points	-	–	51
Imposed inlet air-velocity	u_1	m/s	1.5
Imposed inlet water-velocity	u_2	m/s	1
Imposed inlet/outlet volume fraction	α_1	–	0.5
Imposed outlet pressure PI-controller	p	bar	1
Interface friction parameter	C	m^{-1}	1

see Equation (3.20), with the controller parameters, $(\mathscr{L}^-)^\circ = 0$, $K_D = 0$, $K_P = \sigma(1-\mathscr{M}^2)c_1/L$, $K_I = K_p$, $\mathscr{M} = u_1/c_1$.

As shown in Figure 6.3, this case has been computed with RKFD (Section 4.3), and RKFV (Section 4.2). RKFV was run with the POW and SOU schemes (Section 4.2.1). First observe that the results do not differ much. RKFV-SOU and RKFD are almost identical in the plots. Since RKFV-SOU and RKFD give the same results, only RKFV-SOU is used in the rest of this section.

An effect which is observed is that the pressure and air velocity seam to have the same shape. This seems also to be the case for the volume fraction of air, α_1, and the water velocity, u_2. The reason for this will be explained in Section 6.3.

Subsonic flow

In Figure 6.4, the same case is computed, but with $B_k = 0.99$. This leads to the subsonic situation, therefore the time derivatives of u_1 and u_2 are imposed at the inlet, and at the outlet where α_1 and p are imposed with the MPCBC method (Section 3.5.3), the same PI-controller as in the previous example is used.

Physical relevance of subsonic flow: Before discussing results from subsonic flow, the physical relevance of subsonic flow needs to be discussed. Since two of the eigenvalues are negative, two boundary conditions needs to be specified at the outlet. Here, we have chosen to specify α_1 and p with

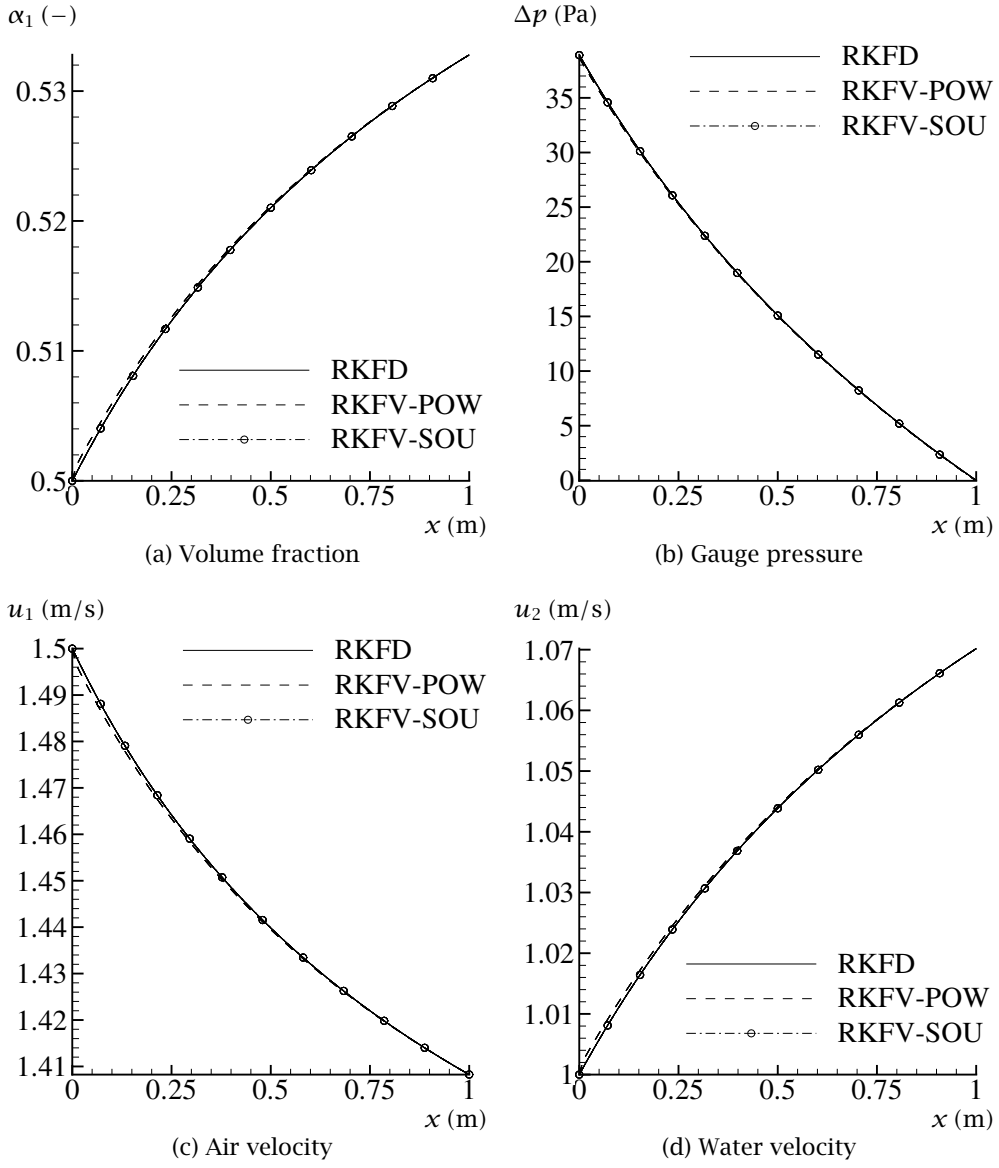

(a) Volume fraction

(b) Gauge pressure

(c) Air velocity

(d) Water velocity

Figure 6.3: Hybrid-sonic flow, B_k=0.9999.

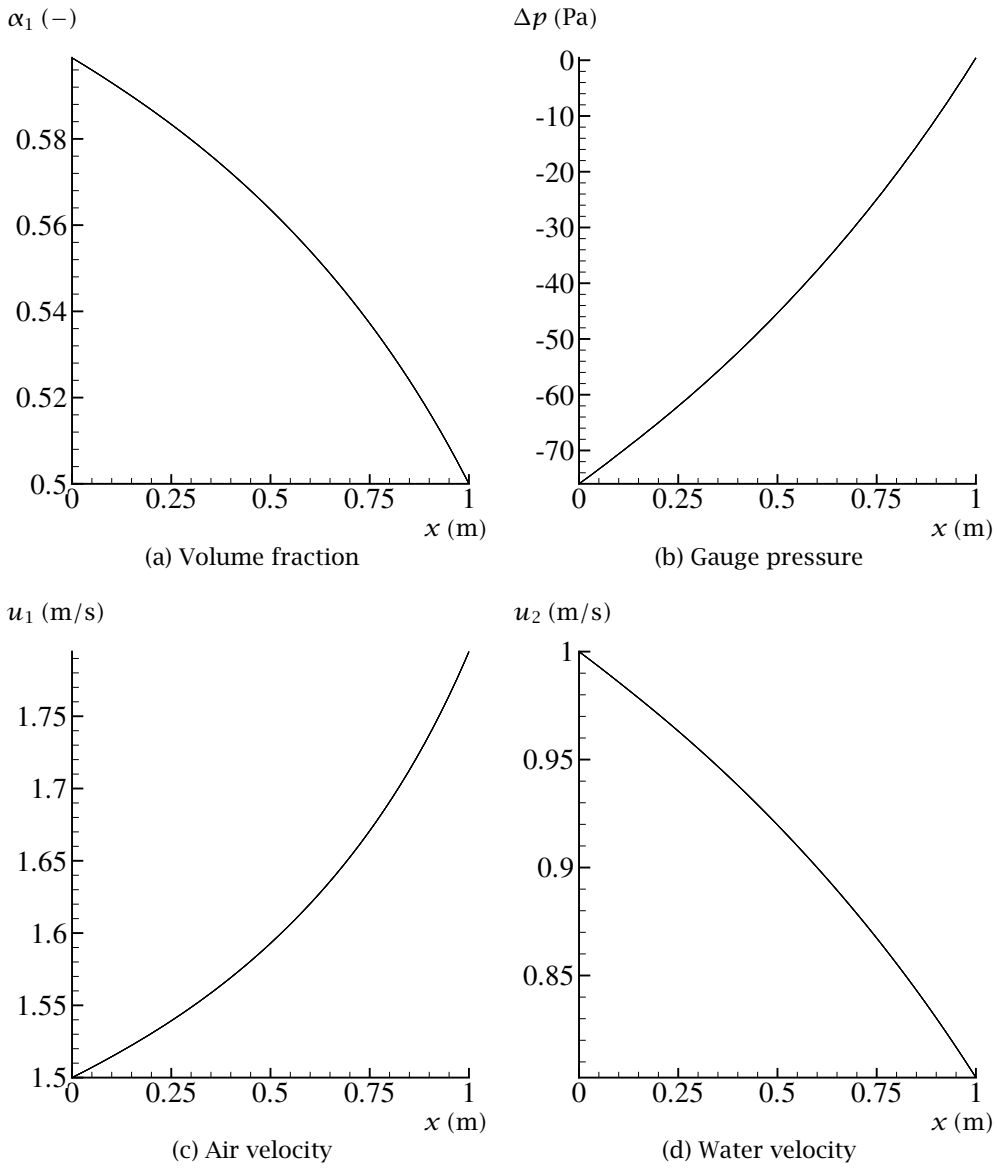

(a) Volume fraction

(b) Gauge pressure

(c) Air velocity

(d) Water velocity

Figure 6.4: Subsonic flow, B_k=0.99.

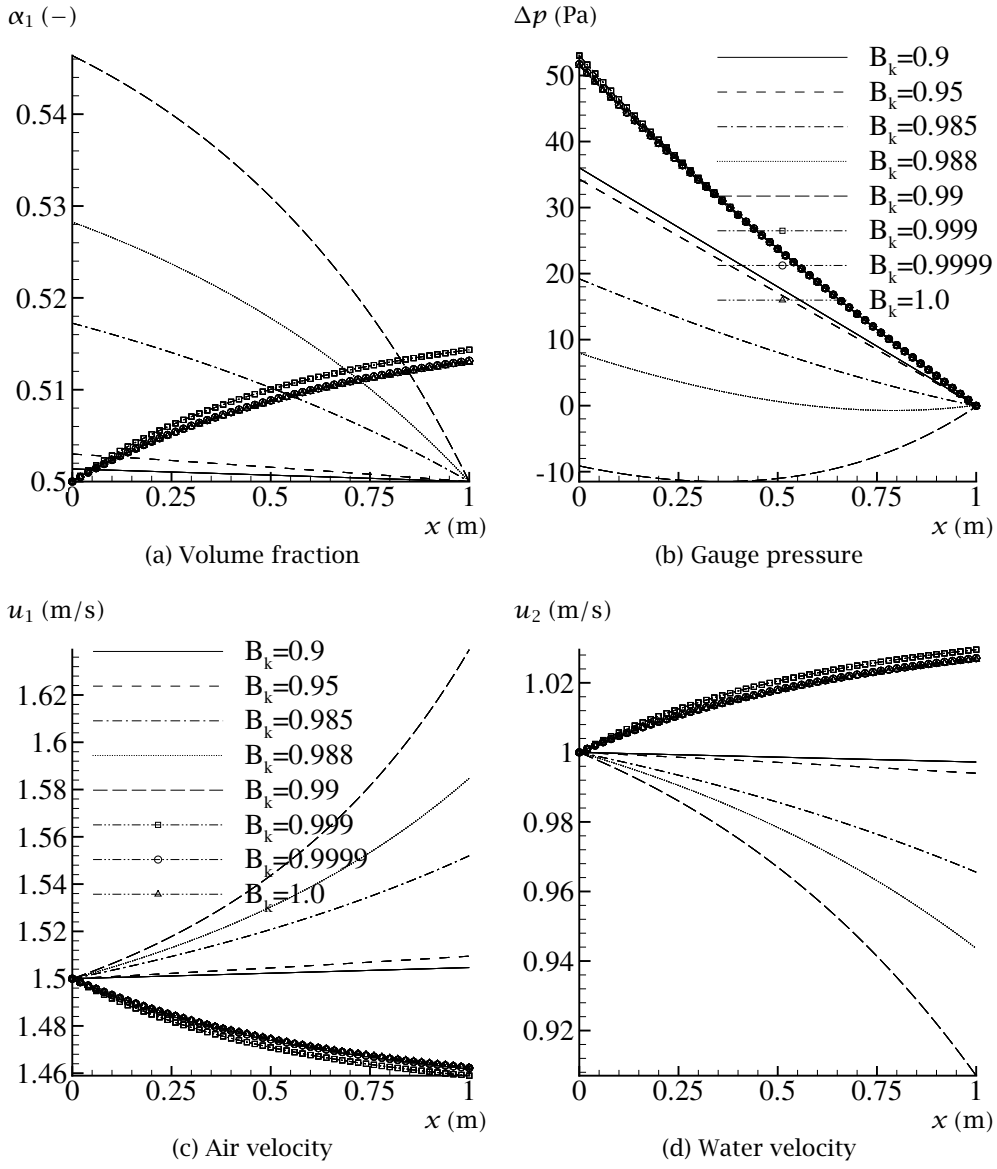

(a) Volume fraction

(b) Gauge pressure

(c) Air velocity

(d) Water velocity

Figure 6.5: $f_{m,k} = 0.03$, $C = 1.0\,\mathrm{m}^{-1}$, varying B_k.

the MPCBC method. From a physical point of view it seems strange that the volume fraction is specified at the outlet. It seems natural to impose one boundary condition at the outlet and three at the inlet. The physical relevance of subsonic flow may therefore be irrelevant. At the moment, a conclusion of this point is not drawn. Therefore, subsonic flow is also computed and examined with respect to the boundary conditions.

Increasing pressure: In Figure 6.4(b), the pressure increases along the pipe. This result is surprising and a more detailed investigation is required. Some points are still worthwhile noting: By reviewing Table 6.4, we see that one of the eigenvalues will almost be zero at $B_k = 0.995$, leading to extremely slow convergence. Finding a solution in this case was therefore given up. In Figure 6.5, $f_{m,k}$ is increased from 0.003 to 0.03. Observe then that the subsonic cases move towards lower pressure drop as B_k is increased towards 0.995. For the hybrid cases, which are marked with symbols as well as lines, the curves are hardly changing when B_k is changed from 0.999 to 1.0, and when $B_k > 1$ the computations diverge. Still this does not explain why the pressure increases along the pipe. This question is left for now and examined more closely in Section 6.3.

Transient behaviour of the boundary conditions

Until now we have examined only the steady solution where the boundary conditions give excellent results. There are several possibilities for the choice of boundary conditions, and in order to get more insight into how the different boundary conditions perform, the time-history at the outlet is plotted for these arrangements:

1. PIO: PI-controller at the outlet.
2. PIO2: PI-controller at the outlet, $K_P^{\mathrm{PIO2}} = 0.5\, K_P^{\mathrm{PIO}}$.
3. PIIO: PI-controller at the inlet and the outlet.
4. PO: P-controller at the outlet.

Again these cases are computed with a phasic moody-factor of $f_{m,k} = 0.03$ and interface friction parameter $C = 1.0\,\mathrm{m}^{-1}$. In Figure 6.6, the time-history

at the outlet is plotted in the hybrid-sonic case, i.e. with $B_k = 0.9999$, and in Figure 6.7, the time-history is plotted for the subsonic case ($B_k = 0.9$). Before the different controllers are compared, we will do some observations for the two cases.

Observations in the hybrid-sonic case

In the hybrid-sonic case, in Figure 6.6, the flows are computed to $t' = 600$. All reach the steady solution in that time, except PIIO which converges slower. During the computations, complex eigenvalues occurred, leading to a situation where the boundary treatment may fail. However, the results obtained were excellent and thence the boundary conditions may be used in this case as well.

Observations in the subsonic case

The subsonic cases need more time to converge, therefore the subsonic cases are computed to $t' = 3000$. In contrast to the hybrid case, waves are travelling back and forth as the computations slowly converge to steady state. The boundary conditions give satisfactory results for the subsonic cases, although a better damping of the reflected waves are preferred. This is believed to be possible to some extent, by tuning the control parameters. The different controlling methods gave fairly the same transient behaviour.

Comparison of the PO-method with the PI-methods

The first thing to observe, in Figure 6.6 and in Figure 6.7, is that the P-controller (PO) does not converge to the imposed pressure for the hybrid case, and neither the volume fraction nor the pressure converge to the imposed values in the subsonic case. This behaviour is what we would expect from a P-controller. Second, the gauge-pressure in Figure 6.6(b) increases steadily to 65 Pa and falls gradually to about 50 Pa. A small plunge is observed at $t' = 280$. Remember from Table 6.4 that the eigenvalues are approximately $u_1 \pm c_1$ and $u_2 \pm 0.15$ m/s, the smallest are in this case approximately 1.2 m/s and 0.89 m/s, and hence waves travelling at the lowest speeds use a reduced time of $t' = 340/1.2 = 280$ to reach the outlet from the inlet.

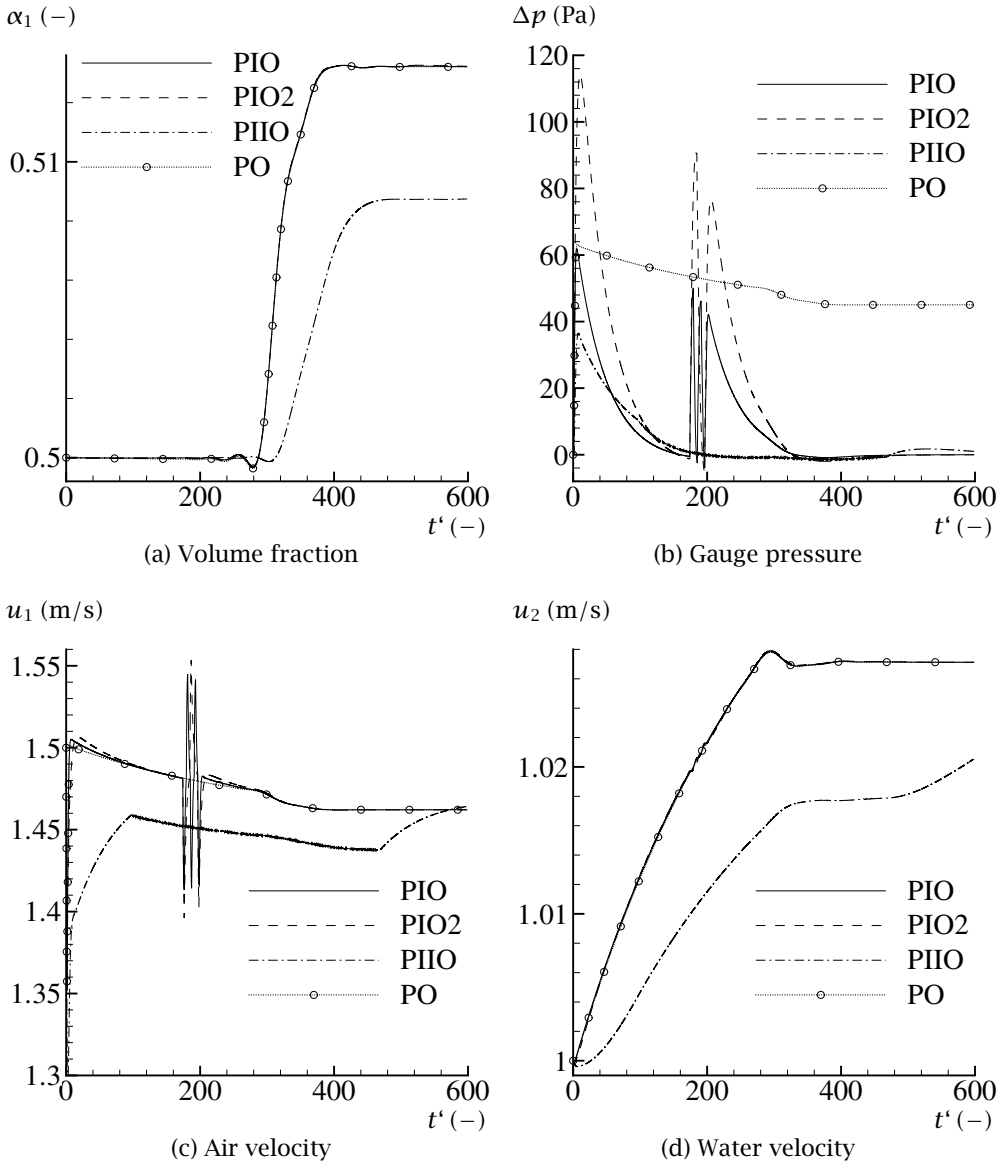

(a) Volume fraction

(b) Gauge pressure

(c) Air velocity

(d) Water velocity

Figure 6.6: The time history at the outlet for different boundary arrangements — Hybrid-sonic ($B_k = 0.9999$).

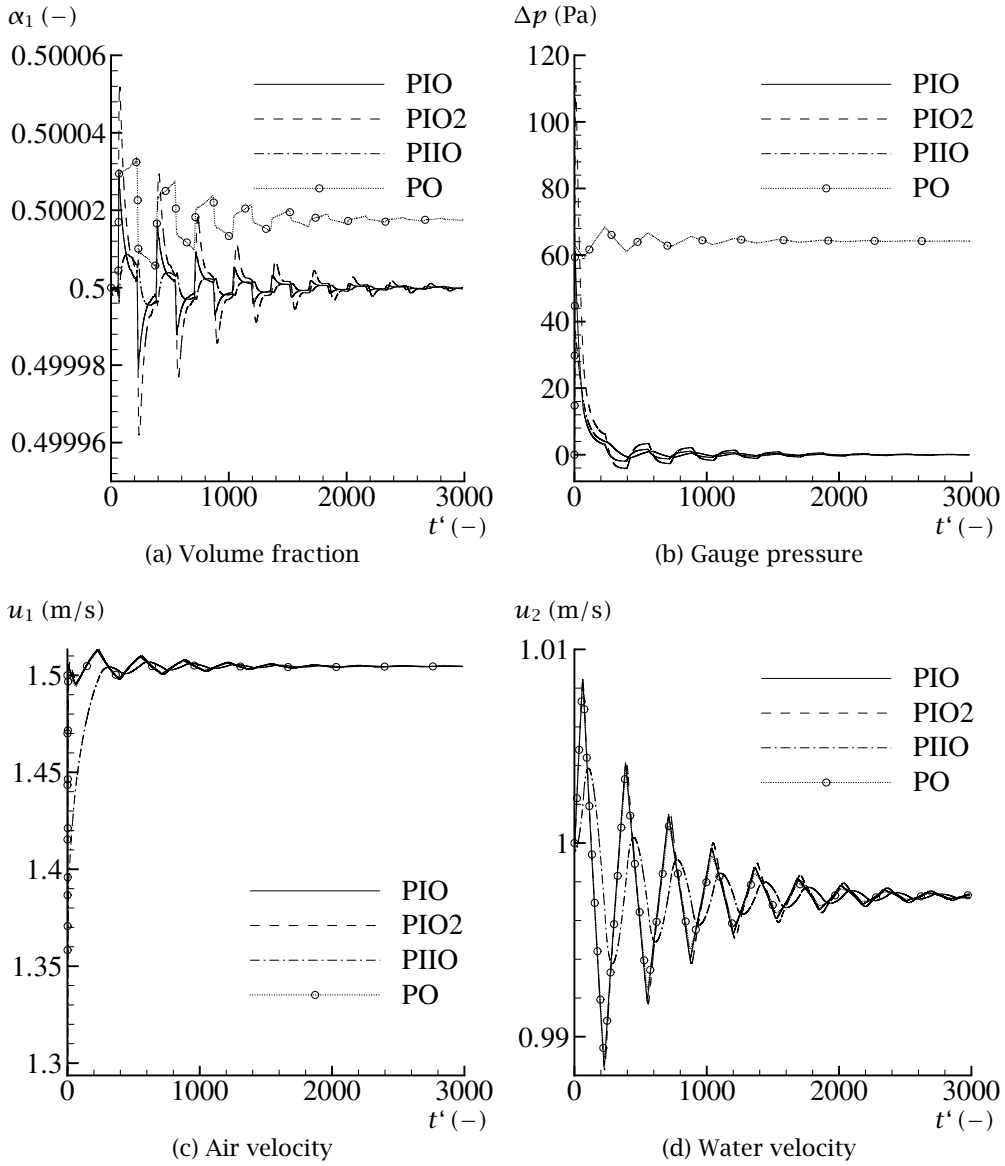

Figure 6.7: The time history at the outlet for different boundary arrangements — Subsonic ($B_k = 0.9$).

Comparison of PIO and and PIO2

Recall that the difference between PIO and PIO2 is only that K_P of PIO2 is half that of PIO. The pressure fluctuations and the volume-fraction fluctuations (in the subsonic case) for PIO2 is twice that of PIO.

As opposed to the other control-methods, fluctuations in the pressure and in the air velocity occurred at $t' = 200$ for the PIO and PIO2 in the hybrid case. Besides that they should occur at $t' = 280$ and not $t' = 200$, these fluctuations may be due to disturbances generated at the inlet at startup. A more thorough investigation of why this is the case should be carried out, however this is considered to be beyond scope of the thesis.

Observations for the PIIO control-method

In the PIIO control-method, a PI-controller is used for the velocities at the inlet as well as the PI-controller for pressure (and volume fraction) at the outlet. The steady solution was not reached for the computed time in the hybrid case, it did converge but only later. This is due to the controller at the inlet also needs time to reach the imposed values. In the subsonic case, the transient behaviour was more smooth than the other controlling methods, as can be seen in Figure 6.7(d).

Summary

The one-dimensional flow model has been solved numerically with the proposed boundary treatment. Hybrid-sonic and subsonic flow have been computed with different boundary arrangements. The boundary treatment worked well in the hybrid-sonic case. In the subsonic case, the damping of the reflected waves were not satisfactory. The PIIO method needed more time to converge than the other arrangements. The PIO method had the same transient behaviour as the PO method. The model predicted a positive pressure gradient in the subsonic case. This may be indicative of either unphysical parameters of the model or that boundary treatment may be in error. Therefore, the discussion now continues by a investigating these issues.

6.3 Investigation of positive pressure gradient

In Figure 6.4, in the previous section, it was discovered that the model predicts positive pressure gradient along the pipe for a given parameter range. This section attempts to examine this issue more closely.

6.3.1 Steady solution

The first question which arises is whether this behaviour is due to the boundary treatment.

To answer that question, assume that the transient problem

$$\frac{\partial \boldsymbol{U}}{\partial t} + \boldsymbol{A}\frac{\partial \boldsymbol{U}}{\partial x} = \boldsymbol{C}, \tag{6.4}$$

which we solved in the previous section, has a steady solution. The problem reduces to an ordinary differential equation:

$$\frac{\partial \boldsymbol{U}}{\partial x} = \boldsymbol{A}^{-1}\boldsymbol{C}, \tag{6.5}$$

provided that $\det(\boldsymbol{A}) \neq 0$. Given that all initial values are specified at one location, Equation (6.5) can be integrated along x, with for instance the Runge-Kutta scheme given in Chapter 4. The cases in the previous section are recomputed with this solver, and the same results as before are obtained. This shows that the results in the previous section are indeed the steady solution, and hence the positive pressure gradient is not due to the boundary treatment.

6.3.2 Explicit pressure gradient

An explicit expression for the pressure gradient can be obtained when Equation (6.5) is evaluated. Recall from Chapter 3 that the following expression holds:

$$\frac{\partial \boldsymbol{U}}{\partial x} = \boldsymbol{A}^{-1}\boldsymbol{C} = \boldsymbol{Q}^{-1}\boldsymbol{D}. \tag{6.6}$$

Now write $\boldsymbol{D}$ as:

$$\boldsymbol{D} = \begin{bmatrix} 0 \\ 0 \\ R_1 \\ R_2 \end{bmatrix} = \begin{bmatrix} 0 \\ 0 \\ \alpha_1\rho_1(g\sin\beta - f_1 u_1|u_1|) + C_s \\ \alpha_2\rho_2(g\sin\beta - f_2 u_2|u_2|) - C_s \end{bmatrix}, \tag{6.7}$$

where C_s is the interface friction term:

$$C_s = C\rho_{\mathrm{m}}\alpha_1\alpha_2|(u_2 - u_1)|\,(u_2 - u_1)\,, \tag{6.8}$$

and $f_k = 1/2 f_{m,k}/D_h$. $f_{m,k}$ is the phasic Moody friction parameter and D_h the hydraulic diameter of the pipe.

It makes sense to group the sum of R_1 and R_2, since the interface friction term disappear when they are added:

$$R_1 + R_2 = \rho_{\mathrm{m}} g \sin\beta - (\alpha_1 f_1 \rho_1 u_1 |u_1| + \alpha_2 f_2 \rho_2 u_2 |u_2|)\,, \tag{6.9}$$

and

$$\rho_{\mathrm{m}} = \alpha_1\rho_1 + \alpha_2\rho_2. \tag{6.10}$$

With $\boldsymbol{Q}$ from Equation (3.68), evaluate Equation (6.6) and arrive at:

$$\frac{\partial\alpha_1}{\partial x} = \left(\frac{1}{K_d}\right)(N_2R_1 - N_1R_2)\,, \tag{6.11}$$

$$\frac{\partial p}{\partial x} = \left(\frac{p}{K_d}\right)\left(\frac{p_B\,(R_1+R_2) - \left(R_1\rho_2u_2^2 + R_2\rho_1u_1^2\right)}{p}\right), \tag{6.12}$$

$$\frac{\partial u_1}{\partial x} = \left(\frac{u_1}{K_d}\right)\left(R_2 - \frac{N_2}{\alpha_1}R_1 - \frac{\frac{\partial\rho_1}{\partial p}}{\rho_1}\left(p_B\,(R_1+R_2) - R_1\rho_2u_2^2\right)\right), \tag{6.13}$$

$$\frac{\partial u_2}{\partial x} = \left(\frac{u_2}{K_d}\right)\left(R_1 - \frac{N_1}{\alpha_2}R_2 - \frac{\frac{\partial\rho_2}{\partial p}}{\rho_2}\left(p_B\,(R_2+R_1) - R_2\rho_1u_1^2\right)\right), \tag{6.14}$$

where

$$K_d = p_B\,(N_1+N_2) - N_2\rho_1u_1^2 - N_1\rho_2u_2^2, \tag{6.15}$$

$$N_k = \alpha_k\left(1 - u_k^2\frac{\partial\rho_k}{\partial p}\right), \tag{6.16}$$

and

$$p_B = p\,(1 - B_k)\,. \tag{6.17}$$

With the equation of state,

$$\rho_k = \left(p + p_k^\circ\right)c_k^{-2}, \tag{6.18}$$

and with

$$\frac{\partial \rho_k}{\partial p} = c_k^{-2}, \tag{6.19}$$

this gives:

$$N_k = \alpha_k \left(1 - Ma_k^2\right), \tag{6.20}$$

where $Ma_k = u_k / c_k$ is the Mach number of phase k.

Separation by gravity

Assume that the two phases are at rest. In this case, $u_1 = u_2 = 0$, $N_k = \alpha_k$, $K_d = p(1 - B_k)$, $R_k = \alpha_k \rho_k g$. This gives the results from Chapter 2:

$$\frac{\partial \alpha_1}{\partial x} = \frac{\alpha_1 \alpha_2 g \left(\rho_1 - \rho_2\right)}{p \left(1 - B_k\right)}, \tag{6.21}$$

and

$$\frac{\partial p}{\partial x} = \rho_m g, \tag{6.22}$$

as expected.

6.3.3 Numerical investigation

The expressions for the gradients are fairly complicated and best understood when explored numerically. Since K_d occurs in all of the gradients, the discussion starts by examining K_d.

Examining K_d

If the phase Mach numbers are assumed to be small, then $N_k \approx \alpha_k$. This gives:

$$K_d = p_B - \alpha_2 \rho_1 u_1^2 - \alpha_1 \rho_2 u_2^2. \tag{6.23}$$

If we let only u_1 and u_2 vary, Equation (6.23) is an ellipse. Furthermore the gradients change sign when K_d does and they are not defined if K_d is zero. The equation for the $K_d = 0$ ellipse gets the form:

$$\left(\frac{u_1}{a}\right)^2 + \left(\frac{u_2}{b}\right)^2 = 1, \tag{6.24}$$

where $a = \sqrt{\frac{p(1-B_k)}{\alpha_2\rho_1}}$ and $b = \sqrt{\frac{p(1-B_k)}{\alpha_1\rho_2}}$. For air and water at $p = 1\,\text{bar}$, $\alpha_1 = 0.5$, and $B_k = 0.995$, the values of a and b are: $a = 34\,\text{m/s}$ and $b = 1\,\text{m/s}$.

Sign of gradients

In Figure 6.8, the sign of the gradients are shown for $\beta = 0$, $C = 1\,\text{m}^{-1}$, $B_k = 0.995$ and $f_{m,k} = 0.003$. The gradients are positive in the white areas and negative in the black areas. The ellipse (6.24) is recognised in these plots. The dimension of the ellipse increases if B_k is reduced and decreases as B_k approaches 1. At $B_k = 1$ the ellipse is reduced to a single point, $u_1 = u_2 = 0$. Observe in Figure 6.9(b) that the pressure gradient has regions where it is positive and where it is negative. If we assume that the expression for the pressure gradient can be written as:

$$\frac{\partial p}{\partial x} = \left(\frac{C_s}{K_d}\right)\left(\rho_2 u_2^2 - \rho_1 u_1^2\right), \tag{6.25}$$

then we see that the pressure gradient changes sign when $K_d = 0$, $C_s = 0$ or when $|u_1| = \sqrt{\frac{\rho_2}{\rho_1}}|u_2|$. This explains the sectors in Figure 6.9(b).

At the moment, our primary interest lies in the upper right quadrant of the charts and this part is shown in Figure 6.9. Based on this, it is clear that the modelling work must be performed with care. If the flow is close to the ellipse, the constant B_k-model may not be valid. As a way to maximise the areas where the constant B_k-model predicts physically meaningful results it makes sense to use $B_k = 1$.

Simplified expressions for the gradients when $B_k = 1$

In order to study the gradients when $B_k = 1$, the following assumptions are made: $N_k = \alpha_k = 0.5$, $C_s \gg f_k\rho_k u_k|u_k|$, and $\rho_2 \gg \rho_1$. This leaves us with

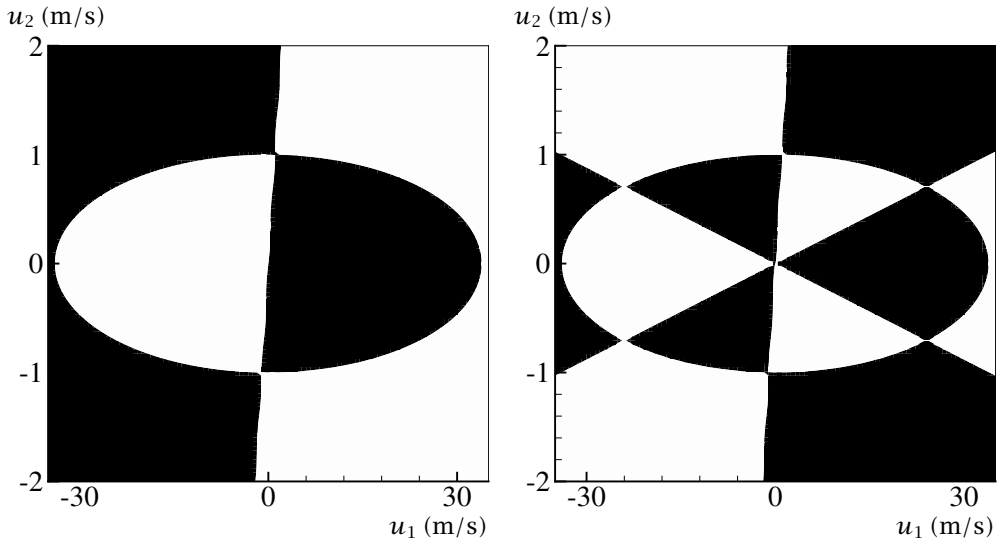

(a) Volume fraction

(b) Pressure

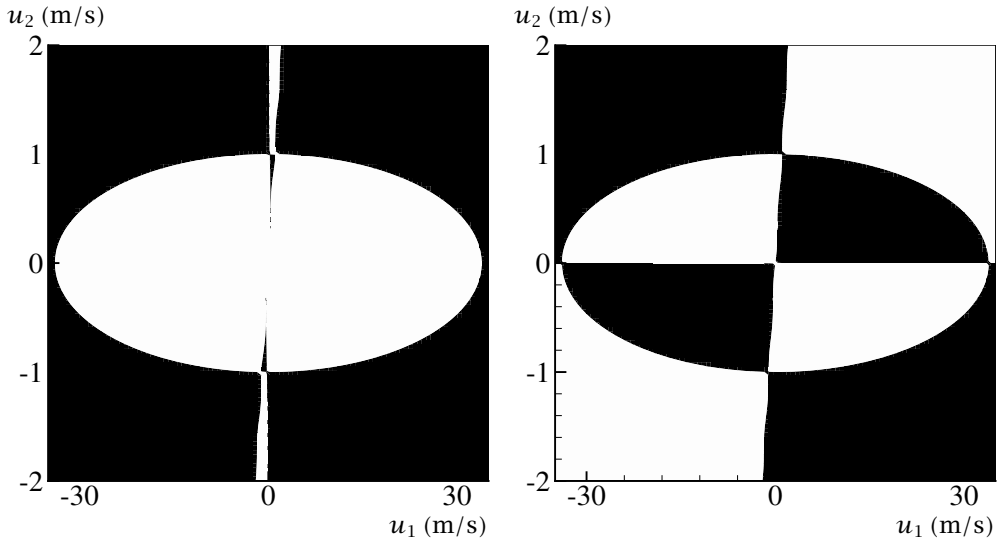

(c) Air velocity

(d) Water velocity

Figure 6.8: Sign of gradients, $B_k = 0.995$.

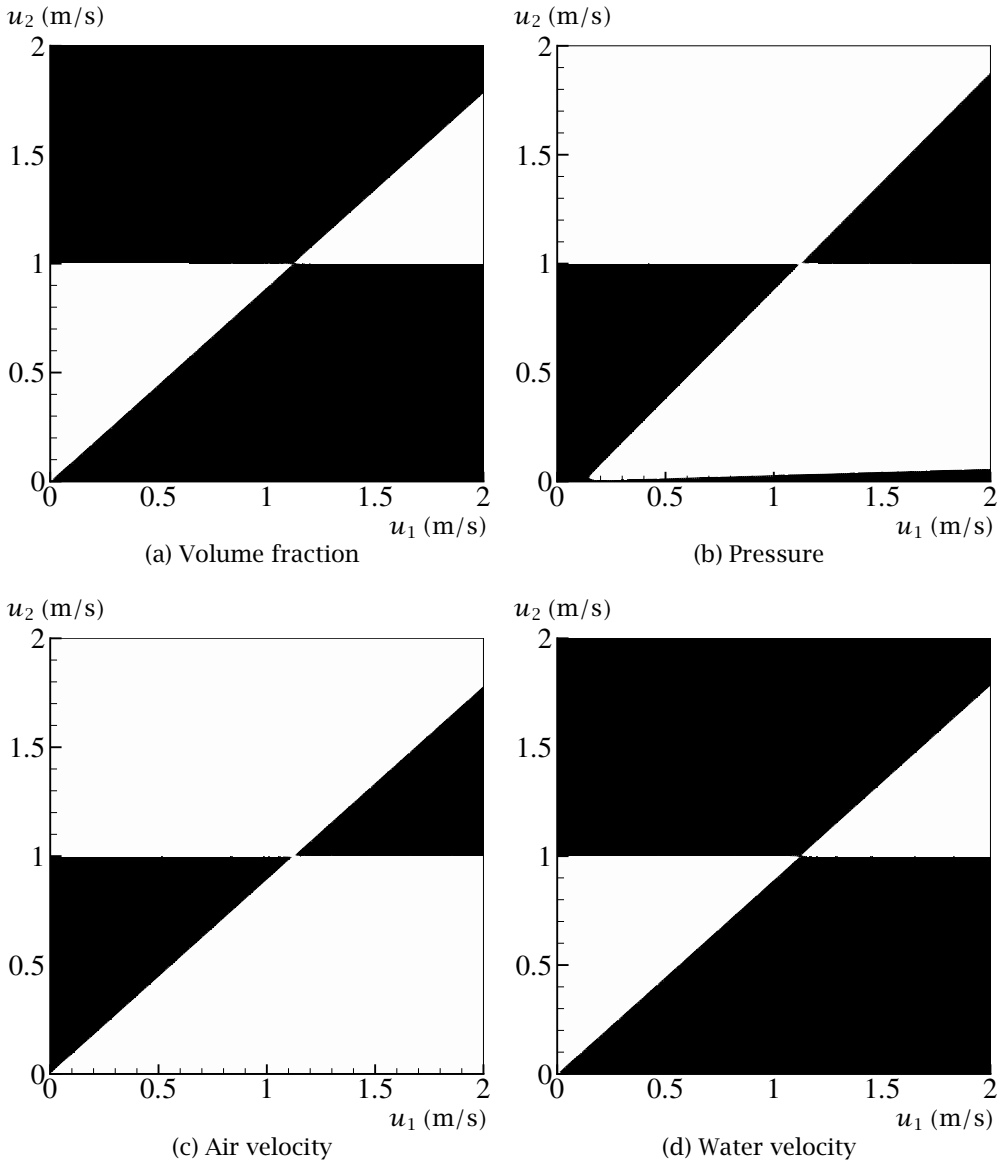

(a) Volume fraction (b) Pressure

(c) Air velocity (d) Water velocity

Figure 6.9: Sign of gradients, $B_k = 0.995$.

the following expressions for the gradients,

$$\begin{aligned}
\frac{\partial \alpha_1}{\partial x} &= \frac{\alpha_1}{K_d}(R_1 - R_2) = -2\frac{C_s}{\rho_2 u_2^2}, \\
\frac{\partial p}{\partial x} &= R_1 = C_s, \\
\frac{\partial u_1}{\partial x} &= \frac{u_1}{K_d}(R_2 - R_1) = 4\frac{u_1 C_s}{\rho_2 u_2^2}, \\
\frac{\partial u_2}{\partial x} &= \frac{u_2}{K_d}(R_1 - R_2) = -4\frac{u_2 C_s}{\rho_2 u_2^2}, \\
K_d &= -\alpha_1 \rho_2 u_2^2.
\end{aligned}$$

In the region where $u_1 > u_2$, the interface friction term is $C_s < 0$, which gives a negative pressure gradient. In the previous section we observed that the shape of the curves for the volume fraction and the water velocity seemed to be the same, as well as the shape of the pressure and air velocity curves. In Figure 6.9, the same observation is made for the sign of the gradients. The simplified expressions for the gradients explain this behaviour. By comparing $\partial \alpha_1 / \partial x$ with $\partial u_2 / \partial x$ and comparing $\partial p / \partial x$ with $\partial u_1 / \partial x$,

$$\frac{\partial u_2}{\partial x} / \frac{\partial \alpha_1}{\partial x} = 2u_2, \tag{6.26}$$

$$\frac{\partial u_1}{\partial x} / \frac{\partial p}{\partial x} = 4\frac{u_1}{\rho_2 u_2^2}, \tag{6.27}$$

we see that the curves will have the same shape.

Summary

The mathematical model has been examined with respect to a positive pressure gradient. The positive pressure gradient was not due to the boundary treatment, and therefore the constant B_k-model seems to be unphysical for some flow states. For $B_k = 1$ the unphysical flow state is reduced to no flow. To determine which states and parameters the mathematical model is unphysical, a more thorough investigation involving the second law of thermodynamics is required. This is beyond scope of the present work. Equipped with some understanding of the model, we may now move on to two-dimensional flow.

6.4 Two-dimensional computations

In this section, a mixture of air and water flowing in a two-dimensional horizontal channel is considered to study the performance of the boundary conditions. The same test as the one developed in Chapter 5 is used to evaluate the boundary conditions for pure hybrid-sonic flow and pure subsonic flow. In addition, the transient behaviour is examined by studying the inlet and outlet mass-flow rates.

6.4.1 Initial discussion

In a two-dimensional flow situation, a local transition from hybrid-sonic to subsonic flow may occur due to the presence of a velocity profile. Therefore, it makes sense to choose B_k such that no transition between hybrid-sonic flow and subsonic flow occurs along the boundaries. Further, the system matrix $\boldsymbol{A}$ is singular at the transition point. Singular points involves numerical difficulties. In single-phase flow, sonic flow is on such point, and special schemes are required, see Wesseling (2001, Chapter 10). Consequently, B_k is chosen such that no transition between hybrid-sonic flow and subsonic flow occurs.

Hybrid-sonic flow

By choosing $B_k = 1$, the flow will be pure hybrid-sonic, but separation by gravity is not defined for $B_k = 1$, see Equation (2.62). This problem can be overcome by using $B_{k,x} = 1$ in the x-direction where the gravity component is zero, and $B_{k,y} < 1$ in the y-direction where gravity is involved. Here, a value of $B_{k,y} = 0.98$ is used in the computations.

A side-effect of choosing $B_{k,x} = 1$ is that the eigenvalues are complex and hence the boundary treatment may fail. In the one-dimensional computations, the boundary treatment worked even with complex eigenvalues and therefore it is reasonable to assume that it will perform properly in two-dimensions as well. Drew and Passman (1999, Page 247) write:

> It seems clear that a formulation which produces complex characteristic values is physically unsound and in need of revisions to incorporate missing physics.

In addition, a model which is directionally dependent may be questionable. With the present model, this is an unsatisfactory compromise which has to be made. It is considered beyond the scope of this thesis to follow these questions and propose new models. Here, the important issue is that the computations are performed in pure hybrid-sonic flow and that no transition occurs. In the computations, a change of sign of the velocities at the inlet or outlet boundary leads to a situation where the number of physical boundary conditions to be specified changes. This is an unwanted situation and no change of sign of the velocities should occur during the computations.

Subsonic flow

In subsonic flow, the present equation system has at least two positive and two negative eigenvalues. Therefore, it is possible to specify the volume fraction and the pressure regardless of the local flow direction.

Furthermore, all the eigenvalues are real. From Table 6.4 we note that by choosing $B_k = 0.9$, subsonic flow will occur if u_2 is lower than $4.9\,\mathrm{m/s}$. Recall from Figure 2.2 on page 33 that $B_k = 0.9$ is not applicable to all kinds of flow, since the flow will hardly separate by gravity. This can be overcome by choosing $B_{k,y}$ closer to one and keeping $B_{k,x} = 0.9$. However, this will again lead to a directionally dependent B_k-model. For simplicity, $B_{k,x} = B_{k,y} = B_k = 0.9$ is used here.

6.4.2 Problem description

A mixture of air and water flowing in a two-dimensional horizontal channel with length $L = 1\,\mathrm{m}$ (see Figure 5.5 on page 73) and half-width $h = 0.1\,\mathrm{m}$ is studied here.

Initial values

Initial values for the pressure and the volume-fraction of air (α_1) are obtained by solving the separation by gravity problem from Section 2.3.2 in the y-direction. The separated solution is found by specifying $\alpha_1 = 0.5$ and

$p = 1\,\text{bar}$ at $y = 0$. The initial velocity profiles are:

$$u_k(x, y) = \frac{3}{2} u_{\text{m},k} \left(1 - (y/h)^2\right), \tag{6.28}$$

where $u_{\text{m},k}$ is the mean velocity of phase k. For the computations performed here, the mean velocity of air is $u_{\text{m},1} = 0.75\,\text{m/s}$ and the mean velocity of water is $u_{\text{m},2} = 0.5\,\text{m/s}$. The volume-flow rate of phase k is $\dot{Q}_k = u_{\text{m},k} 2h$.

Lateral boundary conditions

The lateral boundary conditions ($y = \pm h$) correspond to no-slip walls. For the walls, the unknown $\mathscr{L}_i$ could be found by specifying the velocity, however this is computationally expensive, and hence should be avoided whenever possible. In this case, the pressure and the volume-fraction of air is found by weighted linear extrapolation in the physical space (Melaaen, 1990, Chapter 2).

Inlet

At the inlet, the velocities, u_k and v_k are either specified with PI-controllers (PIIO) or set directly and using Equation (3.16) to find the unknown $\mathscr{L}_i$ (PIO).

The inlet u_k-velocities are set to the initial-value profile, Equation (6.28), and the v_k-velocities are set to zero.

In the case of hybrid-sonic flow, the volume-fraction of air is specified as well. The volume fraction is set to the profile obtained from separation by gravity, with $\alpha_1 = 0.5$ at $y = 0$. However, this profile should be recalculated during the computation since it depends on the actual pressure at $y = 0$.

Outlet

At the outlet, the pressure profile from separation by gravity, with $p = 1\,\text{bar}$ at $y = 0$, is specified with a PI-controller. As for the inlet, this pressure profile depends on the actual volume-fraction of air at $y = 0$, and hence should be updated during the computation.

Updating the imposed pressure is not necessary for subsonic flow since the volume fraction is specified as well.

Parameters for the PI-controllers

The MPCBC method of Section 3.5.3 is used together with PI-controllers to specify the variables. For the PI-controllers, the same controlling parameters are used for all variables. To find K_P, a simplified version of the formula in Chapter 5 is used: $K_P = \sigma c_1/L$, where $\sigma = 5$. For Channel C, where $2L = 2\,\text{m}$, and $c_1 = 340\,\text{m/s}$ the formula gives a K_P value of 850. The integral term K_I is set to K_P and the derivative term K_D is zero.

6.4.3 Viscous conditions

The phaseproperties are the same as those in Table 6.2. In the NSCBC method, extra viscous conditions were imposed in the calculation of the viscous tensor. For the single-phase channel flow, initial tests showed that the results were not sensitive to the specification of these terms. Initial tests in two-phase channel flow show the same behaviour. Therefore, no additional viscous conditions are specified for the computations performed here.

6.4.4 About the computations

The RKFV approach was unstable. A proper numerical filter was not available at the moment. All the computations have therefore been performed with the RKFD approach.

Spatial discretisation

The spatial domain is discretised with 41×41 points for Channel A and B. A, B, and C are names of the different parts of the channel as in Figure 5.5 on page 73. Channel C is discretised with 81×41 points. For the spatial derivative operator, the computations are performed with the fourth-order first-derivative operator. The solution is filtered, with the fourth-order filter after each time-step. The time step is calculated from the CFL-condition (Equation (6.2)).

Computing Channel A

The pressure at $y = 0$ and $x = L$ is read from Channel C and used to compute the separated pressure profile for Channel A. For the subsonic

case, the volume fraction is specified in the same manner.

Computing Channel B

The velocity profiles are read from Channel C at $x = L$ and used as inlet values for Channel B. For the hybrid-sonic case, the volume fraction is read from Channel C at $y = 0$ and $x = L$ and used to compute the separated profile.

Properties of the case

The phase properties are the same as those given in Table 6.2 on page 86. The interface friction parameter $C = 30\,\mathrm{m}^{-1}$.

Reduced time-scale

A reduced time-scale is $t' = u_{\mathrm{m},2}t/L$. The hybrid-sonic cases are computed to $t \approx 13\,\mathrm{s}$, which means $t'_{2L} \approx 3$ for Channel C and $t'_{L} \approx 6$ for Channel A and B. In Section 6.2.2, the subsonic cases were computed longer in order to find the steady solution, and hence the subsonic cases are computed to $t \approx 32\,\mathrm{s}$. However, the solution was found to be steady after $t' \approx 3$.

6.4.5 Results from hybrid-sonic flow

In this section, results from hybrid-sonic flow are presented. The presentation starts by presenting the steady solution, then the boundary conditions are evaluated with same test as developed in Chapter 5, and finally the transient solution is presented.

The steady solution

Before evaluating the boundary conditions, we will take a brief look at the steady solution. A glimpse into the two-dimensional structure of the flow can be achieved by studying contour plots.

In Figure 6.10–6.13, contour plots of the volume fraction, pressure, air velocity and the water velocity are presented. The plotted function is constant along the contour lines. From the contour plots, it is seen that the

flow develops along the channel and reaches fully developed flow. Observe that from the inlet to the fully developed section the air decelerates and the water accelerates, which is due to the interface friction.

In Figure 6.14, plots along the centreline ($y = 0$) are given. From these plots, we see that the flow becomes fully developed around $x = 0.6$ m. The pressure drop, Figure 6.14(b), is largest at the inlet where the slip, as seen in Figure 6.14(c) and Figure 6.14(d), and hence interface friction, is large. The pressure drop stabilises at about 80 Pa/m in the fully developed region. For the air velocity, Figure 6.14(c), a correction of the profile occurs around $x = 0.3 - 0.6$ m. This can also be seen in transverse plots.

In Figure 6.15, the transverse plots at the inlet, $x = L/2$ and $x = L$ are shown. The transverse air velocity is shown in Figure 6.15(c), where the same correction of the profiles is observed. A small upward shift of the air-velocity profile can be observed. This shift is believed to be stronger if the phase separation were stronger. We would expect to get a shift downwards for the water velocity profile. The opposite is observed in Figure 6.15(d).

From the contour, centreline, and transverse plots it is concluded that the boundary treatment gives a reasonable steady solution. The next step will be to evaluate the boundary conditions.

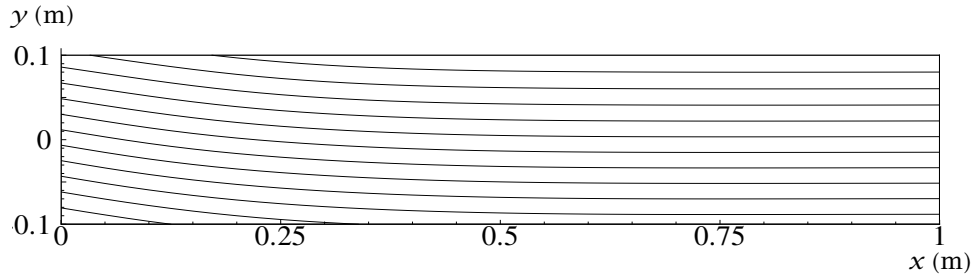

Figure 6.10: Contour plot of the volume fraction.

Comparison of Channel A, B, and C

The error-function, as for single-phase flow, Equation (5.8) on page 74, is computed to evaluate the boundary conditions. In Table 6.6, the maximum of the error-function is shown for Channel A and C, and in Table 6.7 for Channel B and C. The maximum of the error-function is presented for PIIO,

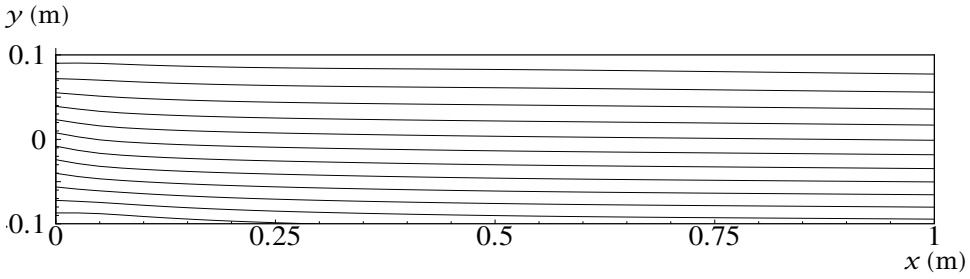

Figure 6.11: Contour plot of the pressure.

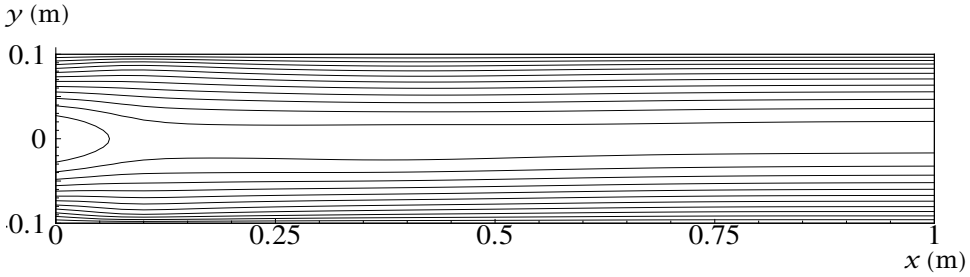

Figure 6.12: Contour plot of the air velocity.

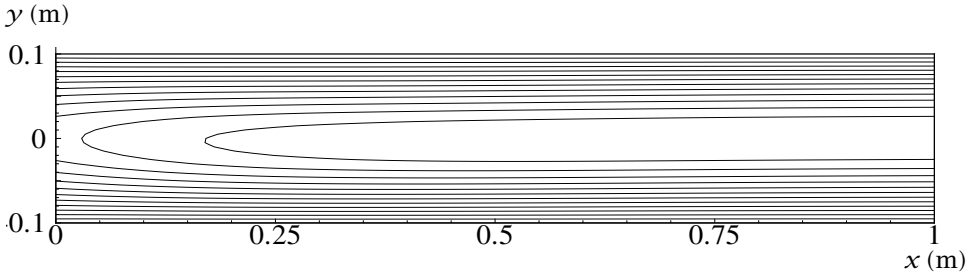

Figure 6.13: Contour plot of the water velocity.

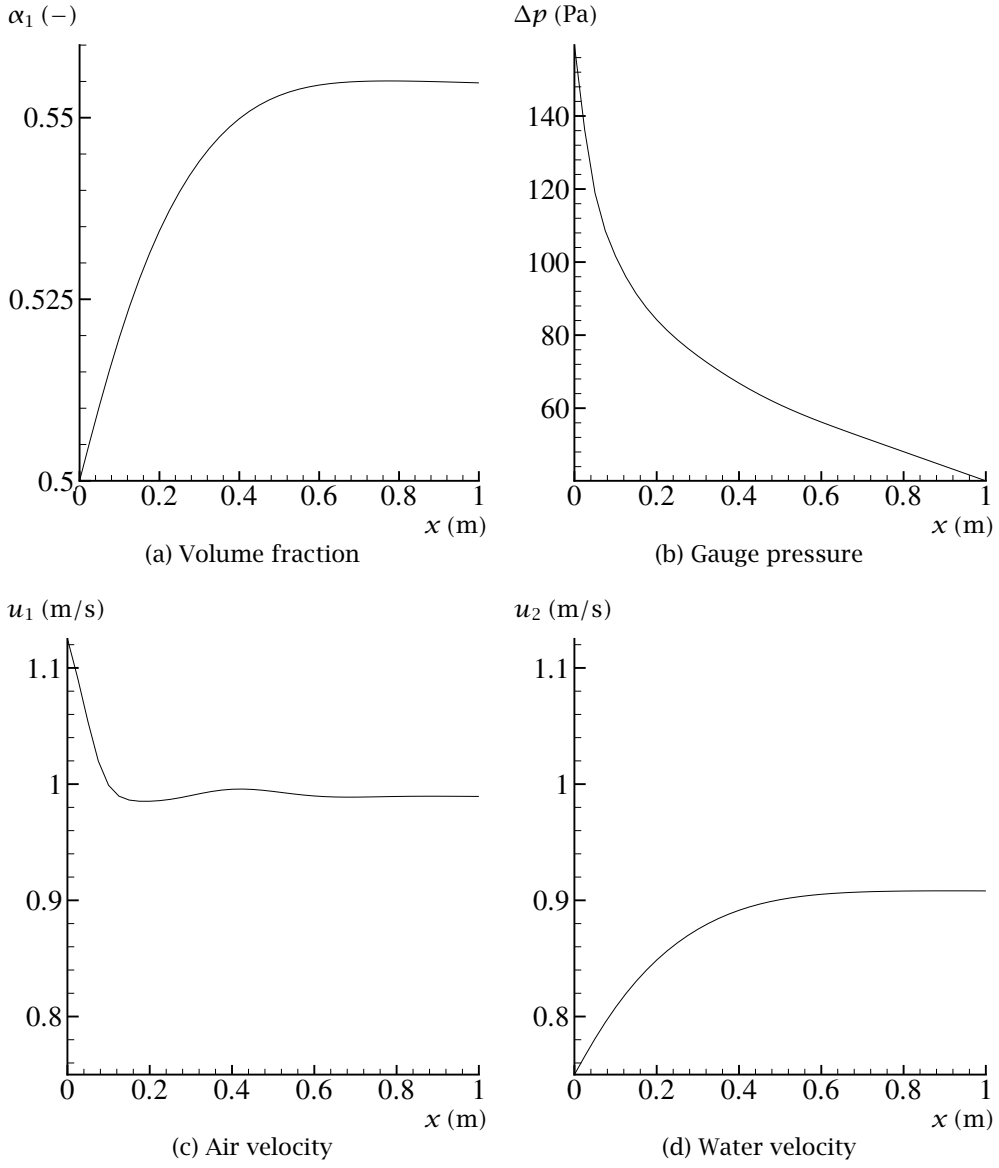

(a) Volume fraction

(b) Gauge pressure

(c) Air velocity

(d) Water velocity

Figure 6.14: Plots along the centreline ($y = 0$).

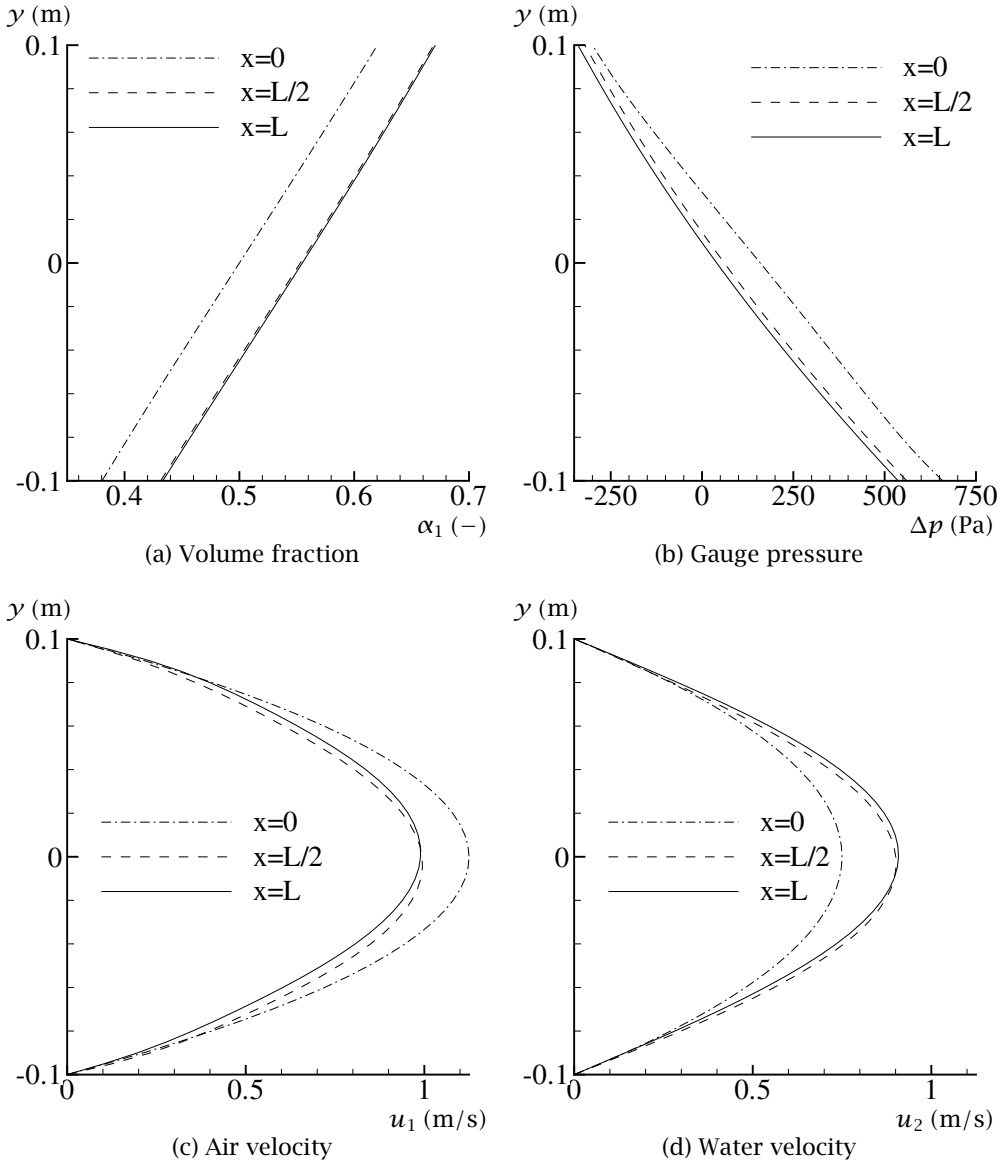

Figure 6.15: Transverse plots for hybrid-sonic flow.

where PI-controllers at the inlet and outlet are used, and for PIO, where the inlet values are set constant and PI-controllers at the outlet are used. The first column shows which variable is compared, the second column shows where the maximum error occurred, and the third the error. For both PIIO and PIO, the largest error observed is in the u_1-velocity for Channel A and C. For PIIO the error is as low as 1.5%, which indeed is an excellent result. For PIO the error is 5.9%, which still is a good result.

In order to find out how much the steady solution differ between PIIO and PIO for Channel C, the error function in this case is presented in Table 6.8. The difference in the air velocity is as low as 1.1%. This shows that the two methods are almost equivalent to compute Channel C, and PIIO gives better results than PIO when computing Channel A and B.

Table 6.6: Comparing Channel A and C in the hybrid-sonic case.

$e(f)$	(i,j)	PIIO	(i,j)	PIO
α_1	(41,5)	$3.1 \cdot 10^{-4}$	(41,30)	$2.1 \cdot 10^{-4}$
p	(1,2)	$6.8 \cdot 10^{-6}$	(2,2)	$1.2 \cdot 10^{-6}$
u_1	(41,2)	$1.5 \cdot 10^{-2}$	(41,38)	$5.9 \cdot 10^{-2}$
u_2	(41,40)	$3.2 \cdot 10^{-3}$	(41,40)	$4.8 \cdot 10^{-3}$

Table 6.7: Comparing Channel B and C in the hybrid-sonic case.

$e(f)$	(i,j)	PIIO	(i,j)	PIO
α_1	(41,2)	$1.4 \cdot 10^{-4}$	(41,2)	$1.9 \cdot 10^{-4}$
p	(1,5)	$2.5 \cdot 10^{-6}$	(1,40)	$4.4 \cdot 10^{-6}$
u_1	(11,2)	$1.3 \cdot 10^{-2}$	(41,37)	$2.2 \cdot 10^{-2}$
u_2	(10,2)	$3.0 \cdot 10^{-3}$	(10,2)	$3.1 \cdot 10^{-3}$

Transient behaviour

In Figure 6.16 and Figure 6.17, the inlet and outlet mass-flow rates for Channel A, B, and C are shown. The mass-flow rates for the PIIO and PIO arrangements are plotted against the reduced time t‘.

Table 6.8: Comparing PIIO and PIO for Channel C in the hybrid-sonic case.

$e(f)$	(i,j)	PIIO-PIO
α_1	(1,2)	$4.6 \cdot 10^{-4}$
p	(1,2)	$8.1 \cdot 10^{-6}$
u_1	(1,40)	$1.1 \cdot 10^{-2}$
u_2	(1,40)	$2.3 \cdot 10^{-3}$

Observations: For Channel B, the inlet mass-flow rate is approximately equal to the outlet mass-flow rate. Note that Channel C needs more time to converge than A and B. This may be due to Channel C having length $2L$ and therefore the imposed information needs more time to travel back and forth, or the controlling parameter K_P for Channel C is half that of Channel A and B. More computations are required to investigate this issue. However, this is left for further work.

Comparison of PIIO and PIO: The arrangements have roughly the same transient variations. PIO reaches the steady solution after $t' \approx 1.5$ and PIIO at $t' \approx 2$. The amplitude of the mass-flow rate for PIO is larger than for PIIO, as can be seen in Figure 6.16(c)-6.16(d) and Figure 6.17(c)-6.17(d).

When a controller is used to set the inlet profile, a deviation between the imposed profile and the actual profile has to exist for the unknown $\mathscr{L}^-$ to be estimated. This can be seen in Figure 6.16(a), where the inlet mass-flow rate for PIIO increases to reach the steady level after $t' = 1.5$. For PIO, where the inlet profile is set, we see that the inlet mass-flow rate remains almost constant.

Conservation of mass: The inlet of Channel B equals the outlet of Channel A, which can be verified in Figure 6.16 and Figure 6.17.

Normally, a scheme which conserve mass, like the RKFV approach which were used for the one-dimensional computations in Section 6.2.2, should be used. A question which arises is whether the RKFD method can be used to study the boundary conditions. In one-dimensional flow, the RKFD and the RKFV-method gave equivalent results. This indicates that the RKFD method

is adequate to study the behaviour of the boundary conditions.

Complex eigenvalues

The problems with complex eigenvalues, as discussed earlier in this chapter were not experienced in the computations. In general this may not be the case. A detailed study of possible problems associated with complex eigenvalues is therefore required. To perform such a study is beside the scope of this thesis.

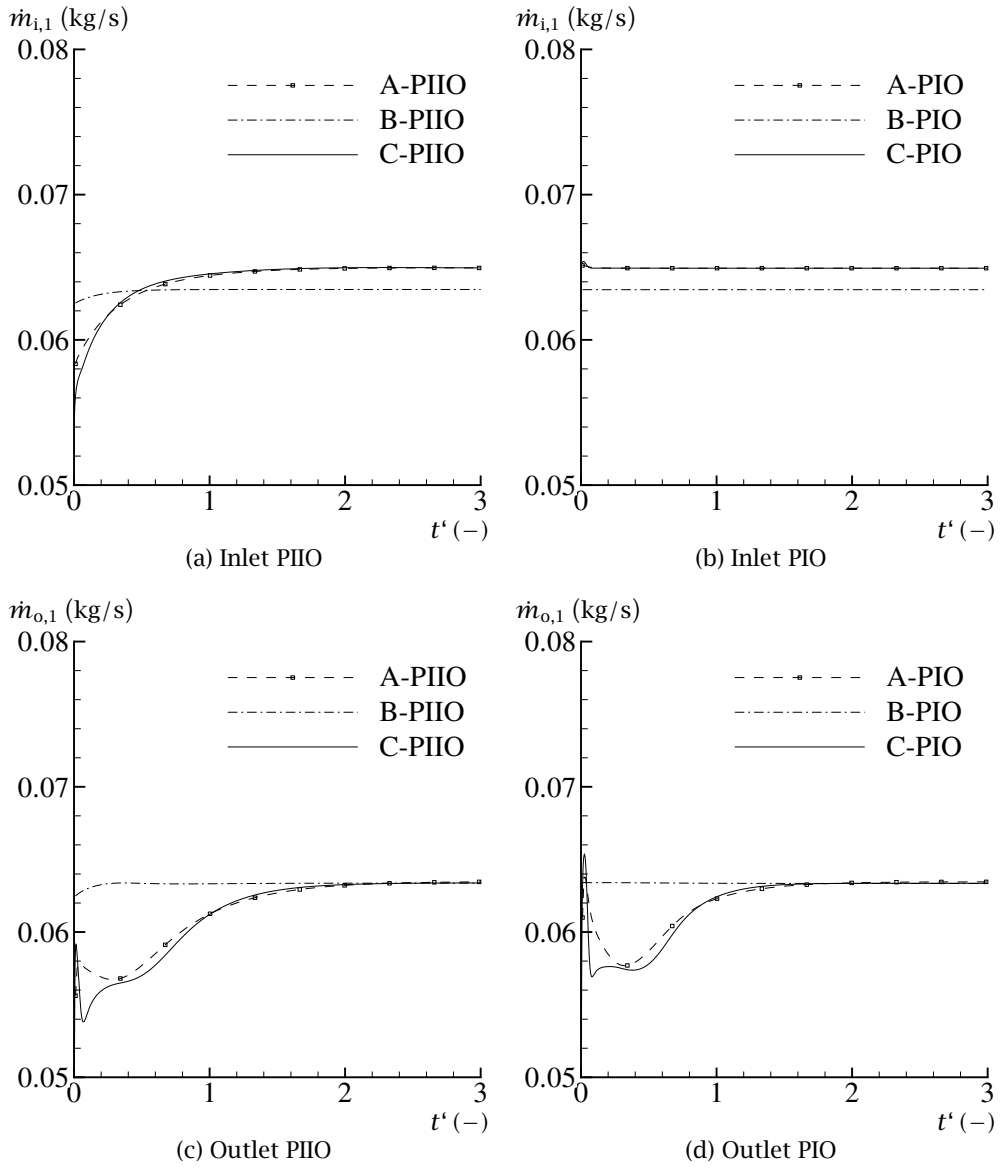

Figure 6.16: Inlet and outlet mass-flow rates of air, phase 1.

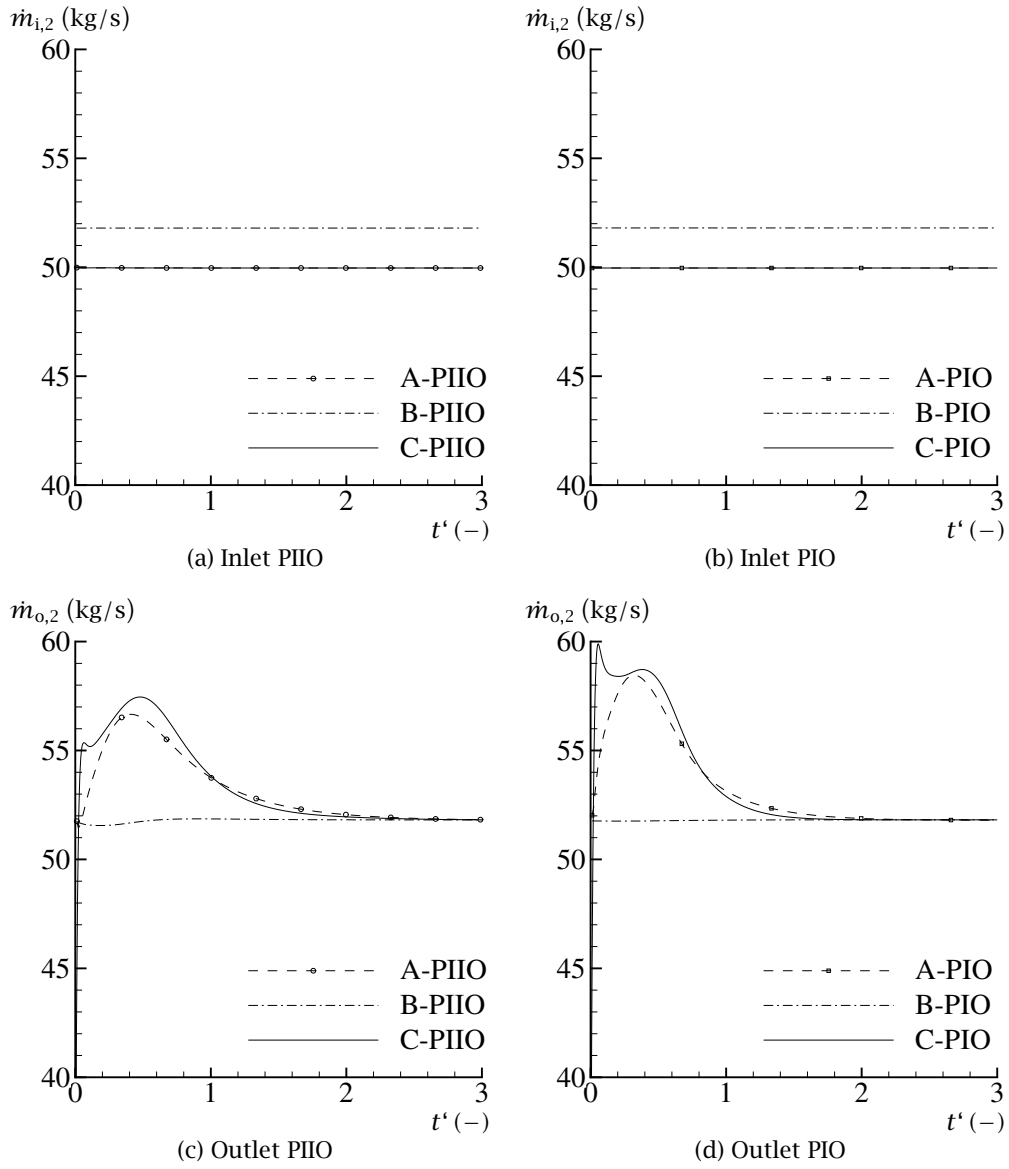

(a) Inlet PIIO

(b) Inlet PIO

(c) Outlet PIIO

(d) Outlet PIO

Figure 6.17: Inlet and outlet mass-flow rates of water, phase 2.

6.4.6 Results from subsonic flow

In this section, results from subsonic flow are presented. The results are presented in the same manner as for hybrid-sonic flow.

The steady solution

In Figures 6.18–6.21, contour plots of the volume fraction, the pressure, the air velocity, and the water velocity for subsonic flow are presented. In Section 6.3, where the sign of the gradients was examined, areas were discovered where the model was unphysical. In the volume-fraction and pressure-contour plot, two unphysical areas can also be seen, one located at the upper wall and $x = 0.05\,\text{m}$, and the other at the lower wall and $x = 0.125\,\text{m}$. Marked with circles in the plots. Observe that the air velocity decreases at the inlet and then increases in the developed section. The water velocity has an opposite behaviour.

This is better seen in the centreline plots in Figure 6.22. In the centreline plot for the pressure, Figure 6.22(b), observe that the pressure falls at the inlet and then increases to top out at $x = 0.15\,\text{m}$, to drop rapidly again and become fully developed around $x = 0.7\,\text{m}$ and that the fully developed pressure gradient is around $43\,\text{Pa/m}$. This is only half the pressure drop observed in hybrid-sonic flow.

These effects can also be seen in the transverse plots given in Figure 6.23. The transverse pressure plot at the inlet, Figure 6.23(b), curves close to the wall and then the pressure drop becomes locally as high as $250\,\text{Pa/m}$. This wall effect is also observed in the air velocity, Figure 6.23(c), where the transverse gradient is larger. This is not observed for the water velocity in Figure 6.23(d).

Comparison of Channel A, B, and C

In Table 6.9, the maximum of the error-function is shown for Channel A and C, and in Table 6.10 for Channel B and C. As for the hybrid-sonic flow, the error was smaller for PIIO than for PIO. The largest error occurred for the air velocity, when comparing Channel A and C: 4.8% for PIO and 1.4% for PIIO.

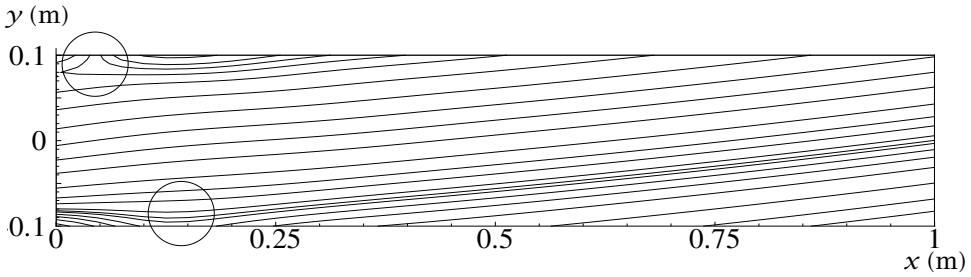

Figure 6.18: Contour plot of the volume fraction.

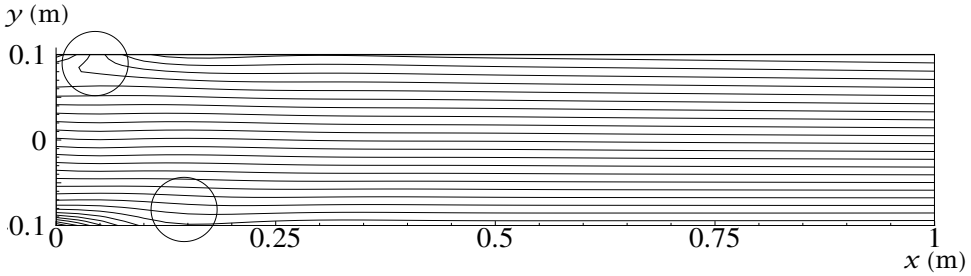

Figure 6.19: Contour plot of the pressure.

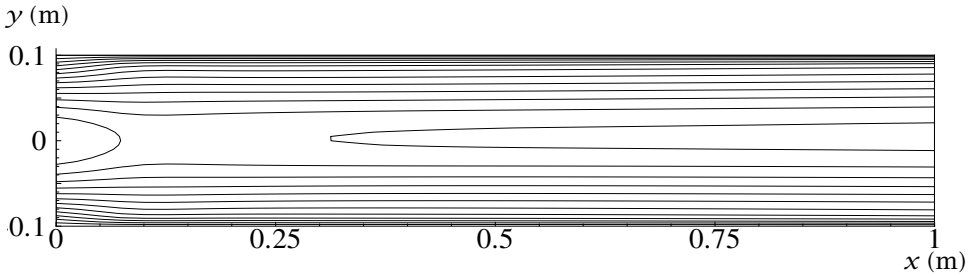

Figure 6.20: Contour plot of the air velocity.

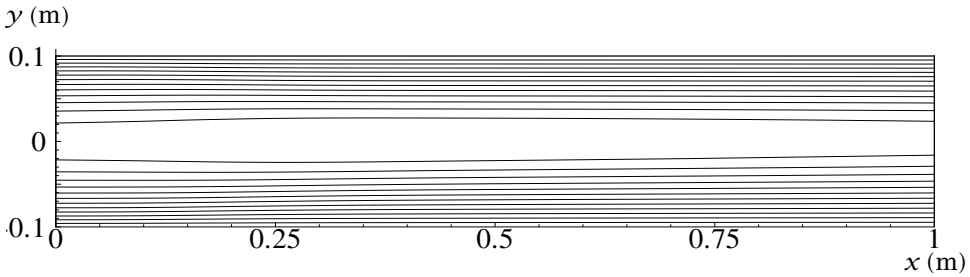

Figure 6.21: Contour plot of the water velocity.

The difference in the steady solution, for Channel C between the two arrangements is shown in Table 6.11, and it can be seen that they give almost the same solution. The largest difference, 6.1%, occurs in the water velocity.

Table 6.9: Comparing Channel A and C in the subsonic case.

$e(f)$	(i,j)	PIIO	(i,j)	PIO
α_1	(1,2)	$4.1 \cdot 10^{-4}$	(36,2)	$1.1 \cdot 10^{-4}$
p	(1,2)	$3.5 \cdot 10^{-5}$	(41,31)	$1.6 \cdot 10^{-4}$
u_1	(41,40)	$1.4 \cdot 10^{-2}$	(41,39)	$4.8 \cdot 10^{-2}$
u_2	(41,2)	$4.6 \cdot 10^{-3}$	(41,2)	$6.9 \cdot 10^{-3}$

Table 6.10: Comparing Channel B and C in the subsonic case.

$e(f)$	(i,j)	PIIO	(i,j)	PIO
α_1	(1,2)	$1.1 \cdot 10^{-3}$	(1,2)	$2.2 \cdot 10^{-3}$
p	(1,34)	$3.5 \cdot 10^{-5}$	(2,2)	$6.3 \cdot 10^{-5}$
u_1	(2,40)	$1.3 \cdot 10^{-2}$	(2,2)	$2.6 \cdot 10^{-2}$
u_2	(41,2)	$1.5 \cdot 10^{-2}$	(41,2)	$1.5 \cdot 10^{-2}$

Transient behaviour

In Figure 6.24 and Figure 6.25, the inlet and outlet mass-flow rates for Channel A, B, and C are shown. The mass-flow rates for the PIIO and PIO arrange-

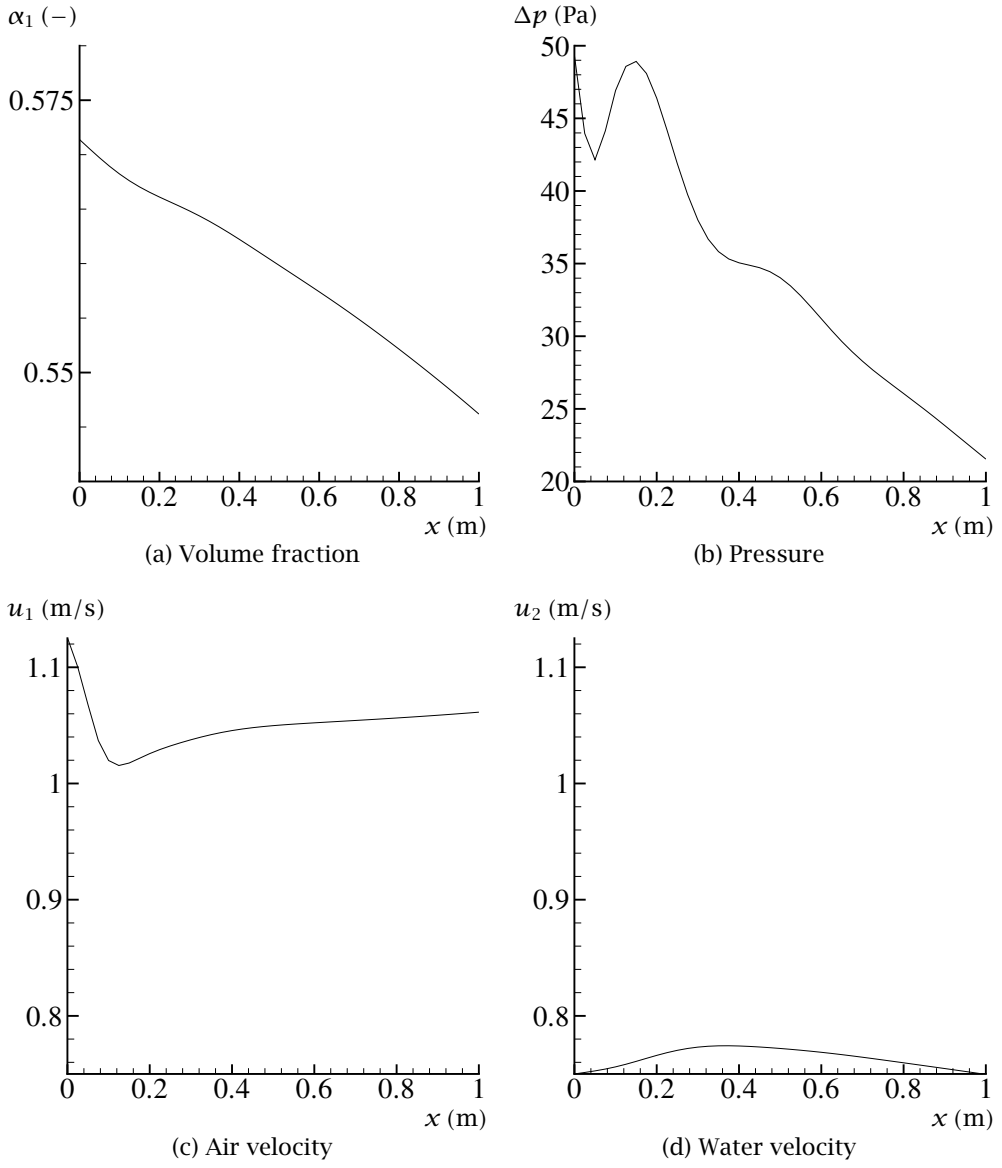

(a) Volume fraction

(b) Pressure

(c) Air velocity

(d) Water velocity

Figure 6.22: Plots along the centreline ($y = 0$).

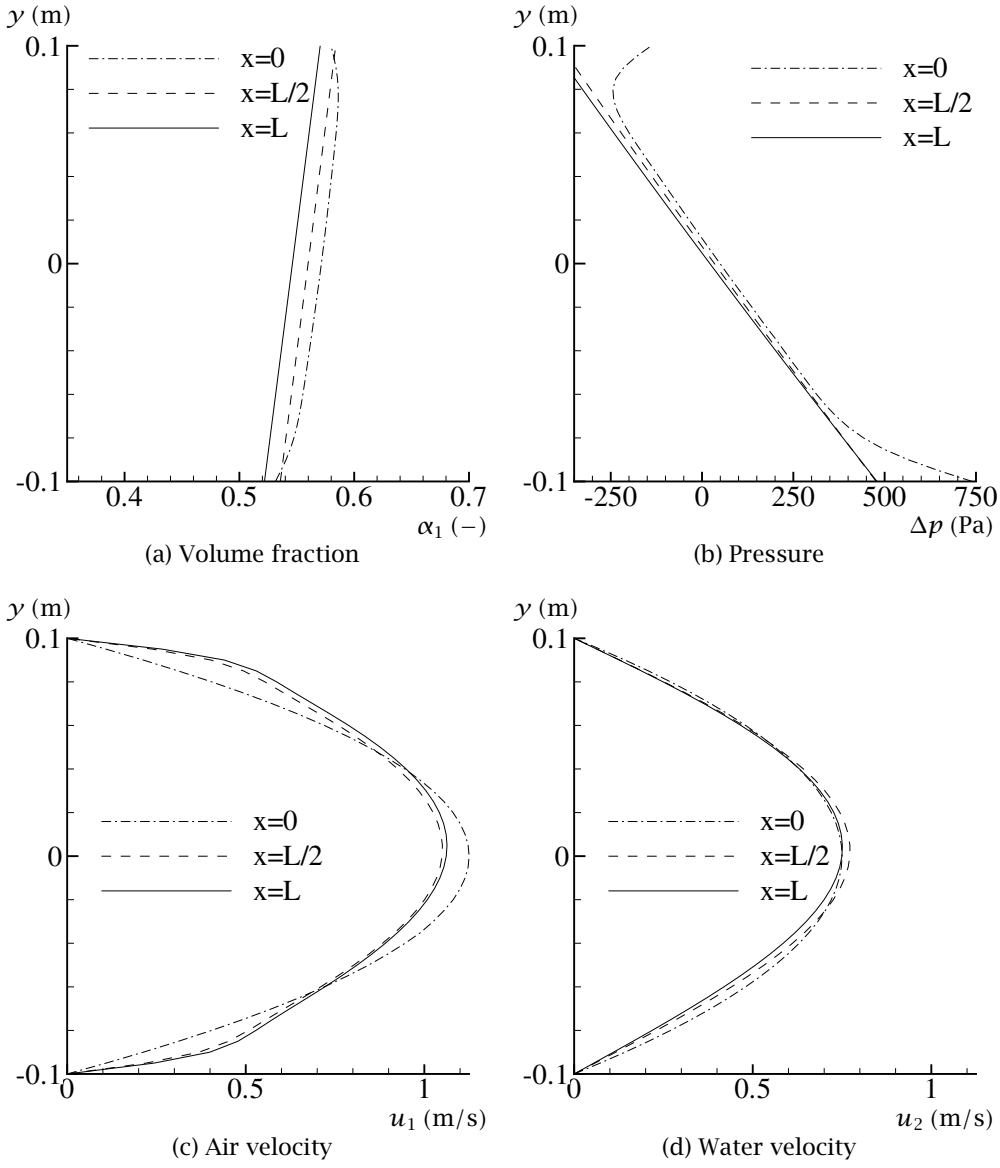

(a) Volume fraction

(b) Pressure

(c) Air velocity

(d) Water velocity

Figure 6.23: Transverse plots for subsonic flow.

Table 6.11: Comparing PIIO and PIO for Channel C in the subsonic case.

$e(f)$	(i,j)	PIIO-PIO
α_1	(1,2)	$3.0 \cdot 10^{-2}$
p	(1,2)	$1.7 \cdot 10^{-3}$
u_1	(79,40)	$1.1 \cdot 10^{-2}$
u_2	(5,40)	$6.1 \cdot 10^{-2}$

ment are plotted against the reduced time t‘.

First observe that the converged mass-flow rates are approximately the same for all three channels and the deviation between the channels is much smaller for subsonic flow than for hybrid-sonic flow.

Channel A converges faster than C, and the steady solution was reached at $t' \approx 0.4$ for PIO, as can be seen in Figure 6.24(b) and Figure 6.25(b). For the water, the amplitude of the mass-flow rate at the outlet, Figure 6.25(c) and Figure 6.25(d), is larger for PIO than PIIO.

The inlet and outlet mass-flow rate for the air, phase 1 in Figure 6.24, increases at the beginning for all arrangements, while they decrease after an initial peak for the water phase, phase 2 in Figure 6.25.

In both arrangements, a small fluctuation occurs in the outlet mass-flow rate, at $t' \approx 1$ for PIIO and at $t' \approx 0.7$ for PIO. This can be due to disturbances generated at the inlet at the startup of the computation.

6.4.7 Comparison of the results from hybrid-sonic and subsonic flow

When the B_k-parameter for the interface pressure was chosen, it was not the intention to compare the solutions between hybrid-sonic and subsonic flow. It was to evaluate the boundary conditions for an example hybrid-sonic and example subsonic flow. For comparison purposes, it is therefore probably better to compare when the interface pressure parameter $B_{k,y}$ is equal for both cases, since this will give approximately the same separation profile. Still, a comparison of the solutions can be made.

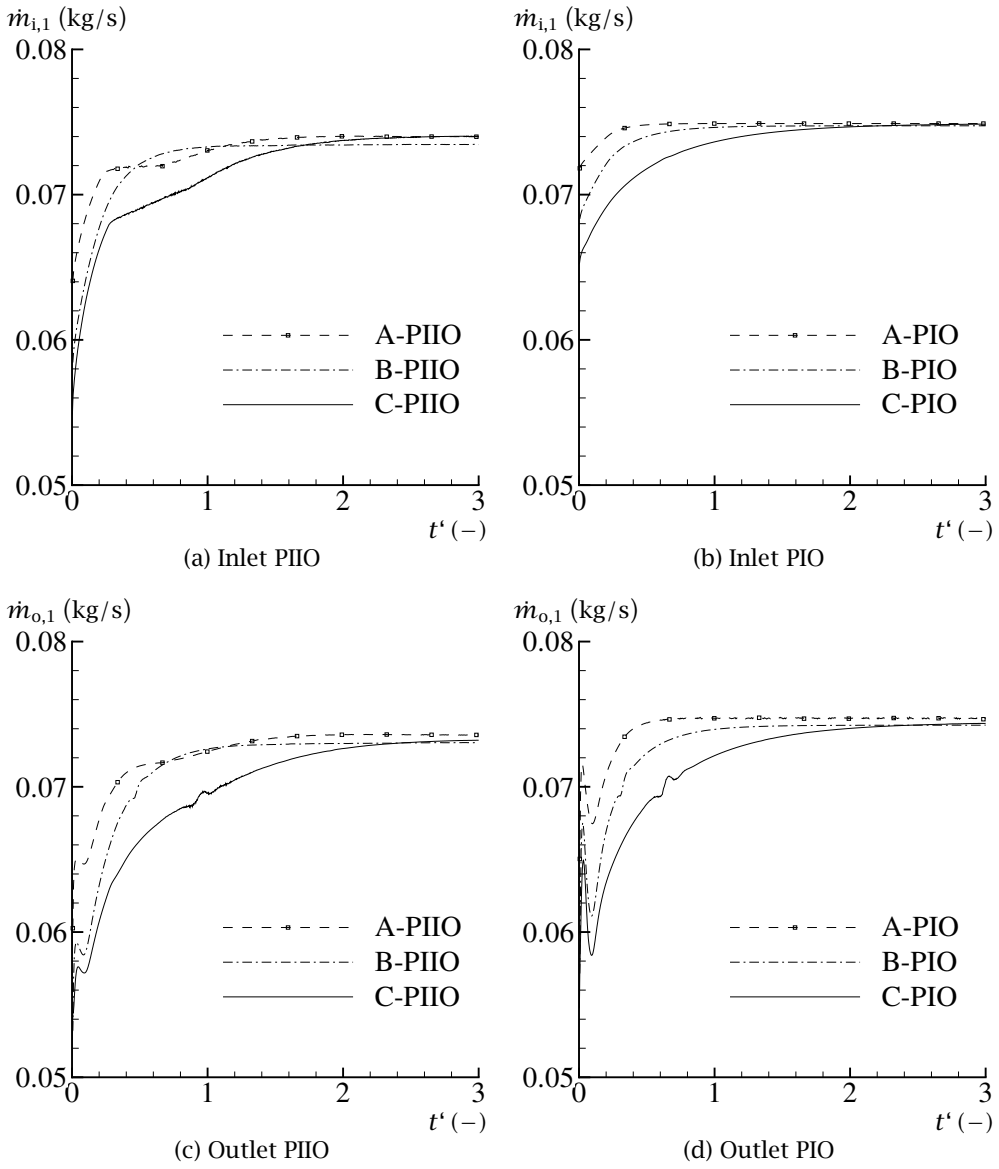

(a) Inlet PIIO (b) Inlet PIO

(c) Outlet PIIO (d) Outlet PIO

Figure 6.24: Inlet and outlet mass-flow rates of air, phase 1.

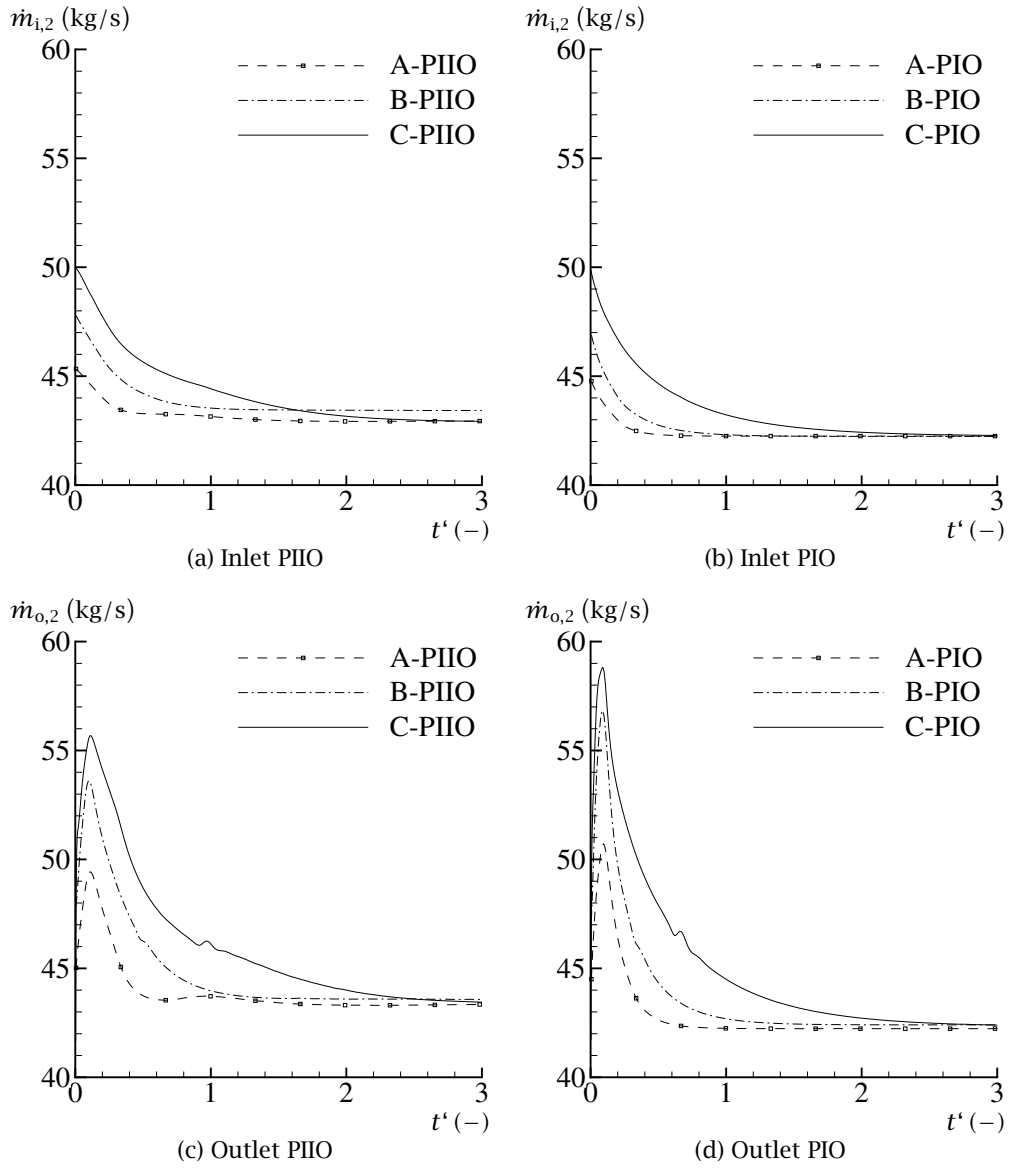

(a) Inlet PIIO (b) Inlet PIO

(c) Outlet PIIO (d) Outlet PIO

Figure 6.25: Inlet and outlet mass-flow rates of water, phase 2.

The steady solution

The steady solution for hybrid-sonic flow is smooth, as seen in the contour and centreline plots. On the contrary, the steady solution for subsonic flow seems to have several artifacts. To repeat, two artificial points are observed in Figure 6.18 and Figure 6.19. The water velocity is hardly affected, Figure 6.22(d), the air velocity, Figure 6.22(c), has a rather large positive gradient in the developed section. The decrease, and the increase in the pressure in Figure 6.22(b) is also artificial. It makes sense, though, that the pressure drop is higher at the bottom of the channel, where there are more water. However, a pressure drop as seen at $y = 0.1$ m in Figure 6.23(b), is hard to justify.

Although the results have not been compared with experiments, the hybrid-sonic solution seems to be the best solution.

The error-function and boundary arrangements

The boundary-condition test gave equivalent results for both cases. The largest error was observed for PIO, 4.8% for subsonic flow and 5.9% for hybrid-sonic flow, when Channel A and C are compared.

When PIO and PIIO are compared, the maximum difference for u_1 was equal, 1.1%. However, the difference between the PIIO- and PIO-solution was higher for the other variables in the subsonic case. From 0.23% in the hybrid-sonic case to 6.1% in the subsonic case, when u_2 is compared.

Despite the difference, it may be concluded that the boundary conditions worked well for the hybrid-sonic and subsonic flow presented here.

The transient solution

The first thing to note when comparing the transient solution for the two cases, is that the air mass-flow rate is higher in the subsonic case than in the hybrid-sonic case, while the water mass-flow rate has an opposite difference.

Second, that the air mass-flow rate for PIO in the subsonic case increases in the beginning, while it remains almost constant in the hybrid-sonic case. The reason for this is probably that, $B_k = 0.9$ results in a force along the

channel in the subsonic case. This results in a reduction of the water mass-flow rate and an increase of the air mass-flow rate.

Third, the steady solution was obtained after $t' \approx 1.5$ in the hybrid-sonic case, while in the subsonic case, the steady solution came after $t' \approx 2.5$.

6.5 Summary

In this chapter, multiphase flow has been computed. The eigenvalues have been examined for some example configurations, and it is found that two of the eigenvalues are small compared to the phasic speed of sound. In some cases, the inviscid model possessed complex eigenvalues, which may lead to an ill-posed inviscid model.

Perfectly non-reflecting boundary conditions were tested for a one-dimensional shock-tube, and the results were excellent.

A tube with an inlet and an outlet has been computed with reflecting boundary conditions. Parameter areas where the model predicted increasing pressure were discovered. This lead to an investigation where these areas were mapped. By solving the steady one-dimensional model, it was shown that the steady solution found in the transient case indeed was the steady solution. It is therefore concluded that the boundary conditions worked well.

Two-dimensional flow in a horizontal channel has been studied for hybrid-sonic flow and for subsonic flow. Each flow was computed with the PIIO and PIO setup for the boundary conditions. Both setups gave satisfactory results when the boundary conditions were evaluated. PIIO was the setup which gave the lowest error in the boundary test and the smoothest transient behaviour.PIO converged fastest to the steady solution.

The solution obtained in the subsonic case had several artifacts. Without further studies which justify the solution, subsonic flow is not recommended for further use. Anyhow, the boundary conditions worked well in this case.

Chapter 7

Concluding remarks and recommendations

Time-dependent boundary conditions for multiphase flow have been proposed. Characteristic-based boundary conditions have been reviewed for single-phase flow. Methods for avoiding a drifting pressure have been analysed and control functions have been used to estimate the incoming wave amplitudes.

7.1 Concluding remarks

The use of control functions to estimate the incoming wave amplitudes has been tested and verified for single-phase and multiphase flow.

Particularly, P- and PI-controllers have been tested. The controllers have been applied for the estimation of the incomning wave amplitudes at the inlet and at the outlet. When the start term for the controller was zero, the P-controller gave the best convergence. Unfortunately, an imposed value could not be specified with the P-controller. With the PI-controller, a given value could be imposed. Based on this, the PI-controller is preferred. When the PI-controller was used to set the inlet as well as the outlet, better performance results where observed, although the convergence was not improved. In the case where the inlet values are set directly, equally good results were obtained as when a controller was used. Therefore, to set the inlet values directly may in many cases be the best choice.

The modelling of multiphase flow has been reviewed. In the case of separation by gravity, it is shown that the interface pressure can not be equal to the pressure. The study showed that if the interface pressure was a bit lower than the pressure, it could predict separation by gravity.

In the one-dimensional computations, it is shown that the steady solution is obtained with the transient solver. Even with complex eigenvalues, a solution of the governing equation was found. Areas where the constant B_k-model predicts unphysically flow were shown. When the interface pressure is equal to the pressure ($B_k = 1$), singular points are reduced to the case where the velocities are zero. It is therefore, preferable to set the interface pressure equal to the pressure whenever possible with the present model.

A subsonic and a hybrid-sonic flow have been computed in a horizontal channel for liquid velocities around 1 m/s and gas velocites around 1.5 m/s. In both cases, the boundary conditions work well. The subsonic solution had several artifacts which could not be explained on a physical basis. Since the hybrid-sonic solution did not have these artifacts, hybrid-sonic flow is recommended for further study.

7.2 Recommendations for further work

- A study which determines optimal values for the parameters in the PID-controller should be carried out, and other control functions should be tested.
- Better methods to evaluate the transient behaviour should be developed.
- A proper filter for the RKFV-method should be implemented.
- An investigation of how the boundary conditions perform when the flow is non-perpendicular to the outlet is recommended.
- An investigation which determines the best way to handle corners should be carried out.
- Model work should be done so that an inclined channel can be computed, without having a transition from hybrid-sonic to subsonic flow.

Bibliography

The bibliography is sorted alphabetically by the author. If there are more than one author, it is sorted by the first author.

Abarnel, S., Gottlieb, D., and Hesthaven, J. Well-posed perfectly matched layers for advective acoustics. *Journal of Computational Physics*, volume 154: pages 266–283, 1999.

Baum, M., Poinsot, T., and Thévenin, D. Accurate boundary conditions for multicomponent reactive flows. *Journal of Computational Physics*, volume 116: pages 247–261, 1994.

Bedjaoui, N. and Sainsaulieu, L. Analysis of a non-hyperbolic system modeling two-phase flows part 1: The effects of diffusion and relaxation. *Mathematical Methods in the Applied Sciences*, volume 20: pages 783–803, 1997.

Bendiksen, K. H., Malnes, D., Moe, R., and Nuland, S. The dynamic two-fluid model OLGA: Theory and application. *SPE Production Engineering*, pages 171–179, May 1991.

Bjørhus, M. The ODE formulation of hyperbolic PDEs discretized by the spectral collocation method. *SIAM Journal on Scientific Computing*, volume 16: pages 542–557, 1995. ISSN 1064-8275.

Bruneau, C. H. and Creusé, E. Towards a transparent boundary condition for compressible navier-stokes equations. *International Journal for Numerical Methods in Fluids*, volume 36: pages 807–840, 2001.

Caiden, R., Fedkiw, R. P., and Anderson, C. A numerical method for two-phase flow consisting of separate compressible and incompressible regions. *Journal of Computational Physics*, volume 166: pages 1–27, 2001.

Carpenter, M. and Kennedy, C. Fourth-order 2n-storage runge-kutta schemes. Technical Report NASA TM-109112, Langley Research Center, Hampton, VA, 1994.

Chaturvedi, R. Studies of non reflecting boundary conditions and their applications. Doctor of philosophy, Indian Institute of Technology, Bombay, 1999.

Cheng, B. L., Glimm, J., Saltz, D., and Sharp, D. H. Boundary conditions for a two pressure two-phase flow model. *Physica D. Nonlinear Phenomena*, volume 133, no. 1-4: pages 84–105, 1999. ISSN 0167-2789. Predictability: quantifying uncertainty in models of complex phenomena (Los Alamos, NM, 1998).

Chung, M. S., Chang, K. S., and Lee, S. J. Wave propagation in two-phase flow based on a new hyperbolic two-fluid model. *Numerical Heat Transfer, Part A Applications*, volume 38: pages 169–91, 2000.

Chung, M. S., Chang, K. S., and Lee, S. J. Numerical solution of hyperbolic two-fluid two-phase flow model with non-reflecting boundary conditions. *International Journal of Engineering Science*, volume 40: pages 789–803, 2002.

Colonius, T. and Ran, H. A super-grid-scale model for simulating compressible flow on unbounded domains. *Journal of Computational Physics*, volume 182: pages 191–212, 2002.

Cortes, J., Debussche, A., and Toumi, I. A density pertubation method to study the eigenstructure of two-phase flow equation systems. *Journal of Computational Physics*, volume 147: pages 463–484, 1998.

Dinh, T., Nourgaliev, R., and Theofanous, T. Understanding the ill-posed two-fluid model. In: *The 10th international topical meeting on nuclear reactor thermal hydraulics*. Seuol, Korea, October 2003.

Drew, D. A. and Passman, S. L. *Theory of multicomponent fluids*, volume 135 of *Applied Mathematical Sciences*. Springer-Verlag, New York, 1999. ISBN 0-387-98380-5.

Engquist, B. and Majda, A. Absorbing boundary conditions for the numerical simulation of waves. *Mathematics of Computation*, volume 31, no. 139: pages 629–651, 1977.

Engquist, B. and Majda, A. Radiation boundary conditions for acoustic and elastic wave calculations. *Communications on Pure and Applied Mathematics*, volume 32: pages 313–357, 1979.

Evje, S. and Fjelde, K. K. On a rough AUSM scheme for a one-dimensional two-phase model. *Computers & Fluids*, volume 32: pages 1497–530, 2003.

Givoli, D. Nonreflecting boundary conditions. *Journal of Computational Physics*, volume 94, no. 1: pages 1–29, 1991. ISSN 0021-9991.

Givoli, D. A spatially exact nonreflecting boundary condition for time dependent problems. *Comput. Methods Appl. Mech. Engrg.*, volume 95, no. 1: pages 97–113, 1992. ISSN 0045-7825.

Givoli, D. and Patlashenko, I. Optimal local non-reflecting boundary conditions. *Applied Numerical Mathematics*, volume 27, no. 4: pages 367–384, 1998. ISSN 0168-9274. Absorbing boundary conditions.

Gran, I. R. Personal communication, 2000.

Haley, T. C., Lahey, R. T., and Drew, D. A. A characteristic analysis of void waves using two-fluid models. *Nuclear Engineering and Design*, volume 139: pages 45–47, 1993.

Harlow, F. H. and Amsden, A. A. Numerical fluid dynamics calculation method for all flow speeds. *Journal of Computational Physics*, volume 8, no. 2: page 197, 1971.

Haugen, F. *Regulering av dynamiske systemer*. TAPIR FORLAG, Trondheim, 1994. ISBN 82-519-1433-7.

Hirsch, C. *Numerical computation of internal and external flows*, volume 1 of *Fundamentals of Numerical Discretization*. John Wiley & Sons, Chichester, 1988. ISBN 0-471-92385-0.

Hu, F. Q. A stable, perfectly matched layer for linearized Euler equations in unsplit physical variables. *Journal of Computational Physics*, volume 173: pages 455–80, 2001.

Hwang, Y.-H. Upwind scheme for non-hyperbolic systems. *Journal of Computational Physics*, volume 192: pages 643–676, 2003.

Ishii, M. *Thermo-fluid dynamic theory of two-phase flow*. Collection de la Direction des Etudes et Recherches d'Electricité de France. Eyrolles, Paris, 1975.

Kataoka, I., Besnard, D. C., and Serizawa, A. Basic equation of turbulence and modeling of interfacial transfer terms in gas-liquid two-phase flow. *Chemical Engineering Communications*, volume 118: pages 221–236, 1992.

Kataoka, I. and Serizawa, A. Basic equations of turbulence in gas-liquid two-phase flow. *International Journal of Multiphase Flow*, volume 15, no. 5: pages 843–855, 1989.

Keller, J. B. and Givoli, D. Exact nonreflecting boundary conditions. *Journal of Computational Physics*, volume 82, no. 1: pages 172–192, 1989. ISSN 0021-9991.

Kennedy, C. A. and Carpenter, M. H. Several new numerical methods for compressible shear-layer simulations. *Applied Numerical Mathematics*, volume 14: pages 397–433, 1994.

Kennedy, C. A. and Carpenter, M. H. Comparison of several numerical methods for simulation of compressible shear layers. Technical Report NASA Technical Paper 3484, National Aeronautics and Space Administration Langley Research Center - Hampton, Virginia 23681-2199, 1997.

Kim, J. W. and Lee, D. J. Generalized characteristic boundary conditions for computational aeroacoustics. *AIAA Journal*, volume 38, no. 11: pages 2040–2049, 2000.

Lee, S. J., Chang, K. S., and Kim, S. J. Surface tension effect in the two-fluids equation system. *International Journal of Heat and Mass Transfer*, volume 41: pages 2821–6, 1998.

Lee, W. H. and Lyczkowski, R. W. The basic character of five two-phase flow model equation sets. *International Journal for Numerical Methods in Fluids*, volume 33: pages 1075–1098, 2000.

Leveque, R. J. *Finite volume methods for hyperbolic problems*. Cambridge texts in applied Mathematics, 2002. ISBN 0-521-81087-6.

Mathew, J., Lechner, R., Foysi, H., Sesterhenn, J., and Friedrich, R. An explicit filtering method for large eddy simulation of compressible flows. *Physics of Fluids*, volume 15: pages 2279–89, 2003.

Melaaen, M. C. Analysis of curvilinear non-orthogonal coordinates for numerical calculation of fluid flow in complex geometries. Dr. ing. thesis, University of Trondheim, 1990.

Melaaen, M. C. Calculation of fluid flows with staggered and nonstaggered curvilinear nonorthogonal grids–a comparison. *Numerical Heat Transfer*, volume 21: pages 21–39, 1992a.

Melaaen, M. C. Calculation of fluid flows with staggered and nonstaggered curvilinear nonorthogonal grids–the theory. *Numerical Heat Transfer, Part B*, volume 21: pages 1–19, 1992b.

Moe, R. and Bendiksen, K. H. Transient simulation of 2D and 3D stratified and intermittent two-phase flows. Part I: Theory. *International Journal for Numerical Methods in Fluids*, volume 16: pages 461–487, 1993.

Moura, L. F. M. and Rezkallah, K. S. Numerical study on the two-phase flow distribution in a T-junction. *International Journal for Numerical Methods in Fluids*, volume 17: pages 257–270, 1993.

Munkejord, S. T., Mølnvik, M. J., Melheim, J. A., Gran, I. R., and Olsen, R. Development of a 2D multiphase simulator and validation for high-pressure pipe flows. *Submitted to Applied Mathematical Modelling*, 2003.

Nguyen, D. L., Winter, E. R. F., and Greiner, M. Sonic velocity in two-phase systems. *International Journal of Multiphase Flow*, volume 7: pages 311–20, 1981.

Nigmatulin, R. I. *Dynamics of Multiphase Media*, volume 1. Hemisphere Publishing Corporation, New York, 1991. ISBN 0-89116-316-6.

Nourgaliev, R., Dinh, N., and Theofanous, T. A characteristics-based approach to the numerical solution of the two-fluid model. In: *4th*

ASME/JSME joint fluids engineering conference, volume FEDSM2003-45551. July 2003a.

Nourgaliev, R., Dinh, N., and Theofanous, T. The characteristics-based matching (CBM) method for compressible flow with moving boundaries and interfaces. In: *4th ASME/JSME joint fluids engineering conference*, volume FEDSM2003-45550. July 2003b.

Okong'o, N. and Bellan, J. Consistent boundary conditions for multicomponent real gas mixtures based on characteristic waves. *Journal of Computational Physics*, volume 176: pages 330–344, 2002.

Patankar, S. V. *Numerical Heat Transfer and Fluid Flow*. McGraw-Hill Book Company, New York, 1980.

Patankar, S. V. and Spalding, D. B. Calculation procedure for heat, mass and momentum-transfer in 3-dimensional parabolic flows. *International Journal of Heat and Mass Transfer*, volume 15, no. 10: page 1797, 1972.

Peric, M. A finite volume method for the prediction of three-dimensional fluid flow in complex ducts. Ph.D. thesis, Imperial College, London, 1985.

Poinsot, T. J. and Lele, S. K. Boundary conditions for direct simulations of compressible viscous flows. *Journal of Computational Physics*, volume 101: pages 104–129, 1992.

Prosperetti, A. and Jones, A. V. Pressure forces in disperse two-phase flow. *International Journal of Multiphase Flow*, volume 10, no. 4: pages 425–440, 1984.

Ramshaw, J. D. and Trapp, J. A. Characteristics, stability, and short-wavelength phenomena in two-phase flow equation systems. *Nuclear Science and Engineering*, volume 66: pages 93–102, 1978.

Rhie, C. M. and Chow, W. L. Numerical study of the turbulent flow past an airfoil with trailing edge separation. *AIAA Journal*, volume 21: pages 1525–1532, 1983.

Rian, K. E. On open boundaries in numerical simulations of compressible flows. Technical Report A5048, SINTEF Energy Research, Division of Thermal Energy, Trondheim, Norway, oct 1999.

Rian, K. E. On mathematical modelling and numerical simulation of transient compressible flow across open boundaries. Dr. Ing. thesis, NTNU, Norwegian University of Science and Technology, Norway, 2003.

Rudy, D. H. and Strikwerda, J. C. A nonreflecting outflow boundary condition for subsonic Navier-Stokes calculations. *Journal of Computational Physics*, volume 36: pages 55–70, 1980.

Rudy, D. H. and Strikwerda, J. C. Boundary conditions for subsonic compressible Navier-Stokes calculations. *Computers & Fluids*, volume 9: pages 327–338, 1981.

Ryaben'kii, V. Nonreflecting time-dependent boundary conditions on artificial boundaries of varying location and shape. In: *Proceedings of the Fourth International Conference on Spectral and High Order Methods (ICOSAHOM 1998) (Herzliya)*, volume 33, pages 481–492. 2000. ISSN 0168-9274.

Ryaben'kii, V., Tsynkov, S., and Turchaninov, V. Global discrete artificial boundary conditions for time-dependent wave propagation. Technical report, NASA, 2001.

Salvesen, H.-C. and Teigland, R. Non-reflecting boundary conditions applicable to general purpose CFD simulators. *International Journal for Numerical Methods in Fluids*, volume 28: pages 523–540, 1998.

Saurel, R. and Abgrall, R. A multiphase Godunov method for compressible multifluid and multiphase flow. *Journal of Computational Physics*, volume 150: pages 425–467, apr 1999a.

Saurel, R. and Abgrall, R. A simple method for compressible multifluid flows. *SIAM Journal on Scientific Computing*, volume 21, no. 3: pages 1115–1145 (electronic), 1999b. ISSN 1095-7197.

Saurel, R. and LeMetayer, O. A multiphase model for compressible flows with interfaces, shocks, detonation waves and cavitation. *Journal of Fluid Mechanics*, volume 431: pages 239–271, mar 2001.

Slattery, J. C. Flow of viscoelastic fluids through porous media. *AIChE Journal*, volume 13, no. 6: pages 1066–1071, November 1967.

Soo, S. L. *Particulates and continuum: Multiphase fluid dynamics*. Hemisphere, New York, 1989. ISBN 0-89116-918-0.

Soo, S. L. *Multiphase fluid dynamics*. Science Press, Beijing, 1990. ISBN 0-291-39781-6, 70-300-0102.

Spedding, P. L. and Spence, D. R. Flow regimes in two-phase gas-liquid flow. *International Journal of Multiphase Flow*, volume 19, no. 2: pages 245–280, 1993.

Strikwerda, J. C. *Finite Difference Schemes and Partial Differential Equations*. Wadsworth & Brooks/Cole Advanced Books & Software, 1989.

Sutherland, J. C. and Kennedy, C. A. Improved boundary conditions for viscous, reacting, compressible flows. *Journal of Computational Physics*, volume 191: pages 502–524, July 2003.

Taitel, Y. Multiphase flow modeling, fundamentals and application to oil production system. Course manual, Department of Petroleum Technology and Applied Geophysics, NTNU, 2003.

Thompson, K. W. Time-dependent boundary conditions for hyperbolic systems. *Journal of Computational Physics*, volume 68, no. 1: pages 1–24, 1987. ISSN 0021-9991.

Thompson, K. W. Time-dependent boundary conditions for hyperbolic systems. II. *Journal of Computational Physics*, volume 89, no. 2: pages 439–461, 1990. ISSN 0021-9991.

Tourrette, L. Artificial boundary conditions for the linearized compressible Navier-Stokes equations. *Journal of Computational Physics*, volume 137, no. 1: pages 1–37, 1997. ISSN 0021-9991.

Tourrette, L. Artificial boundary conditions for the linearized compressible Navier-Stokes equations. II. The discrete approach. *Journal of Computational Physics*, volume 144, no. 1: pages 151–179, 1998. ISSN 0021-9991.

Tsynkov, S., Abarbanel, S., Nordstrain, J., Ryaben'kii, V., and Vatsa, V. Global artificial boundary conditions for computation of external flows with jets. *AIAA Journal*, volume 38: pages 2014–22, 2000.

Tsynkov, S. V. Numerical solution of problems on unbounded domains. *Applied Numerical Mathematics*, volume 27: pages 465–532, 1998.

Wesseling, P. *Principles of computational fluid dynamics*. Springer-Verlag, Berlin, 2001. ISBN 3-540-67853-0.

Whitaker, S. Advances in theory of fluid motion in porous media. *Industrial and Engineering Chemistry*, volume 61, no. 4: pages 14–28, December 1969.

Yost, S. A., Rao, P., and Brown, R. M. Absorbing boundary technique for open channel flows. *International Journal for Numerical Methods in Fluids*, volume 33: pages 641–656, 2000.

Appendix A

Two-phase equations extended to three dimensions

In this appendix, the extension of the boundary formulation with arbitrary equation of state to three dimensions is presented. With the conservative and primitive vector as

$$\hat{\boldsymbol{U}} = \begin{bmatrix} \hat{\boldsymbol{U}}_{1\mathrm{D}} \\ \alpha_1\rho_1 v_1 \\ \alpha_2\rho_2 v_2 \\ \alpha_1\rho_1 w_1 \\ \alpha_2\rho_2 w_2 \end{bmatrix}, \quad \boldsymbol{U} = \begin{bmatrix} \boldsymbol{U}_{1\mathrm{D}} \\ v_1 \\ v_2 \\ w_1 \\ w_2 \end{bmatrix}, \tag{A.1}$$

where the index $_{1\mathrm{D}}$ is meant to identify a corresponding entity in one dimension. As an example $\boldsymbol{U}_{1\mathrm{D}}$, is the $\boldsymbol{U}$-vector in the one-dimensional case. The transformation matrix $\boldsymbol{P}$ and system matrix $\boldsymbol{A}$ in three dimensions are

$$\boldsymbol{P} = \begin{bmatrix} \boldsymbol{P}_{1\mathrm{D}} & & & & & & & \\ \rho_1 v_1 & \alpha_1 v_1 \frac{\partial \rho_1}{\partial P} & 0 & 0 & \alpha_1\rho_1 & 0 & 0 & 0 \\ -\rho_2 v_2 & \alpha_2 v_2 \frac{\partial \rho_2}{\partial P} & 0 & 0 & 0 & \alpha_2\rho_2 & 0 & 0 \\ \rho_1 w_1 & \alpha_1 w_1 \frac{\partial \rho_1}{\partial P} & 0 & 0 & 0 & 0 & \alpha_1\rho_1 & 0 \\ -\rho_2 w_2 & \alpha_2 w_2 \frac{\partial \rho_2}{\partial P} & 0 & 0 & 0 & 0 & 0 & \alpha_2\rho_2 \end{bmatrix}, \tag{A.2}$$

and

$$\boldsymbol{A} = \begin{bmatrix} \boldsymbol{A}_{1\mathrm{D}} & & & & \\ 0 & u_1 & 0 & 0 & 0 \\ 0 & 0 & u_2 & 0 & 0 \\ 0 & 0 & 0 & u_1 & 0 \\ 0 & 0 & 0 & 0 & u_2 \end{bmatrix}. \tag{A.3}$$

The eigenvalues of $\boldsymbol{A}$ will now be the eigenvalues of $\boldsymbol{A}_{1D}$ and $[u_1, u_2, u_1, u_2]$. The eigenvector matrix and its inverse are:

$$\boldsymbol{S} = \begin{bmatrix} \boldsymbol{S}_{1D} & 0 \\ 0 & \boldsymbol{I} \end{bmatrix}, \quad \boldsymbol{S}^{-1} = \begin{bmatrix} \boldsymbol{S}_{1D}^{-1} & 0 \\ 0 & \boldsymbol{I} \end{bmatrix}, \tag{A.4}$$

where $\boldsymbol{I}$ is a 4×4 identity matrix.

Appendix B

Modelled multiphase equations

In this appendix, the modelled multiphase equation are summarized.

B.1 Simplifications

For the simulations performed in Chapter 6, the following assumptions and simplifications, discussed in Chapter 2, were made:

- Two dimensions and two phases.
- Equal pressure in the phases, Equation (2.42) on page 28.
- Equation of state, Equation (2.47) on page 29.
- No mass transfer.
- Turbulence was modelled with $\mu_{k,\text{eff}}$ = constant, Equation (2.36) on page 27.
- The fluctuating term from the averaging, $\Delta = 0$, Equation (2.32) on page 26.
- Interfacial pressure model, Equation (2.54) on page 31.
- Interfacial drag force, Equation (2.37) on page 27.
- The body force is gravity in the y-direction.

Continuity equation

The continuity equation comes from Equation (2.26),

$$\frac{\partial}{\partial t}\left(\alpha_k \rho_k\right) + \frac{\partial}{\partial x_i}\left(\alpha_k \rho_k u_{k,i}\right) = 0.$$

Momentum equation

The momentum equation comes from Equation (2.29),

$$\begin{aligned}\frac{\partial}{\partial t}\left(\alpha_k \rho_k u_{k,j}\right) + \frac{\partial}{\partial x_i}\left(\alpha_k \rho_k u_{k,j} u_{k,i}\right) + \frac{\partial}{\partial x_j}\left(\alpha_k p\right) \\ = B_k p \frac{\partial \alpha_k}{\partial x_j} + C \rho_{\mathrm{m}} \alpha_1 \alpha_2 \sqrt{(u_2 - u_1)^2 + (v_2 - v_1)^2}\left(u_{f,j} - u_{k,j}\right) \\ + \frac{\partial}{\partial x_i}\left(\alpha_k \tau_{k,ji}\right) + \alpha_k \rho_k g_j,\end{aligned}$$

where f is the other phase.

Stress tensor

The stress tensor comes from Equation (2.34),

$$\tau_{k,ji} = \mu_{k,\mathrm{eff}}\left(\frac{\partial u_{k,j}}{\partial x_i} + \frac{\partial u_{k,i}}{\partial x_j} - \frac{2}{3}\frac{\partial u_{k,l}}{\partial x_l}\delta_{ji}\right).$$

With this notation, the Navier-Stokes (or single-phase) equations arise by setting the number of phases to one.

B.2 The multiphase equations for two phases and two dimensions

Continuity phase 1

$$\frac{\partial}{\partial t}\left(\alpha_1 \rho_1\right) + \frac{\partial}{\partial x}\left(\alpha_1 \rho_1 u_1\right) + \frac{\partial}{\partial y}\left(\alpha_1 \rho_1 v_1\right) = 0,$$

Continuity phase 2

$$\frac{\partial}{\partial t}(\alpha_2\rho_2) + \frac{\partial}{\partial x}(\alpha_2\rho_2 u_2) + \frac{\partial}{\partial y}(\alpha_2\rho_2 v_2) = 0.$$

Momentum phase 1, x-direction

$$\begin{aligned}\frac{\partial}{\partial t}(\alpha_1\rho_1 u_1) + \frac{\partial}{\partial x}(\alpha_1\rho_1 u_1 u_1) + \frac{\partial}{\partial y}(\alpha_1\rho_1 u_1 v_1) + \frac{\partial}{\partial x}(\alpha_1 p)\\ = B_x p\frac{\partial \alpha_1}{\partial x} + C\rho_{\mathrm{m}}\alpha_1\alpha_2\sqrt{(u_2-u_1)^2+(v_2-v_1)^2}\,(u_2-u_1)\\ + \frac{\partial}{\partial x}(\alpha_1\tau_{1,11}) + \frac{\partial}{\partial y}(\alpha_1\tau_{1,12}).\end{aligned}$$

Momentum phase 1, y-direction

$$\begin{aligned}\frac{\partial}{\partial t}(\alpha_1\rho_1 v_1) + \frac{\partial}{\partial x}(\alpha_1\rho_1 v_1 u_1) + \frac{\partial}{\partial y}(\alpha_1\rho_1 v_1 v_1) + \frac{\partial}{\partial y}(\alpha_1 p)\\ = B_y p\frac{\partial \alpha_1}{\partial y} + C\rho_{\mathrm{m}}\alpha_1\alpha_2\sqrt{(u_2-u_1)^2+(v_2-v_1)^2}\,(v_2-v_1)\\ + \frac{\partial}{\partial x}(\alpha_1\tau_{1,21}) + \frac{\partial}{\partial y}(\alpha_1\tau_{1,22}) + \alpha_1\rho_1 g.\end{aligned}$$

Momentum phase 2, x-direction

$$\begin{aligned}\frac{\partial}{\partial t}(\alpha_2\rho_2 u_2) + \frac{\partial}{\partial x}(\alpha_2\rho_2 u_2 u_2) + \frac{\partial}{\partial y}(\alpha_2\rho_2 u_2 v_2) + \frac{\partial}{\partial x}(\alpha_2 p)\\ = B_x p\frac{\partial \alpha_2}{\partial x} + C\rho_{\mathrm{m}}\alpha_1\alpha_2\sqrt{(u_2-u_1)^2+(v_2-v_1)^2}\,(u_1-u_2)\\ + \frac{\partial}{\partial x}(\alpha_2\tau_{2,11}) + \frac{\partial}{\partial y}(\alpha_2\tau_{2,12}).\end{aligned}$$

Momentum phase 2, y-direction

$$\begin{aligned}\frac{\partial}{\partial t}\left(\alpha_2\rho_2 v_2\right) + \frac{\partial}{\partial x}\left(\alpha_2\rho_2 v_2 u_2\right) + \frac{\partial}{\partial y}\left(\alpha_2\rho_2 v_2 v_2\right) + \frac{\partial}{\partial y}\left(\alpha_2 p\right) \\ = B_y p\frac{\partial \alpha_2}{\partial y} + C\rho_{\mathrm{m}}\alpha_1\alpha_2\sqrt{(u_2-u_1)^2+(v_2-v_1)^2}\,(v_1-v_2) \\ + \frac{\partial}{\partial x}\left(\alpha_2\tau_{2,21}\right) + \frac{\partial}{\partial y}\left(\alpha_2\tau_{2,22}\right) + \alpha_2\rho_2 g.\end{aligned}$$

Stress tensor for phase 1

$$\tau_{1,11} = \mu_{1,\mathrm{eff}}\left(\frac{4}{3}\frac{\partial u_1}{\partial x} - \frac{2}{3}\frac{\partial v_1}{\partial y}\right),$$

$$\tau_{1,22} = \mu_{1,\mathrm{eff}}\left(\frac{4}{3}\frac{\partial v_1}{\partial y} - \frac{2}{3}\frac{\partial u_1}{\partial x}\right),$$

$$\tau_{1,12} = \tau_{1,21} = \mu_{1,\mathrm{eff}}\left(\frac{\partial u_1}{\partial y} + \frac{\partial v_1}{\partial x}\right).$$

Stress tensor for phase 2

$$\tau_{2,11} = \mu_{2,\mathrm{eff}}\left(\frac{4}{3}\frac{\partial u_2}{\partial x} - \frac{2}{3}\frac{\partial v_2}{\partial y}\right),$$

$$\tau_{2,22} = \mu_{2,\mathrm{eff}}\left(\frac{4}{3}\frac{\partial v_2}{\partial y} - \frac{2}{3}\frac{\partial u_2}{\partial x}\right),$$

$$\tau_{2,12} = \tau_{2,21} = \mu_{2,\mathrm{eff}}\left(\frac{\partial u_2}{\partial y} + \frac{\partial v_2}{\partial x}\right).$$